# Finite Cloud Effects in Longwave Radiative Transfer

by

Andrew K. Heidinger and Stephen K. Cox

Department of Atmospheric Science
Colorado State University
Fort Collins, Colorado

Colorado
State
University

Department of
Atmospheric Science

Paper No. 563

# FINITE CLOUD EFFECTS IN
# LONGWAVE RADIATIVE TRANSFER

by: Andrew K. Heidinger and Stephen K. Cox

Department of Atmospheric Science
Colorado State University
Fort Collins, CO 80523

November 1994

Atmospheric Science Paper No. 563

# ABSTRACT

## FINITE CLOUD EFFECTS IN LONGWAVE RADIATIVE TRANSFER

As numerical weather and climate prediction models demand more accurate treatment of clouds, finite cloud effects in longwave radiative transfer warrant further study. In this research, finite cloud effects are defined as the influence of cloud shape, size and spatial arrangement on longwave radiative transfer. To show the magnitude of these effects, radiometer data during ASTEX were analyzed. The ASTEX data showed that radiative transfer calculations which ignored the vertical dimensions of the clouds underestimated the longwave cloud radiative surface forcing by 30% on average. To study further these finite cloud effects, a three dimensional 11 $\mu$m radiative transfer model was developed. The results from this model, which neglected scattering, where shown to agree with the measurements taken during ASTEX on June 14, 1992. This model was also used to show that cloud macrophysical properties can be more important than cloud microphysical properties in the transfer of longwave radiation in optically thick clouds. In addition, results from simulated isolated and non-isolated clouds were presented. Due to the presence of neighboring clouds, the 11 $\mu$m heating rates in non-isolated clouds were shown to be significantly different from those in isolated clouds. Lastly, techniques for the inclusion of these finite cloud effects were discussed. Accurate heating profiles were achieved with a method which assumed a linear variation of the cloud fraction through the cloud layer. Parameterizations of the finite cloud effects for the marine stratocumulus observed during ASTEX are presented.

# ACKNOWLEDGEMENTS

# TABLE OF CONTENTS

# Chapter 1

## INTRODUCTION

Clouds have long been known to be the most variable component of the earth's atmospheric system. With the advent of satellite meteorology, scientists could for the first time study clouds and their effect on atmospheric radiative transfer on a global scale. These studies coupled with the recent progress in radiative transfer theory have clearly demonstrated that the commonly used plane-parallel approximation for radiative transfer in the presence in clouds is not valid over significant regions of the globe.

The research presented in this thesis will focus on finite cloud effects in longwave radiative transfer. Finite cloud effects are defined as the effects of the cloud's finite horizontal and vertical dimensions on radiative transfer. Much current research is committed to understanding the role of cloud microphysical properties in radiative transfer. This research will show that uncertainties in cloud macrophysical properties, such as cloud geometry, have the potential to be the dominant sources of error in longwave radiative transfer computations in partial cloudiness conditions. Plane-parallel theory, which assumes the cloud layer to be horizontally infinite and homogenous, will serve as a reference to measure the relative magnitude of these finite cloud effects.

## 1.1 The Global Occurrence of Finite Cloudiness

As any global satellite image will show, significant regions of the globe are covered by partial cloudiness at any one time. For example, Fig 1.1 shows the zonally averaged amount of cumulus when present over land for the Northern Hemisphere summer (Warren, 1986). As the figure shows, cumulus clouds usually appear in amounts less than 50%. As will be shown in this research, for cloud amounts typical of cumulus, the use of plane-parallel theory in longwave radiative transfer can cause significant errors. Looking at a photograph, Fig 1.2, of a typical fair weather cumulus cloud field off the coast of Florida, USA (Planck, 1969), one can easily visualize the

inadequacy of plane parallel radiative transfer theory in describing the radiative characteristics of such a cloud field. In fact, any region where convection is occurring likely to produce clouds with geometries that are not suitable for plane-parallel theory.
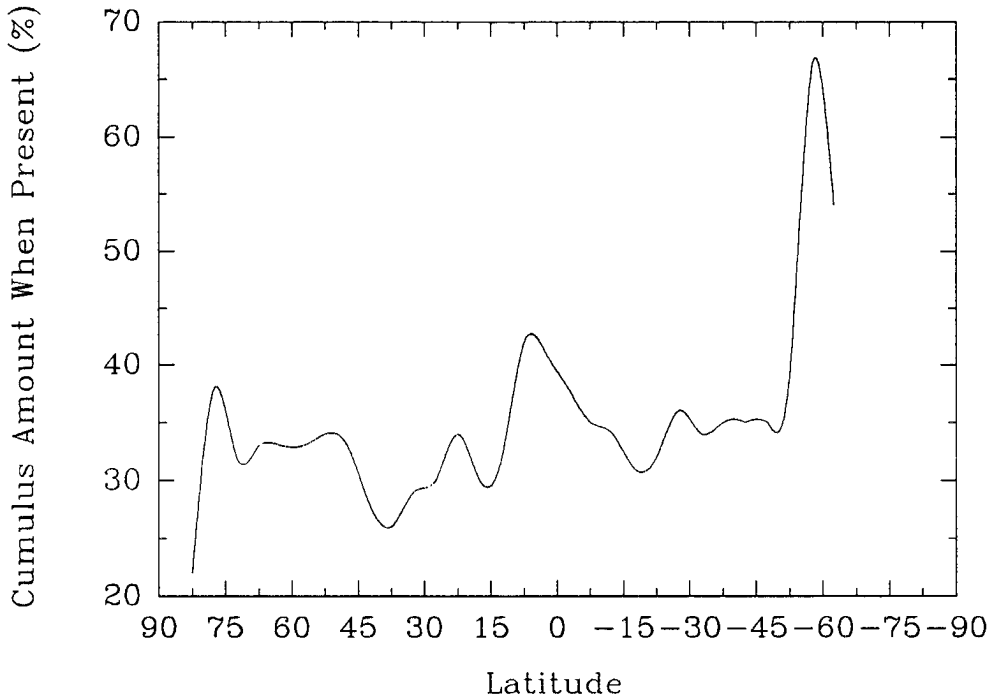


Fig. 1.1 Zonally averaged cumulus amount present. Data period is June, July and August from 1971 to 1981. Northern hemisphere is represented by positive latitudes. (NCAR/TN-273)

## 1.2 The Role of Clouds on the Earth's Radiation Budget

Clouds play a fundamental role in the modulation of earth's radiation budget (ERB). In the longwave spectral region, clouds act to warm the underlying surface by absorbing radiation emitted below the cloud and then re-emitting it back towards the surface, thus decreasing the net radiational loss of the surface. Outside of the polar regions, clouds also tend to be significantly cooler than the underlying surface. This temperature difference causes the outgoing longwave flux at the top of the atmosphere to be reduced dramatically in the presence of cloudiness. Fig 1.3 shows the magnitude of this latitudinally averaged reduction in the outgoing longwave flux due to the presence of various cloud types (Stowe *et al.* 1989). Clearly clouds can have a dramatic effect on longwave radiative transfer throughout the atmosphere, and it is the understanding of the variation of this effect with changes in cloud cover and geometry that is the aim of this research.

2

Fig. 1.2 A photograph of a fair weather cumulus cloud field of the coast of Florida, USA. (taken from Planck, 1969)
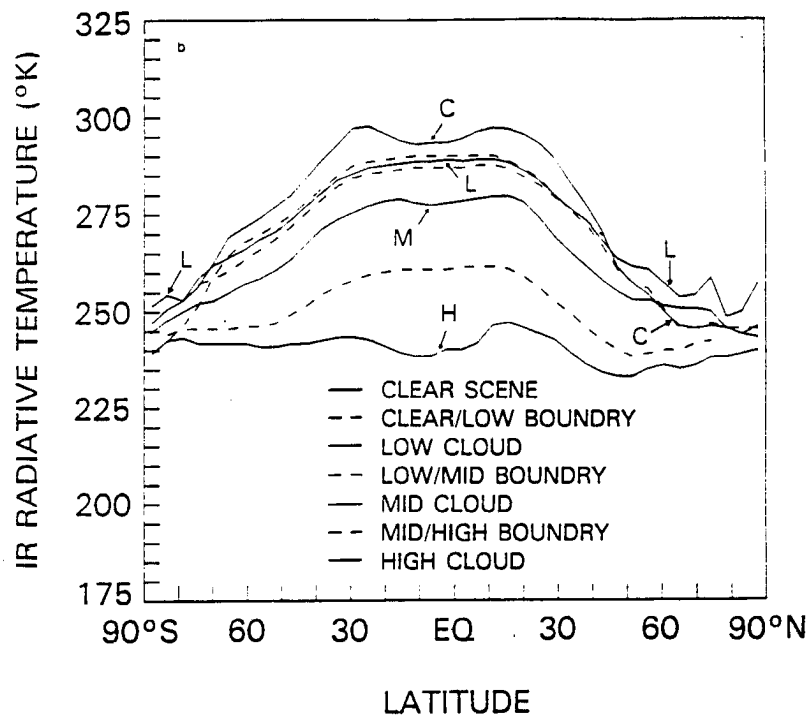


Fig. 1.3 The zonally averaged effect of differing cloud types on the amount of longwave radiation escaping from earth to space. (taken from Stowe *et al.*, 1989)

3

## 1.3    The Objectives of this Research

Due to the potentially large effect of clouds on the earth radiation budget, an investigation into the role of finite cloudiness on longwave radiative transfer is certainly warranted. Keeping in mind the accomplishments of previous studies, five main research objectives were identified and are listed below.

1.    Determine and quantify finite cloud effects in the downwelling longwave surface flux data taken during the Atlantic Stratocumulus Experiment (ASTEX). Unlike previous studies, which used cloudiness data to estimate finite cloud effects, this study will attempt to measure these effects directly.

2.    Develop a flexible, efficient three dimensional longwave radiative transfer model. In contrast to previous studies which attempted to include finite cloud effects into one dimensional radiative transfer models, this model will allow fully three dimensional clouds of arbitrary shape and size.

3.    Compare longwave radiative transfer through isolated and non-isolated clouds. As will be discussed in the next chapter, several longwave radiative transfer modeling studies of isolated clouds have been performed. In this paper, the three dimensional model will be used to study how neighboring clouds affect longwave radiative transfer in non-isolated clouds.

4.    Examine methods for the inclusion of finite cloud effects into one dimensional longwave radiative transfer schemes. Model results will be used to show that the common practice of using the cloud fraction to weight the clear and overcast sky radiative transfer solutions to approximate the partial cloudy solution introduces significant errors.

5.    Develop parameterizations of these finite cloud effects in terms of quantities readily available to

existing numerical weather and climate prediction models

## 1.4 Organization

The following thesis will be organized into ten chapters.  Chapter 2 will briefly discuss results of previous

research which has dealt with finite cloud effects in longwave radiative transfer.  The development of the three

dimensional longwave radiative transfer model will be outlined in Chapter 3.  Results from this model will be used

to show how an important meteorological quantity, the cloud fraction, varies for differing simulated cloudiness

conditions in Chapter 4.  Measurements showing the magnitude of the finite cloud effects during ASTEX will be

presented in Chapter 5.  Chapter 6 will present a detailed case study of one ASTEX day.  A comparison of longwave

radiative transfer in isolated and non-isolated clouds is shown in Chapter 7.  An investigation of the inclusion of

finite cloud effects in one dimensional radiative schemes is performed in Chapter 8.  The parameterization of finite

cloud effects is discussed in Chapter 9. Lastly, Chapter 10 presents a summary of the conclusions from this study.

# Chapter 2

## PREVIOUS RESEARCH ON FINITE CLOUD EFFECTS
## IN LONGWAVE RADIATIVE TRANSFER

This chapter will briefly highlight some of the major accomplishments of previous studies that have dealt

with finite cloud effects in radiative transfer. As shown below, research on this subject has been ongoing for over

twenty years. By recognizing the strengths and weaknesses of past research, this study will attempt not to duplicate

the previous research, but to further the understanding of radiative transfer in finite clouds.


## 2.1    Niylisk 1968,1972

Estimates in the errors in the downwelling longwave surface flux calculations due to neglecting the cloud's

vertical dimensions were first made by Niylisk in papers published in 1968 and 1972. In the earlier paper, he

assumed cloud fields with simple azimuthal symmetric geometries and that the clouds behaved as isothermal

blackbodies. In the 1972 paper, he continued to treat the clouds as black bodies, but he also used cloud field data

recorded by Plank in 1969. Plank's observations were of small fair weather cumuli cloud fields off the coast of

Florida. Niylisk's findings were that for small cumulus clouds, maximum errors of 3% would be expected in the

calculation of downwelling flux if the vertical dimensions of the clouds were ignored. Though a small percentage,

a 3% error in the downwelling flux could easily represent an absolute error of 10 $W/m^2$. As will be shown, an

error of 10 $W/m^2$ in the longwave flux, could represent a 25% error in the longwave cloud surface forcing

calculations.


## 2.2 Liou and Ou, 1979

The study published by Liou and Ou in 1979 was concerned primarily with longwave radiative transfer

through an isolated finite cloud. They utilized a four term truncated spherical harmonics expansion for the scattering

phase function and intensity to derive analytic solutions to the three dimensional radiative transfer equation. The

6

clouds were assumed to be isothermal and the effects of water vapor were ignored. Their findings showed that unlike plane parallel clouds, finite cloud emissivities do not approach unity and may be as much as 30% lower than the plane parallel value. Also, due to the emission from lateral cloud boundaries, horizontally averaged cooling rates inside finite clouds are larger than those in plane parallel clouds.

## 2.3 Harshvardhan, Weinman and Davies 1981

As done in Liou and Ou (1979), Harshvardhan, Weinman, and Davies (1981) were primarily concerned with longwave radiative transfer in isolated cuboidal clouds. A variable azimuth two-stream (VATS) approximation was used to analytically solve the radiative transfer equation. Their results also showed that isolated finite clouds cool significantly more than plane parallel clouds. For example, Fig 2.1 shows the horizontally averaged heating rate profile for an isolated cubic cloud with dimensions of 1 km on each side. In this example, the cloud temperature was -10°C and the underlying surface was 15°C. In addition, this study also showed that brightness temperature measurements from finite clouds can be significantly higher than the cloud-top temperature.

## 2.4 Harshvardhan and Weinman, 1982

The previous theoretical studies mentioned above all dealt with longwave radiative transfer in isolated cuboidal clouds. The transfer of longwave radiation through a layer of interacting clouds was addressed by Harshvardhan and Weinman (1982). The simulated cloud layer consisted of a regular array of cuboidal cloud elements. An experimental method was used to determine the variation of the effective cloud fraction with the absolute cloud fraction for different cloud aspect ratios. As will be discussed in Chapter 4, the effective cloud fraction accounts for the vertical dimensions of the clouds while the absolute cloud fraction accounts for only the horizontal coverage of the clouds. The theory was developed for blackbody clouds and was extended to scattering non-black clouds through the use of the VATS approximation. For a layer of black clouds, they showed the ratio of the mean cooling in the finite cloud layer to that of a planiform cloud is simply the ratio of the effective to the absolute cloud fraction. As Fig 2.2 shows, the commonly used planiform estimate for the mean cooling of the cloud layer significantly underestimates the true value for small cloud fractions and large cloud aspect ratios.
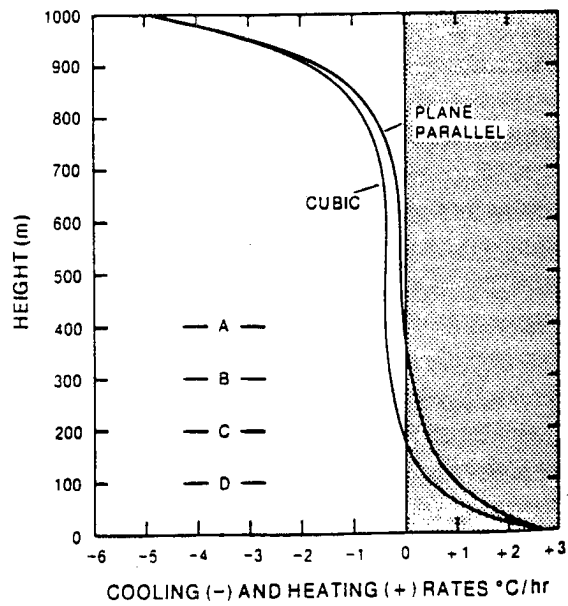
Fig. 2.1 A comparison of the simulated cooling profiles in isolated cubic and plane-parallel clouds. (taken from Harshvardhan et. al., 1981)
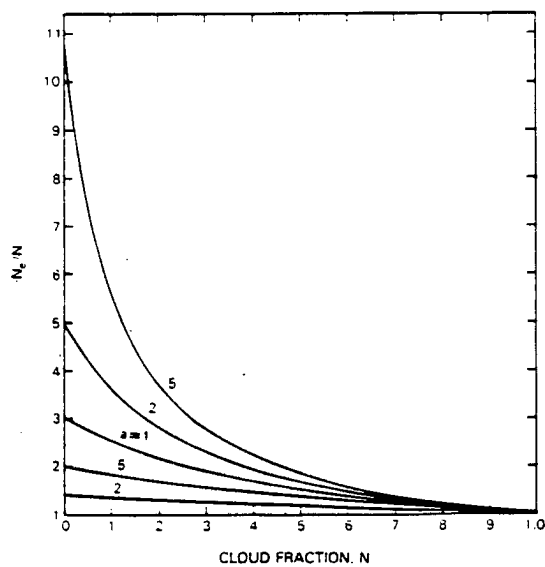


Fig. 2.2 Ratio of the total cooling rates in cuboidal and planiform cloud layers as a function of cloud fraction, N, for differing cloud aspect ratios,a. (taken from Harshvardhan and Weinman, 1982)

8

## 2.5 Ellingson, 1982

The three previous studies have used analytical solutions of the three dimensional longwave radiative transfer equation to simulate radiative transfer through cuboidal clouds. Another method would be to incorporate three dimensional finite cloudiness directly into the formulation of a two dimensional model statistically. This is the method used by Ellingson (1982) where the cloud layer was assumed to be composed of blackbody right circular cylinders that could be described by a probability of a clear line of sight function. A comparison of this function with one produced by the model described in Chapter 3 is shown in Chapter 4. Using this formulation, Ellingson was able to show underestimations in the planiform estimates of downwelling longwave fluxes of 1-4%, which are roughly equivalent to the estimates of Niylisk (1972). Results from this study included showing that the tropospheric column consisting of cylindrical clouds may cool up to 10% more than a column consisting of planiform clouds.

## 2.6 Stephens and Preisendorfer, 1984

The radiative behavior of isolated finite cuboidal clouds was studied by in a series of two papers by Stephens and Preisendorfer. In Part 1, Preisendorfer and Stephens (1984), the radiative transfer equation was solved using two dimensional Fourier series for a laterally finite scattering medium. In Part 2, Stephens and Preisendorfer (1984), thermal emission was included and results showing the transfer of 10 $\mu$m radiation in isolated cuboidal clouds were presented. As shown by Liou and Ou (1979) and Harshvardhan et al. (1981), this study showed that isolated cuboidal clouds could cool significantly more than plane parallel clouds. This enhanced cooling, however, was shown to be dependent on the temperature difference between the cloud and the ground. If the clouds were sufficiently high in the atmosphere, this study showed that isolated clouds could warm significantly more than plane parallel clouds.

## 2.7 Evans, 1993

Unlike this thesis and the studies described above which explored radiative transfer through media composed of simplistic geometries, Evans (1993) modelled cloud heterogeneity stochastically. This stochastic

modelling approach was accomplished using a backward Monte Carlo technique with the radiative effects of differing cloud structures being described by probability density functions. Though this method is limited to producing only mean radiative fluxes, it is these mean quantities that are of most interest to climate models.

## 2.8 Killen and Ellingson, 1994

Using an approach similar to Ellingson (1982), Killen and Ellingson (1994) explored the effect of cloud shape and spatial resolution on longwave fluxes in the presence of broken cloud fields. Clouds were modelled as right cylinders with vertically sloping sides. Their results showed that longwave fluxes are sensitive to both the assumed distribution of the cloudiness and on the assumed cloud shapes.

## 2.9 Summary

As discussed above, significant progress has been made in the study of longwave radiation transfer in finite clouds during the last two decades. Several key issues still need to be resolved. For example, no study has shown actual measurements of the radiative effect of finite cloudiness nor has any study tried to compare measured and modelled longwave calculations under finite cloudiness. In addition, the inclusion of finite cloudiness in numerical weather prediction has not been fully addressed. These are a few of the issues that this study will address.

# Chapter 3

## A MODEL FOR LONGWAVE RADIATIVE TRANSFER IN THE PRESENCE OF THREE DIMENSIONAL FINITE CLOUDS

The purpose of this research is to explore the effect of finite cloudiness on infrared radiative transfer. To aid in the understanding of this problem, a model was developed. In order to be useful, this model needed to be able to simulate the fully anisotropic radiance field in the presence of three dimensional broken cloud fields. Several different methods could have been used to model infrared radiative transfer in three dimensions such as the Fourier Transform method of Stephens (1988), the SHSG method of Evans (1993), the VATS technique of Harshvardhan (1981) and the Monte Carlo method. However, each of these methods has limitations and all are computationally intensive. In addition, the three dimensional variation of the cloudiness could have been incorporated into a one dimensional model stochastically through the use of a probability of a clear-line-of-sight function (Niylisk, 1972) (Ellingson, 1980). Though computationally efficient, this method did not allow for non-black clouds and the validity of these clear line-of sight functions has never been determined. The model developed in this chapter was a compromise among versatility, speed and accuracy.

## 3.1 Model Spectral Region

In the interest of computational efficiency, radiative transfer through finite clouds was simulated only at 11 $\mu$m, though an extension to broad-band radiative transfer is made in Section 3.6. The modelled spectral region was chosen since most of the cloud's influence in the infrared is felt in the 8-14 $\mu$m window region. This limited spectral range of the longwave cloud radiative surface forcing (LW CRSF) is shown in Fig 3.1, taken during ASTEX on the Island of Porto Santo. This figure shows spectra taken under clear and stratus conditions. Comparison of the two spectra shows them to be nearly identical except in the 8-14 $\mu$m region (800-1200 cm$^{-1}$). Therefore, the spectral range of the model was chosen to be 11 $\mu$m (910 cm$^{-1}$) to study the effect of finite cloudiness on infrared radiative transfer. Developing a monochromatic model rather than a broad-band one drastically reduces

11

the computational burden while still retaining the sensitivity of the LW CRSF to differing cloudiness conditions.
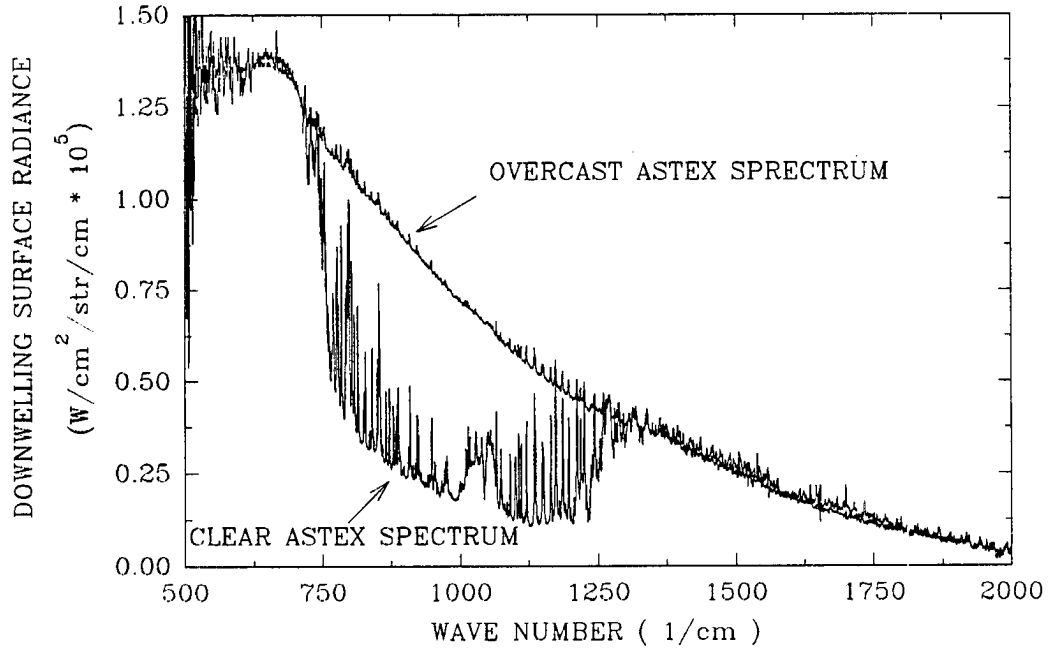


**Fig. 3.1 Clear and cloudy (stratus) spectra during ASTEX**

## 3.2 Model Formulation

The model developed simulates a cloud layer imbedded in an emitting and absorbing atmosphere. The processes of scattering and reflection by the cloud elements and the underlying surface are neglected. A discussion of the effects of scattering is given Section 3.7. Only the effects of atmospheric water vapor and cloud liquid water are included in the model. Horizontal homogeneity is assumed in the atmospheric temperature and moisture fields. The underlying surface is assumed to be Lambertian and to emit with a specified temperature and emissivity. The downward flux at the top model layer is assumed to be negligible. Fluxes are determined by a finite difference integration over both the zenith angle and the azimuth angles.

### 3.2.1 Model Geometry

The geometry of the model environment is shown in Fig. 3.2. A right handed cartesian coordinate system is used with the azimuth and zenith angles defined as shown. The model has the ability to calculate fluxes at any

12

point in the model domain, including inside of individual cloud elements.
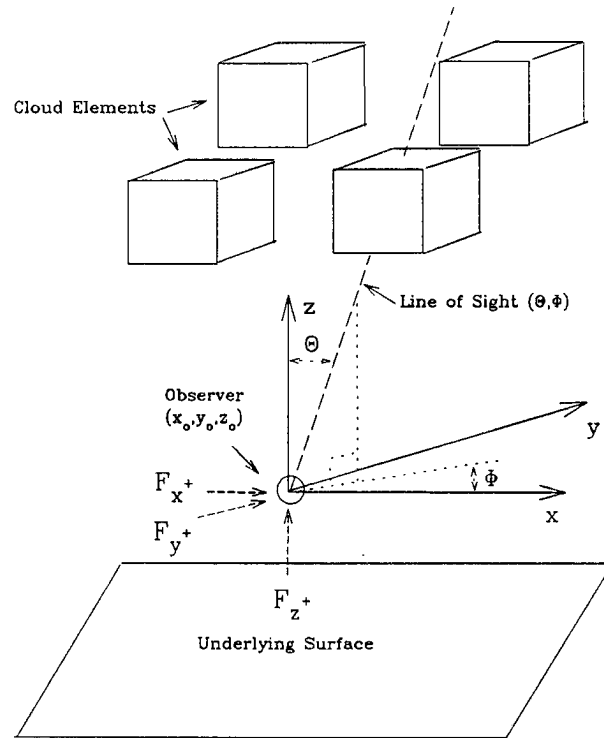


**Fig 3.2 Schematic illustration of model domain showing coordinates and flux conventions.**

The cloud layer consists of an infinite number of finite cloud elements. Each element can be of arbitrary shape, but for most of this research identical rectangular shapes were assumed. Also, the spacing between cloud elements can be any value, but for most of this research the clouds elements were spaced uniformly. The depth of the cloud layer is assumed to be constant and only one cloud layer is assumed present.

Each cloud element can assumed to be a blackbody or the liquid water content in the cloud elements can be set. This liquid water content can be a constant value or it can be function of the vertical position in the cloud. The temperature of the cloud elements can either vary with the temperature of the environment or it can specified separately.

## 3.3 Calculation of Cloud Forcing Radiance

The radiances calculated in the model at a specified observer location are formulated in terms of a cloud forcing radiance. As with other cloud forcing quantities, the cloud forcing radiance is the difference between the

13

radiance with and without cloud present. Only when the line-of-sight intercepts a cloud, does the cloud forcing radiance, $I_{cf}$, take on a non-zero value.

The longwave radiative transfer equation in the absence of scattering can be expressed for the downwelling radiance at some optical depth, $\tau$, as:

$$I^-(\tau,-\mu) = I(0,-\mu)\, e^{-\frac{\tau}{|\mu|}} + \int_0^\tau B(\tau')\, e^{-(\tau-\tau')/|\mu|}\, \frac{d\tau'}{|\mu|} \quad (3.1)$$

where $\mu$ is the cosine of the zenith angle. The radiance at the top of the atmosphere, $\tau=0$, is specified by $I(0,-\mu)$. Imagine a line of sight emanating upwards from an observer placed below the cloud layer, as shown in Fig 3.3. Eq. (3.1) can be rewritten to express the radiance, I, along the $\Theta$, $\Phi$ direction as contributions from the sub-cloud layer (A), cloud, layer (B), and the above cloud layer (C) as:

$$I^-(x_o, y_o, z_o, \theta, \phi) = \underset{A}{I^-_{sc}} + \underset{B}{T_{sc} I^-_{cld}} + \underset{C}{T_{sc} T_{cld} I^-_{ac}} \quad (3.2)$$

where $T_{sc}$ and $T_{cld}$ are the 11 $\mu$m transmissions through the sub-cloud and cloud layer respectively. Due to the three dimensional variation of the cloud field, I is now a function of x,y and z as well as $\Theta$ and $\Phi$. The downwelling emissions from the sub-cloud and clouds layers are represented by $I_{sc}$ and $I_{cld}$. The radiance observed for a clear sky can also be expressed as:

$$I^-_{clr}(z_o, \theta, \phi) = I^-_{sc} + T_{sc} I^-_{cldgas} + T_{sc} T_{cldgas} I^-_{ac} \quad (3.3)$$

where $T_{cldgas}$ and $I_{cldgas}$ are the transmission and emission along a path from the cloud layer due only to the ambient water vapor. These two quantities can be subtracted to produce a cloud forcing radiance, $I_{cf}$, given by:

$$I^-_{cf}(x_o, y_o, z_o, \theta, \phi) = T_{sc}[\,(T_{cld}-T_{cldgas})\, I^-_{ac} + (I^-_{cld}-I^-_{cldgas})\,] \quad (3.4)$$

A similar procedure for the upwelling radiances yields:

$$I^+_{cf}(x_o, y_o, z_o, \theta, \phi) = T_{ac}[\,(T_{cld}-T_{cldgas})\, I^+_{sc} + (I^+_{cld}-I^+_{cldgas})\,] + $$
$$T_{ac} T_{sc} (T_{cld}-T_{cldgas})\, I_{sfc} \quad (3.5)$$

where $T_{ac}$ and $I_{ac}$ are the 11 $\mu$m transmission and emission from the cloud top to the observer and $I_{sfc}$ is the emission

14

from the underlying surface.

Line of Sight

Above Cloud Emission
(Water Vapor)

Cloud

/C

Cloud Layer Emission
(Liquid Water and Water Vapor)

B

Subcloud Layer Emission
(Water Vapor)

A

Observer

Underlying Surface, $T_{sfc}$ & $\epsilon_{sfc}$
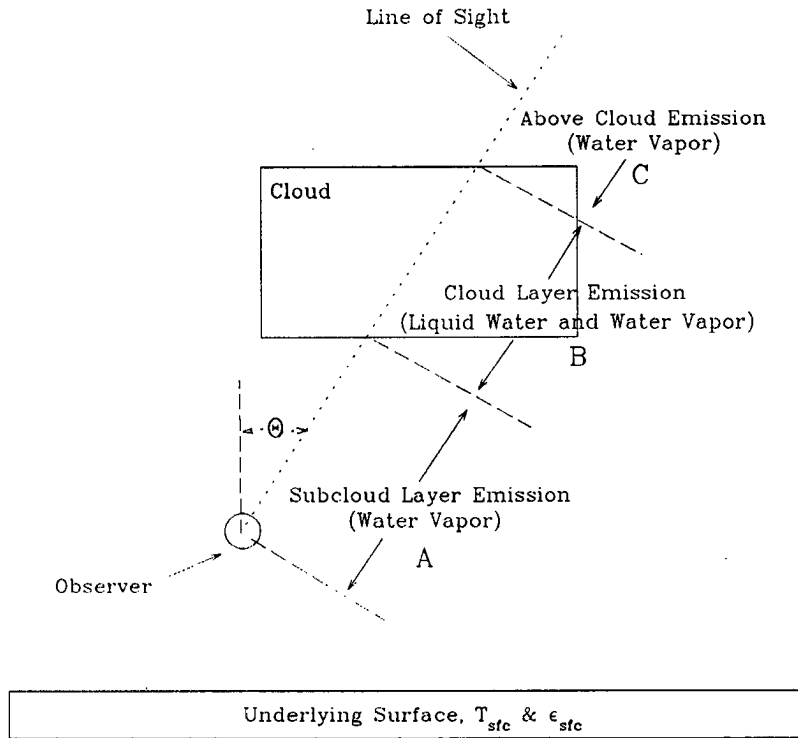
**Fig 3.3 Schematic illustration of sources of radiance along an arbitrary line of sight.**

### 3.3.1 Calculation of Cloud Layer Emissions

Using the absorption approximation for clouds, which assumes that cloud droplet absorption is dominant compared to cloud droplet scattering (Stephens, 1984), allows the transmission through the cloud layer to be expressed as:

$$T_{cld}(x_o, y_o, z_o, \theta, \phi) = \exp(-k_{abs}W) \, T_{cldgas} \qquad (3.6)$$

where $k_{abs}$ is the appropriate mass absorption coefficient and W is the total amount of liquid water encountered along the line-of-sight through the cloud layer. The value of $k_{abs}$, 0.13 m$^2$/g, was taken from Schmetz (1981) and is appropriate for boundary layer clouds at 11 $\mu$m. The determination of the transmission through the cloud layer due to the ambient water vapor, $T_{cldgas}$, is described in Section 3.5.2. Once the transmission through the cloud layer is known, the emission along the line through the cloud layer is assumed to be linear in optical depth (Ackerman 1990)

15

and is given by:

$$I_{cld}^- = B_o - B_n T_{cld} + \frac{(B_n - B_o)}{\ln(T_{cld})}(T_{cld} - 1)$$

$$I_{cld}^+ = B_n - B_o T_{cld} + \frac{(B_o - B_n)}{\ln(T_{cld})}(T_{cld} - 1)$$

$$(3.7)$$

where $B_o$ and $B_n$ are the 11 $\mu$m Planckian emissions at the temperatures of the lower and upper intersection points of the line-of-sight with the cloud layer respectively.

### 3.3.2 The Model Treatment of Cloud to Cloud Interactions

One necessary capability of any three dimensional radiative transfer model which simulates finite cloudiness is the ability to simulate cloud to cloud radiative interactions. When calculating the radiance emitted along a line-of-sight that passes through multiple clouds, two simplifying assumptions are made. First, any emission and absorption in the clear regions between the clouds is ignored. Second, the Planckian emission is assumed to vary linearly with the cloud optical depth between the intersection points of the line-of-sight with the cloud layer. With these two assumptions, the emission along a line-of-sight passing through multiple clouds is given by Eq. (3.7) with $T_{cld}$ being composed of components from each intersected cloud.

### 3.4 Calculation of Model Fluxes

Knowing the cloud forcing radiance field, the cloud forcing fluxes can be determined. To obtain the actual fluxes at the observer position, the appropriate clear sky fluxes are simply added to the cloud forcing fluxes. The calculation of the clear sky fluxes is discussed in the next section. Six fluxes are calculated at the observer location, each being associated with either the positive or negative direction along the x, y and z axes. The six fluxes are determined through a finite integration of the following expressions:

16

$$F_{cf,z^+} = \int_0^{2\pi} \int_0^1 I_{cf}\mu\, d\mu\, d\phi$$

$$(3.8)$$

$$F_{cf,z^-} = \int_0^{2\pi} \int_{-1}^0 I_{cf}\mu\, d\mu\, d\phi$$

$$F_{cf,x^+} = \int_{-\frac{\pi}{2}}^{\frac{\pi}{2}} \int_{-1}^1 I_{cf}\nu\cos\phi\, d\mu\, d\phi$$

$$(3.9)$$

$$F_{cf,x^-} = \int_{\frac{\pi}{2}}^{-\frac{\pi}{2}} \int_{-1}^1 I_{cf}\nu\cos\phi\, d\mu\, d\phi$$

$$F_{cf,y^+} = \int_0^{\pi} \int_{-1}^1 I_{cf}\nu\sin\phi\, d\mu\, d\phi$$

$$(3.10)$$

$$F_{cf,y^-} = \int_{\pi}^0 \int_{-1}^1 I_{cf}\nu\sin\phi\, d\mu\, d\phi$$

here $\mu$ and $\nu$ are the cosine and sine, respectively, of the zenith angle, $\Theta$.

### 3.4.1 Model Resolution

For most of the model results presented in this study, an angular resolution of 2.5° was used. For example, the sensitivity to the angular resolution in the downwelling flux is shown in Fig. 3.4. In this example, angular resolutions of less than 5.0° produced accurate flux measurements. Higher angular resolution would be necessary, however, if the distance between the observer and the cloud layer were increased.

When horizontally or vertically averaged quantities are calculated, the issue of spatial resolution must also be addressed. In Fig. 3.5, the effect of differing spatial resolutions on the gradient of $F_x^{net}$ near the left lateral side of cubic cloud is shown for two different cloud liquid water contents, LWC. As Fig. 3.5 shows, a spatial resolutions of less than 50 meters is needed to resolve the steep gradient of $F_x^{net}$ near the cloud boundary for the

LWC = 0.1 g/m$^3$ case. Due to the increase of the gradient of $F_x^{net}$ near the boundary for the LWC = 1.0 g/m$^3$ case, finer spatial resolutions are needed to accurately resolve the heating near the boundary. For the heating rate calculations presented in Chapters 7 and 8, spatial resolutions of 25 and 50 meters were used respectively.
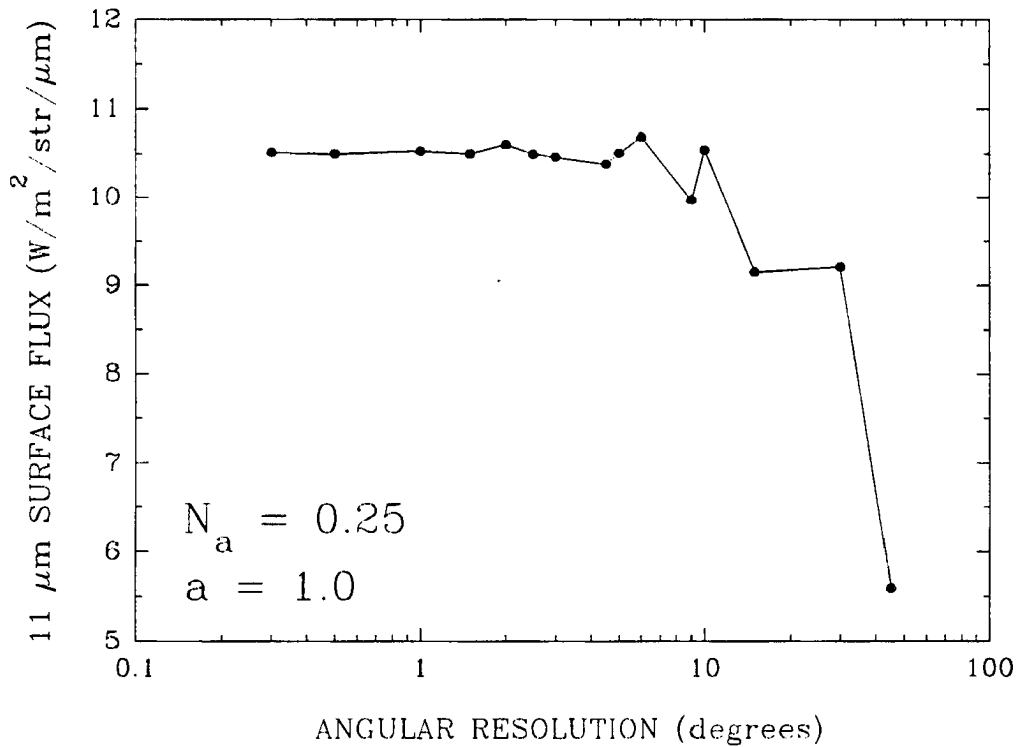


Fig. 3.4 The effect of angular resolution in the calculation of the downwelling flux.

## 3.5 Clear Sky Radiative Transfer at 11 $\mu$m

Before the effect of clouds on the infrared radiative transfer could be modelled, the clear sky fluxes needed to be determined. As stated previously, once the clear sky fluxes are known, the effect of the clouds can be superimposed upon these fluxes to determine the total fluxes in the presence of the finite clouds.

### 3.5.1 Gaseous Absorption

In the 8-14 $\mu$m window region, absorption of radiation by water vapor is governed by water vapor continuum absorption, also known as e-type absorption. The calculation of this absorption was done as outlined

18

LWC = 1.0 g/m$^3$
—— 10 m res.
---- 25 m res.
----- 50 m res.
—— 100 m res.

11 $\mu$m $F_x^{net}$ (W/m$^2$/$\mu$m)

0.00
-0.25
-0.50
-0.75
-1.00
-1.25
-1.50
-1.75
-2.00

-650 -600 -550 -500 -450 -400 -350

x(m)

LWC = 0.1 g/m$^3$
—— 10 m res.
--- 25 m res.
----- 50 m res.
—— 100 m res.

11 $\mu$m $F_x^{net}$ (W/m$^2$/$\mu$m)

0.00
-0.25
-0.50
-0.75
-1.00
-1.25
-1.50
-1.75
-2.00

-650 -600 -550 -500 -450 -400 -350

x(m)
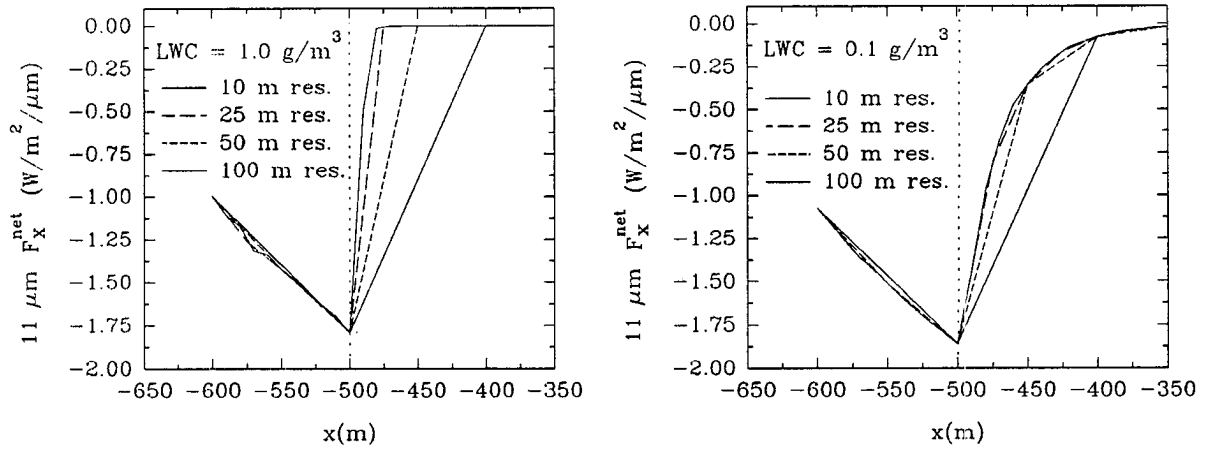
**Fig. 3.5 The effect of spatial resolution on resolving the gradient of $F_x^{net}$ near cloud lateral boundaries.**

in Stephens (1984). The expressions are empirical fits of data collected by Roberts et al. (1976). The mass absorption coefficient, $k_{abs}$, for e-type absorption is given as:

$$k_{abs} = \frac{\Phi(T)}{\Phi(T_0)} \Psi(v, T_0) e_c \quad (3.11)$$

where

$$\Phi(T) = \exp\frac{1800}{T} \quad (3.12)$$

$$\Psi(v, T_0) = c_1 + c_2 \exp(-c_3 v) \quad (3.13)$$

and $e_c$, the corrected water vapor pressure is given as:

$$e_c = e_{H_2O} + \gamma (P - e_{H_2O}) \quad (3.14)$$

where P and $e_{H2O}$ are the mean atmospheric pressure and water vapor partial pressure of the layer in atmospheres respectively. The variable $\gamma$ is a self broadening correction and the values for all of the constants used in the parameterization are shown in Table 1.

19

| CONSTANT | VALUE | SOURCE |
|---|---|---|
| $T_o$ | 296 K | Stephens, 1984 |
| $c_1$ | 4.2 cm$^2$/g/atm | Stephens, 1984 |
| $c_2$ | 5588 cm$^2$/g/atm | Stephens, 1984 |
| $c_3$ | 0.00787 cm | Stephens, 1984 |
| $\gamma$ | 0.002 | Kneizys et al., 1980 |
| $\nu$ | 910 1/cm | User Specified |

Table 1. The values of the parameters used in the Stephens (1984) continuum absorption parameterization

A comparison of the total zenith transmission from the top of the atmosphere to the surface between the Stephens (1984) parameterization and two commonly used radiative transfer codes, LOWTRAN and MODTRAN, is shown in Fig. 3.6. The LOWTRAN code has a spectral resolution of 20 cm$^{-1}$ while the MODTRAN code has a spectral resolution of 1cm$^{-1}$. The temperature and water vapor profiles used were taken from an ASTEX sounding. As Fig. 3.6 shows, the Stephens (1984) parameterization does accurately reproduce the broad scale spectral variation of the transmission as compared with the other models, especially in the most transparent regions of the atmospheric window where ozone and carbon dioxide contribute little to the absorption. Since this parameterization does not emulate the finer scales of the spectral variation of the transmission, the quoted 11 $\mu$m values are not truly the exact monochromatic values at 11 $\mu$m, but merely representative monochromatic values in the spectral region surrounding 11 $\mu$m.

### 3.5.2 Clear sky fluxes

Using the above technique to determine the mass absorption coefficient $k_{abs}$, for water vapor continuum absorption at 11 $\mu$m, the transmission of each layer can now determined simply as:
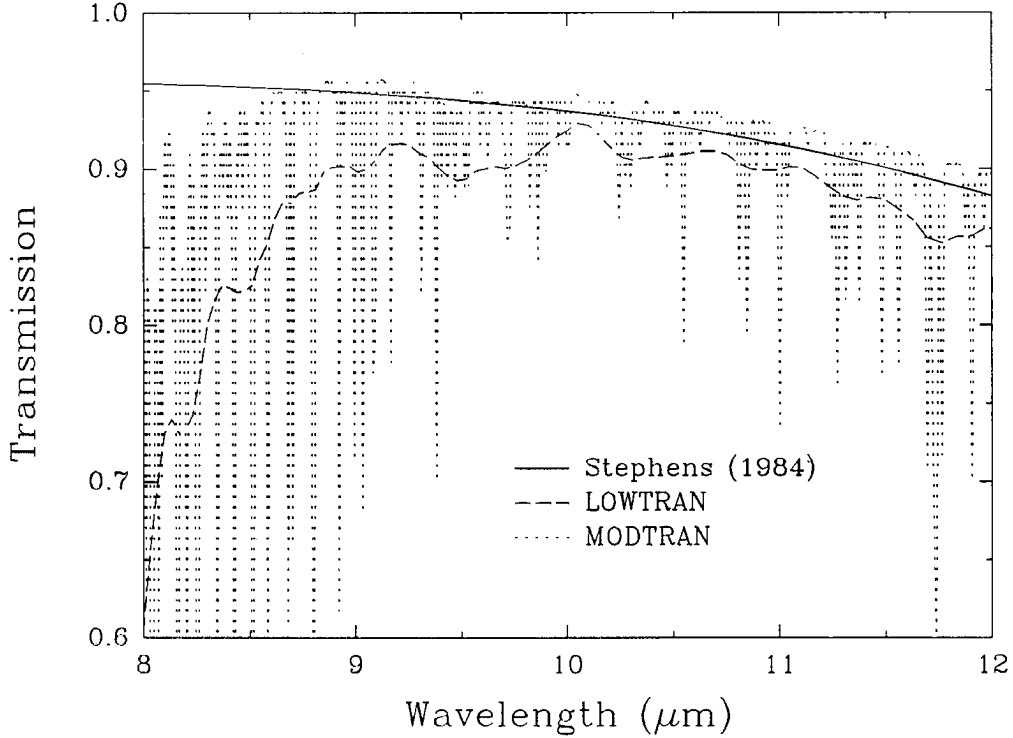
**Fig. 3.6** Comparison of total zenith transmission in the atmospheric window for ASTEX using the Stephens (1984) parameterization, LOWTRAN and MODTRAN

$$T(\mu) = (\exp(-k_{abs}u))^{1/\mu}$$ 

(3.15)

where u, the optical mass is defined as:

$$u = \frac{r\Delta p}{g}$$

(3.16)

where r is the mean water vapor mixing ratio across a layer with a pressure thickness of $\Delta p$ and $\mu$ is the cosine of the zenith angle and g is the gravitational constant. Note that calculating the transmission in this way avoids the use of any scaling factors since the variation of pressure and temperature are explicitly in the expression for the mass absorption coefficient (Stephens 1984). Also, due to the transmission expression being in an exponential form and monochromatic, the transmission through multiple layers is simply the product of the transmissions of the separate layers as shown below.

$$T(\mu)_{1...3} = T(\mu)_1 \times T(\mu)_2 \times T(\mu)_3$$

(3.17)

To calculate the radiance from each clear sky layer, the emission from the layer was assumed to be linear in optical depth (Ackerman 1989). With this assumption, the emission from a layer, 1, along direction $\mu$, $H(1,\mu)$, can be written as:

$$H(1,\mu) = B_o + \frac{(B_o - B_n)}{\ln(T(1,\mu))} \qquad (3.18)$$

where $B_o$ and $B_n$ are the Planckian emission for the temperature at the bottom and top of the layer respectively.

Knowing the transmission and emission from each layer, the radiance fields can be determined by simply summing through the layers to obtain the radiance field at a particular level, 1, along a particular direction, $\mu$, as shown by:

$$I_{clr}^-(1,\mu) = H(1,\mu) + T(1,\mu)F^-(1+1,\mu) \qquad (3.19)$$

$$I_{clr}^+(1,\mu) = H(1-1,\mu) + T(1-1,\mu)I^+(1-1,\mu) \qquad (3.20)$$

where layer "1+1" is the layer above layer "1" and the subscripts "+" and "-" refer to the upwelling and downwelling radiance fields respectively. The boundary conditions at the underlying surface, 1=1, and the top of the atmosphere, 1=n, are:

$$I^-(n,\mu) = 0 \qquad I^+(1,\mu) = \epsilon_{sfc} \times B_{sfc} \qquad (3.21)$$

where $\epsilon_{sfc}$ and $T_{sfc}$ are the emissivity and temperature of the underlying surface respectively.

Knowing the radiance field at each level, the fluxes at each level can be obtained by integrating over the azimuth and zenith angles as shown in Eqs. (3.8)-(3.10). In this case, azimuthal symmetry was assumed so that the integration over azimuth simply introduced a factor of $2\pi$.

## 3.6 Model Extension to Broad-band Radiative Transfer

As described in Section 3.1, the model developed in this chapter was limited to the spectral range of 11 $\mu$m. However, if one assumes that the clouds are grey bodies, the broad-band radiance can be found empirically from the 11 $\mu$m radiance. The empirical relation depends not only on the moisture and temperature profile of the atmosphere but also on the position of the observer. The empirical fit derived from the composite ASTEX sounding

for an observer looking up from the surface expressed in terms of equivalent brightness temperatures, EBT's, is

shown in Fig. 3.7. The 11 $\mu$m values were obtained using the continuum absorption parameterization discussed

in Section 3.5. The broadband values were calculated using LOWTRAN.
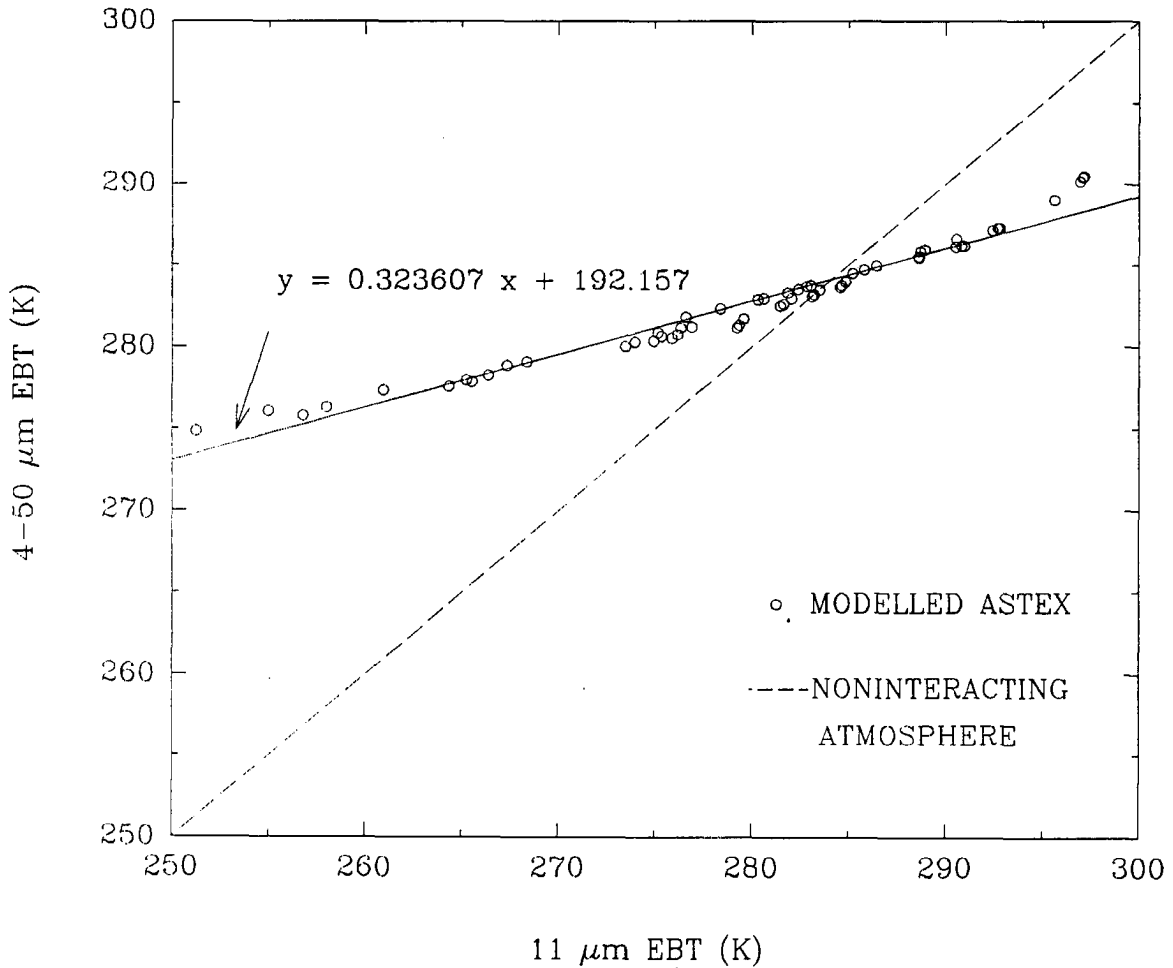


Fig. 3.7 Comparison of broadband and 11 micron EBT's for the composite ASTEX sounding.

Each point in Fig. 3.7, was calculated by placing a blackbody cloud at some level in the atmosphere. The

altitudes of the clouds ranged from 0.5 km to 7.5 km which spans the observed range of cloud altitudes. The cloud

temperature was varied from the ambient temperature at that level to 10°C above and 10°C below this temperature.

The temperature was varied to simulate differing cloud emissivities. The zenith angle was varied from 0 to 80

degrees. As Fig 3.7 shows, the resulting points show little dependence on both zenith angle and cloud emission.

The slope of the line in Fig. 3.7 is dependent on the temperature and moisture profiles of the atmosphere

and on the placement of the observer. For reference, the dashed line in Fig 3.7, represents the line of perfect agreement between the broadband and 11 $\mu$m EBT which would result if sub-cloud atmospheric effects were ignored. As seen in Fig 3.1, the LW CRSF is near zero outside of the 8-14 $\mu$m atmospheric window. As Fig. 3.8 shows, the emission outside of the atmospheric window occurs in the first few hundred meters of the atmosphere, and therefore acts as constant offset which keeps the broad-band ebt higher than the 11 $\mu$m ebt. The observed linear relationship between the two ebt values results from the 11 $\mu$m ebt being linearly related to the integrated 8-14 $\mu$m atmospheric window ebt. The resulting slope in Fig. 3.7 is less than unity since the 11 $\mu$m spectral region is more transparent, or equivalently more sensitive the presence of clouds, than the 8-14 $\mu$m atmospheric window as a whole.
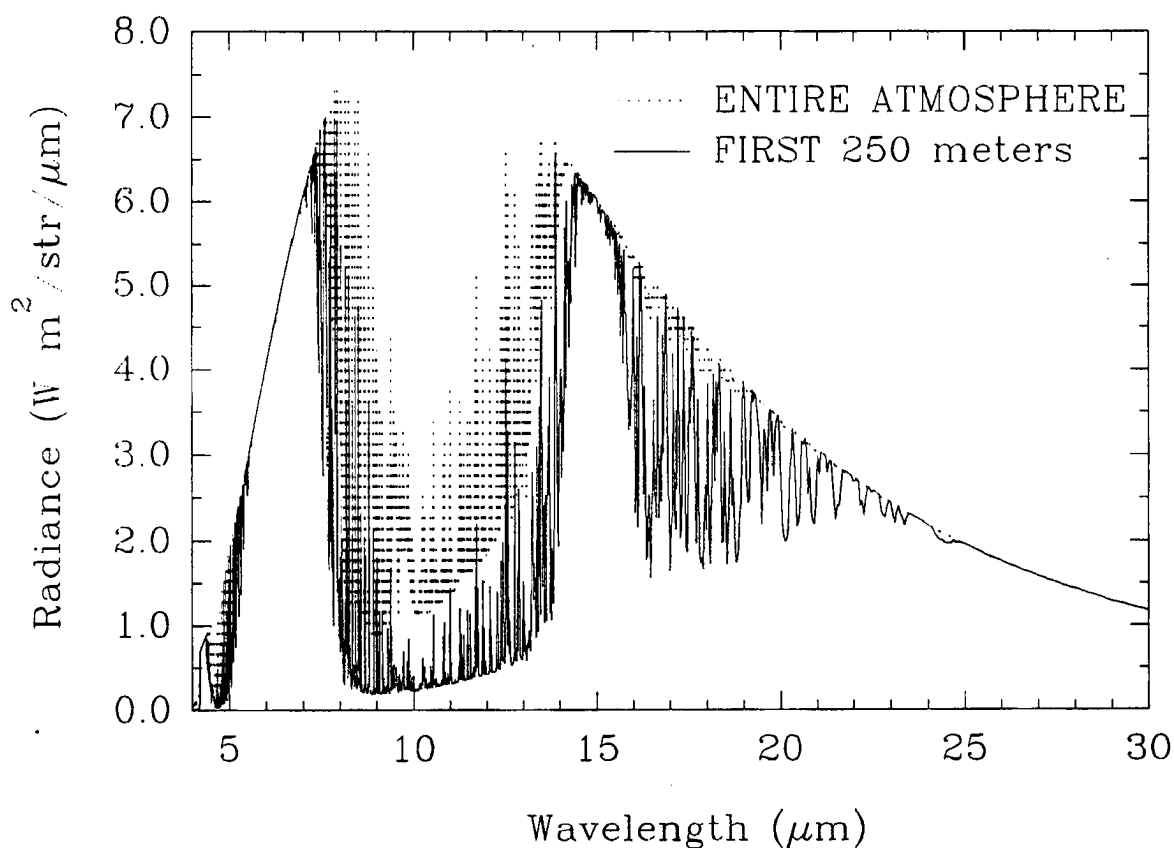


Fig 3.8 Relative Contribution of the first 250 meters to the total zenith downwelling surface radiance for ASTEX from MODTRAN

## 3.7  A Discussion of the Non-scattering Assumption

As stated in Section 3.2, the model developed in this chapter neglected the process of scattering in longwave radiative transfer. This section will explore the ramifications of that assumption. The process of scattering was neglected to allow the radiance along a line-of-sight to be calculated knowing only the absorption and emission properties along that particular line-of-sight. If scattering from other lines-of-sight needed to be accounted for, the problem would become significantly more complicated and numerically difficult. The nonscattering assumption implies a single scattering albedo, $\omega_o$, of zero. To explore the validity of this assumption, Mie code results are presented for water droplets of differing radii in Fig. 3.9. As Fig. 3.9 shows, clouds composed primarily of droplets larger than 1 $\mu$m in diameter, will have $\omega_o$'s significantly larger than zero and scattering will have a noticeable effect on the radiative transfer, especially for optically thin media. The anisotropy of the scattering, given by the value of the asymmetry parameter, g, also increases with increasing droplet radius.

Knowing that typical mean droplet radii for marine boundary layer clouds, the clouds studied in Chapters 5 and 6, fall between 3 and 10 $\mu$m and that scattering is significant at 11 $\mu$m for these droplet radii, the validity of the nonscattering assumption should be questioned. To study the effect of scattering on radiative transfer at 11 $\mu$m, a 16-stream adding doubling radiative transfer code was used. The scattering properties were taken from the Mie code results of Irvine and Pollack (1969) and simulated a water cloud composed of 10 $\mu$m droplets.

To study the effect of scattering on infrared transfer, the 16-stream adding code was used to generate net flux profiles in the presence and absence of scattering. The modelled clouds had a temperature of 280 K and the underlying surface had a temperature of 290 K. The clouds were imbedded in a non-interacting atmosphere and reflection from the underlying surface was ignored. Both clouds were constructed to have a downwelling effective emissivity of 0.80. The resulting net flux profiles are shown in Fig. 3.10.

As Fig. 3.10 shows, the net flux profiles through the scattering and nonscattering clouds are nearly identical. Therefore, for a plane-parallel cloud of known emissivity, the radiative transfer in that cloud can be simulated accurately by a nonscattering model if the modelled optical depth of the cloud is reduced. It is assumed that radiative transfer with finite clouds can also be simulated with scattering by adjusting the optical depth in a similar manner. Since most of the clouds modelled in this study are optically thick, these scattering effects are
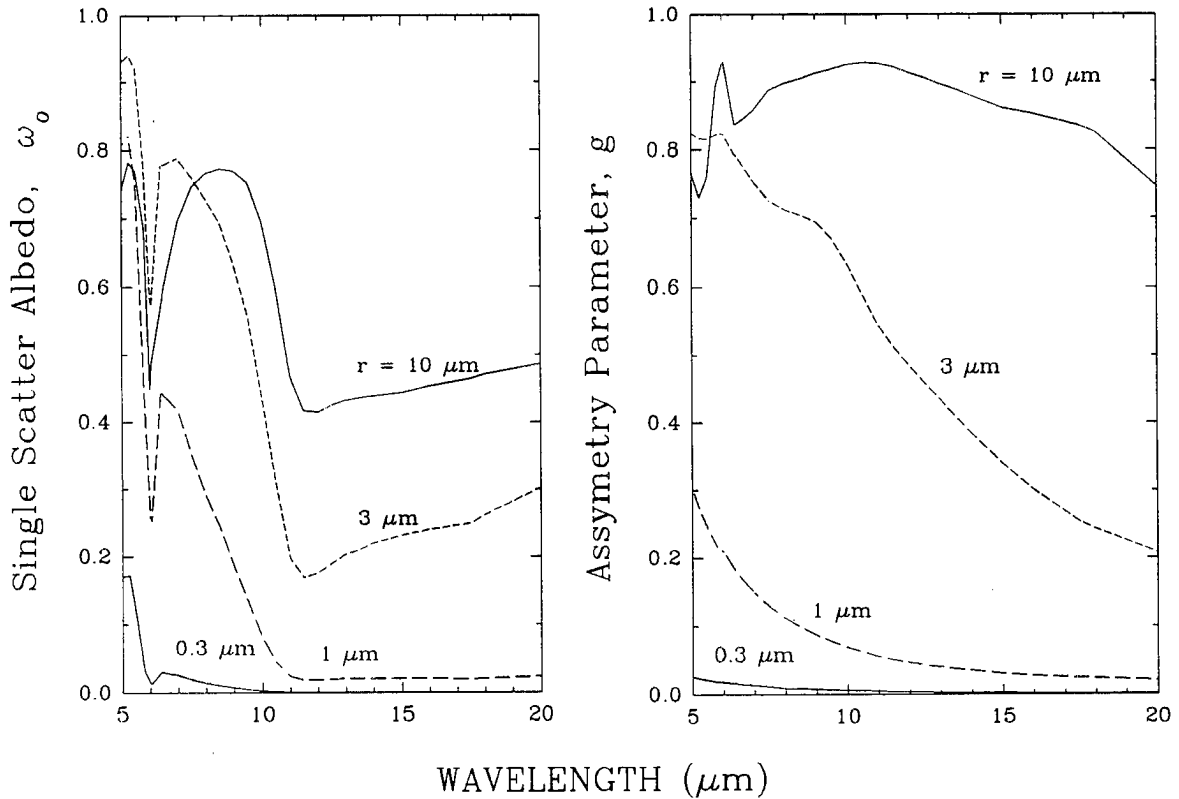
**Fig. 3.9** Mie Code Results for Water Droplet of Differing Radii from Irvine and Pollack, 1968

minimized.

## 3.8 Some Model Results

Even though Chapters 4, 7 and 8 deal with specific applications of this model, two modelling results of general interest are presented below.

### 3.7.1 The Dominance of Cloud Macrophysical over Microphysical Properties in Longwave Radiative Transfer

Even though much recent research has dealt with effect of cloud microphysical properties on longwave radiative transfer, this section show that cloud macrophyical properties can be more important than cloud microphysical properties in determining the transfer of longwave radiation in partial cloudiness conditions. To show this, consider a control case consisting of clouds with aspect ratios, a, of 0.5 and a vertical optical depths, $\tau$, of 4. The variation of the downwelling flux from a layer of these clouds versus the cloud fraction is shown in Fig. 3.11

**Left plot:**

Optical Depth into Cloud, $\tau$

$T_{cloud} = 280$ K
$T_{sfc} = 290$ K

$\epsilon = 0.80$
$\tau_N = 2.0$
$\omega_0 = 0.46865$
$g = 0.92687$

(y-axis: 0.0, 0.2, 0.4, 0.6, 0.8, 1.0, 1.2, 1.4, 1.6, 1.8, 2.0)
(x-axis: -25, -20, -15, -10, -5)

**Right plot:**

$T_{cloud} = 280$ K
$T_{sfc} = 290$ K

$\epsilon = 0.80$
$\tau_N = 1.055$
$\omega_0 = 0$

(y-axis: 0.0, 0.1, 0.2, 0.3, 0.4, 0.5, 0.6, 0.7, 0.8, 0.9, 1.0)
(x-axis: -25, -20, -15, -10, -5)

11 $\mu$m Net Flux (W/m$^2$/$\mu$m)
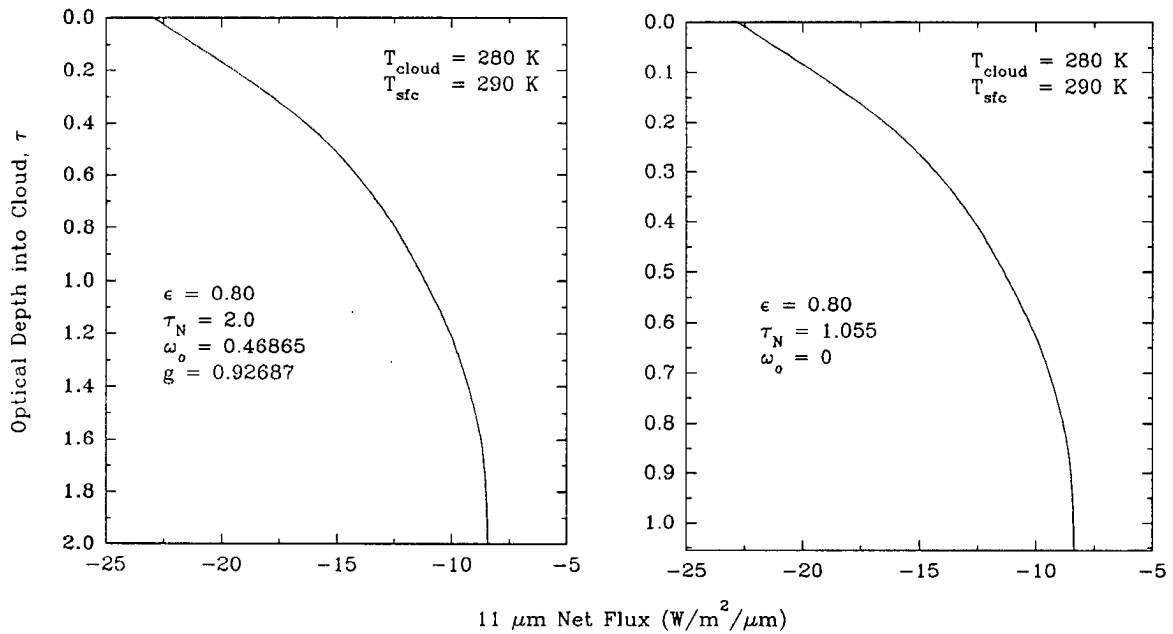
### Fig. 3.10 The Effect of Scattering on Net Flux Profiles

In these simulations, the atmosphere was assumed to be transparent and the clouds were assumed to be isothermal with a temperature of 250 K.

To explore the sensitivity of the downwelling flux to cloud microphysical changes, the optical depth of the control case was halved and doubled while the cloud's macrophysical properties, a, remained unchanged. Next the sensitivity to cloud macrophysical changes were explored by halving and doubling the cloud aspect ratio while the cloud microphysical properties, $\tau$, remained unchanged. The effect of both the macrophysical and microphysical changes of the variation of the 11 $\mu$m downwelling flux with the absolute cloud fraction. As Fig. 3.11 shows, the macrophysical changes to the control had more effect on downwelling flux than microphysical changes except for high values of the cloud fraction. The reason for the relative departure of the results from the $\tau=2$ clouds from the other results for high cloud fractions is due to the nonblack behavior of clouds with $\tau=2$.

### 3.8.2 The Effect of Cloud Geometry on the Sensitivity of the Downwelling Flux to Changes in Cloud Fraction

One parameter useful in surface budget studies is the variation in the downwelling longwave surface flux with cloud fraction. To simulate the sensitivity of this parameter to cloud geometry, the model was run with isothermal blackbody clouds of differing aspect ratio imbedded in a transparent atmosphere. The sensitivity of the

27
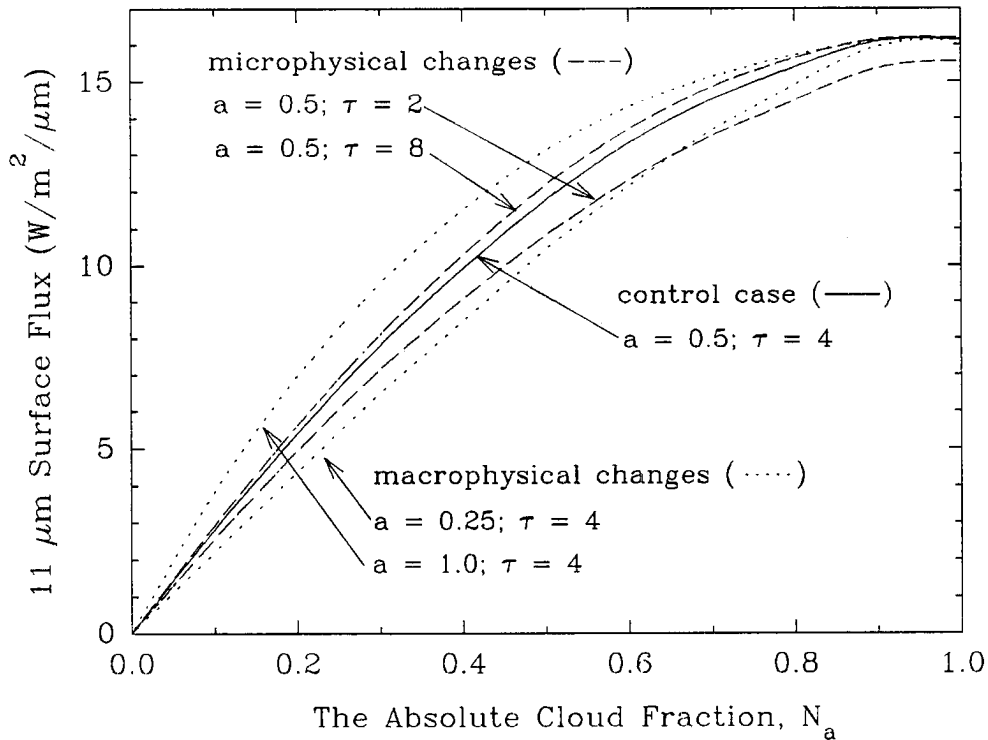
**Fig. 3.11 The effect of cloud macrophysical and microphysical properties on the 11 $\mu$m downwelling flux from a simulated broken cloud layer.**

downwelling flux, F, to changes in cloud cover for a range of cloud fractions, $N_a$, is shown in Fig. 3.12. In this figure, F represents the downwelling flux normalized by the downwelling flux for overcast sky conditions. For the case of planar clouds(a=0), $\partial F/\partial N_a$ is unity for all cloud fractions. For clouds with non-zero aspect ratios, however, the effect of the cloud sides is to increase $\partial F/\partial N_a$ for low cloud fractions and to decrease $\partial F/\partial N_a$ for high cloud fractions relative to the planar cloud results.

### 3.9 Summary

This chapter discussed a model developed for infrared radiative transfer in the presence of finite cloudiness. The cloud field was composed of uniformly spaced rectangular clouds and is imbedded in a absorbing and emitting atmosphere. Only radiative transfer at 11 $\mu$m was modelled but a limited extension of this model to broadband transfer was presented. Though the formulation of the model neglected scattering, the qualitative effects of scattering on the net infrared flux profiles were shown to be minimal.
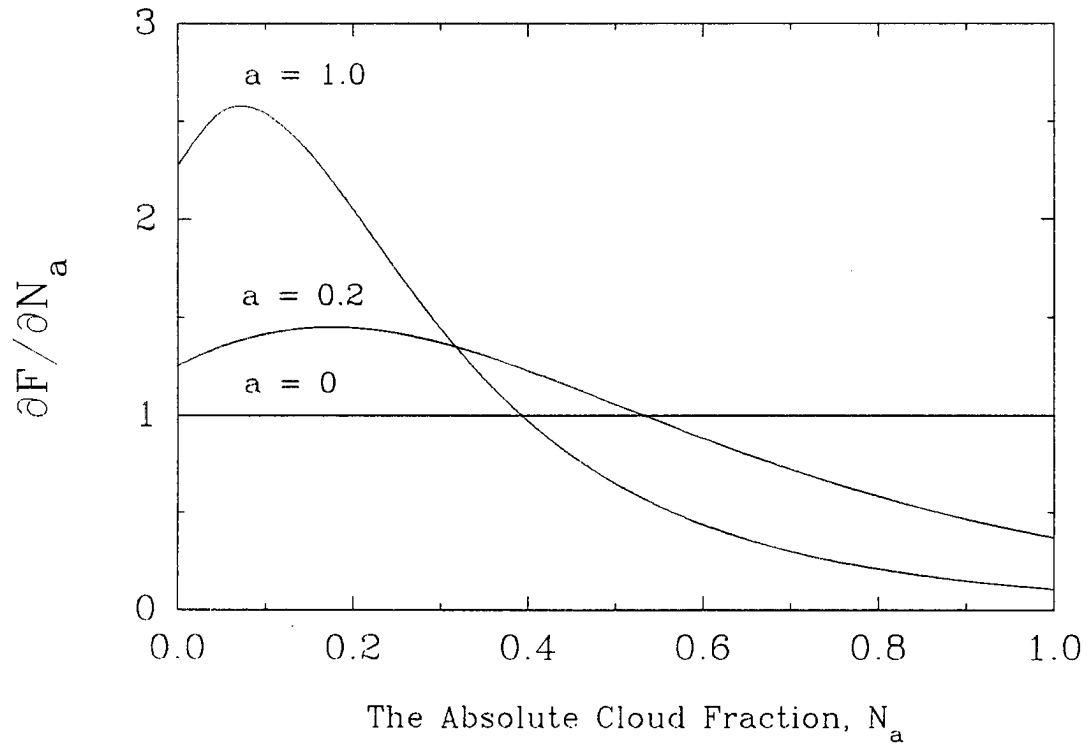
28

Fig. 3.12 The sensitivity of the 11 $\mu$m downwelling flux to cloud geometry for a simulated broken cloud layer.

Chapter 4

## EFFECTIVE VERSUS ABSOLUTE CLOUD FRACTION

Since cloud fraction is the most commonly used parameter to describe partial cloudiness, the effect of finite cloudiness on this quantity will be explored in this chapter. Traditionally the cloud fraction has been used as a closure condition for radiative transfer in broken cloudiness conditions. Stephens (1990) discusses the assumptions inherent in this application. He states that this form of closure is most appropriate for the calculation of longwave radiative transfer in the presence of black clouds. Most commonly, this closure is accomplished by using the absolute cloud fraction to weight the cloudy and clear sky contributions to obtain the observed solution. This absolute cloud fraction, $N_a$, accounts for only the areal projection of the clouds and neglects the clouds' vertical dimensions. This is the cloud fraction most often produced by models and approximates that measured by satellites.

As will be shown in this chapter, the use of $N_a$ to weight the clear and overcast fluxes can produce significant errors depending on the cloud layer geometry. One way to avoid these errors is to define an effective cloud fraction, $N_e$, that correctly weights the overcast and clear sky solutions. For example, $N_e$ can defined in terms of surface fluxes as:

$$N_e = \frac{F_{obs} - F_{clr}}{F_{ovc} - F_{clr}}$$

(4.1)

where $F_{clr}$ is the clear sky surface flux, $F_{ovc}$ is the overcast surface flux and $F_{obs}$ is the observed surface flux. By being based on hemispheric fluxes, $N_e$ is able to absorb the finite cloudiness information into one quantity. The following sections will explore the variation of $N_a$ and $N_e$ for various cloud geometries and optical depths.

30

## 4.1 The Variation of $N_e$ and $N_a$ for Black Cuboidal Clouds

In this section, the variation of the effective and absolute cloud fractions for black cuboidal cloud elements is studied. The term cuboidal refers to each cloud element's horizontal dimension being the same, which in this case was 500 meters. The vertical dimensions of the clouds were varied in order to study the effect of cloud aspect ratio, a, on the effective cloud fraction, $N_e$. Cloud aspect ratio is defined as the ratio of the mean cloud height to the mean cloud width. The absolute cloud fraction, $N_a$, was varied by decreasing the spacing between the individual cloud elements. The clouds were assumed isothermal with a temperature of 255 K and the underlying surface was assumed to behave as a black body at a temperature of 290 K. The atmosphere was assumed to be non-interactive.

Fig. 4.1 shows the variation of the effective cloud fraction, $N_e$ with the absolute cloud fraction, $N_a$, for different cloud aspect ratios. Values of $N_a$ were determined by the size and spacing of the individual cloud elements and are given by:

$$N_a = \frac{w_x}{w_x + d_x} \times \frac{w_y}{w_y + d_y} \qquad (4.2)$$

where $w_x$ and $w_y$ are the cloud element's width in the x and y directions and $d_x$ and $d_y$ are the spacing between the clouds in the x and y directions. The clouds simulated in Fig. 4.1 were all cuboidal clouds, meaning that $w_x$ and $w_y$ were equal. The term cubic cloud is reserved for clouds with aspect ratios of unity. For comparison, the results of Harshvardhan and Weinman (1982) are also plotted. Harshvardhan's results were obtained by measurements of blocks on a diffusing light table.

As Fig. 4.1 shows, the value of $N_e$ is always greater than the value of $N_a$ except at the extreme bounding cases of clear and totally overcast conditions. The sensitivity of $N_e$ to $N_a$ is largest for $N_a < 0.5$ and decreases for larger values of $N_a$ due to the shading of cloud elements by other cloud elements as they approach each other. The sensitivity to aspect ratio is largest for small aspect ratios.

Comparison of the two results in Fig. 4.1, shows the Harshvardhan results to produce lower $N_e$ for all $N_a$ and a. As a model check, the theoretical results for an absolute cloud cover of 0.50 are plotted for aspect ratios of 0.5 and 1.0. The theoretical values are obtained through empirical view factor calculations (Incropera 1980) for blocks arranged so that each block corner touches another block resulting in an absolute cloud fraction of 0.50.

31
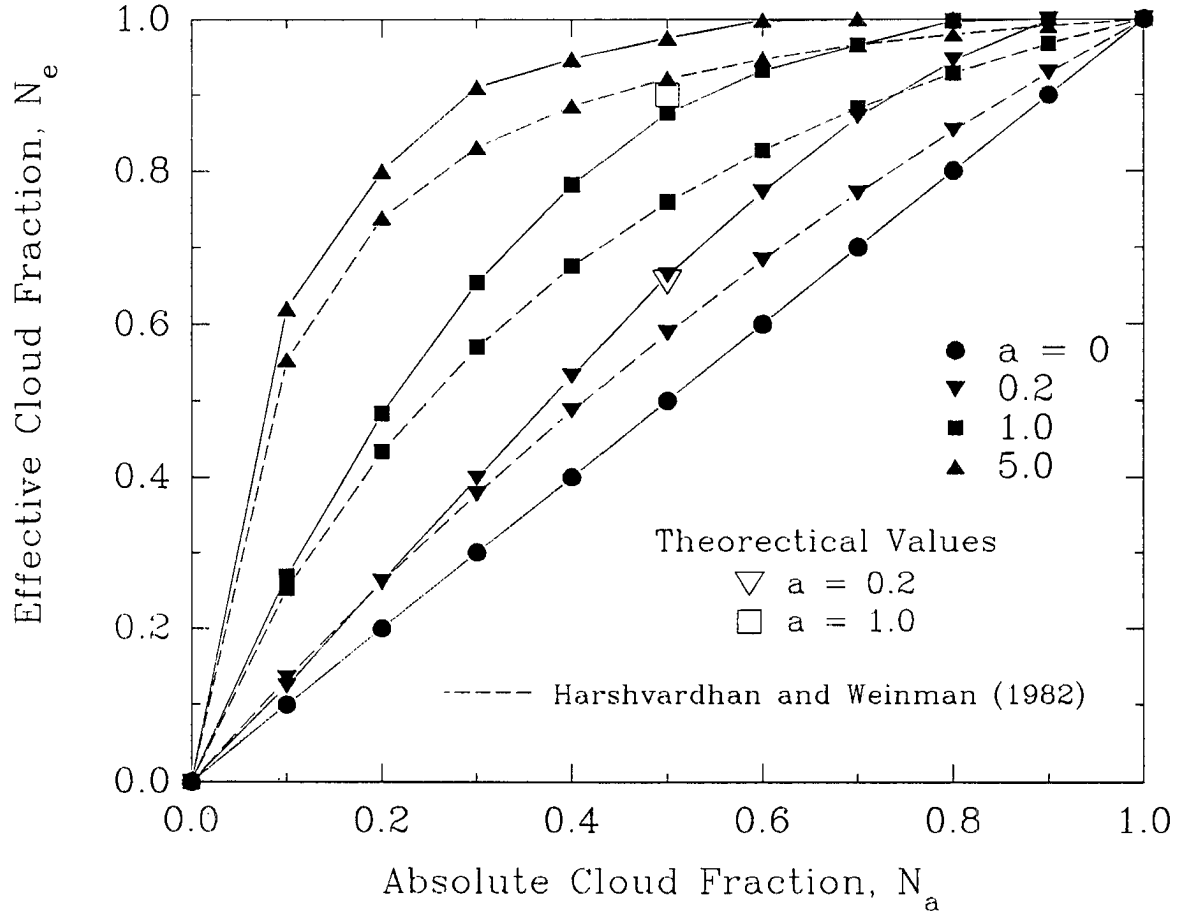
Fig 4.1 Variation of $N_e$ with $N_a$ for differing cloud aspect ratios, a. Cloud layer is a regular array of blackbody cuboidal clouds imbedded in a non-interacting atmosphere.

The theoretical values are close to the modelled solutions. Due to the apparent underestimation of $N_e$ by Harshvardhan's measurements, the parameterization presented in that paper has been modified to fit the results obtained here. Fig. 4.2 shows this modified parameterization in which $N_e$ is calculated as a function of $N_a$ and a as given by:

$$N_e^{geom} = \frac{[1+1.27a(1+5.75N_a)]N_a}{1+1.27aN_a(1+5.75N_a)}$$

(4.3)

Since the above parameterization is dependent only on the cloud geometry, the effective cloud fraction from this parameterization will be titled $N_e^{geom}$ to distinguish between $N_e$ values that account for such effects as sub-cloud moisture, variable cloud liquid water contents and non-isothermal clouds.
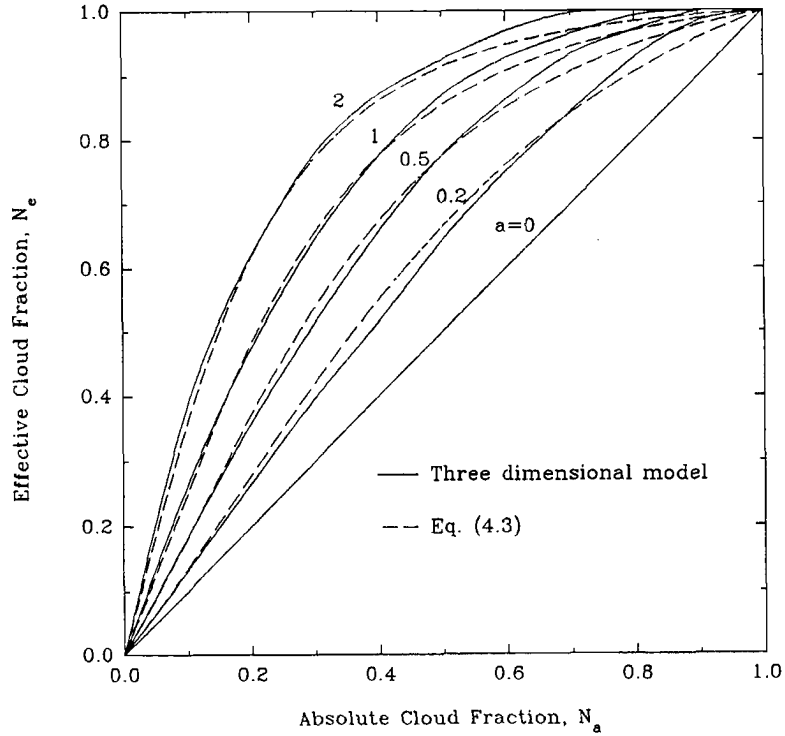
**Fig. 4.2 Comparison of the variation of $N_e$ and $N_a$ for black cuboidal clouds as predicted by the three dimensional model and Eq. (4.3).**

### 4.1.1 The Use of a Probability of a Clear Line-of-sight to $N_e$

Instead of modelling radiative transfer in three dimensions directly, one dimensional models can be used which incorporate the broken cloud field statistically. One common approach, shared by Niylisk (1972) and Ellingson (1982), was to incorporate a probability of a clear line-of-sight function, $P(\Theta)$, directly into the one dimensional radiative transfer equation. For example, using a probability of a clear line-of-sight in describing the downwelling flux below a cloud layer gives:

$$F^-(Z) = 2\pi \int_0^1 P(\theta) \, I_{clr}(z,\theta) \, \cos(\theta) \, \sin(\theta) \, d\theta + \qquad (4.4)$$

$$2\pi \int_0^1 [1-P(\theta)] \, I_{ovc}(Z,\theta) \, \cos(\theta) \, \sin(\theta) \, d\theta$$

33

where $I_{clr}$ and $I_{ovc}$ are the clear and overcast radiances respectively and $\Theta$ is the zenith angle. Azimuthal symmetry is inherent in this approach. If the clear sky radiance is assumed to be negligible and the clouds are assumed to behave as isothermal blackbodies, then an expression for $N_c$ using this probability of a clear line-of-sight function is:

$$N_\theta = 2 \int_0^{\frac{\pi}{2}} [1 - P(\theta)] \cos(\theta) \sin(\theta) \, d\theta \qquad (4.5)$$

In Ellingson (1982), the probability of clear line-of-sight function was generated assuming the clouds were right circular cylinders which were distributed along the lower boundary according to a Poisson distribution. In Fig 4.3, the probability of a cl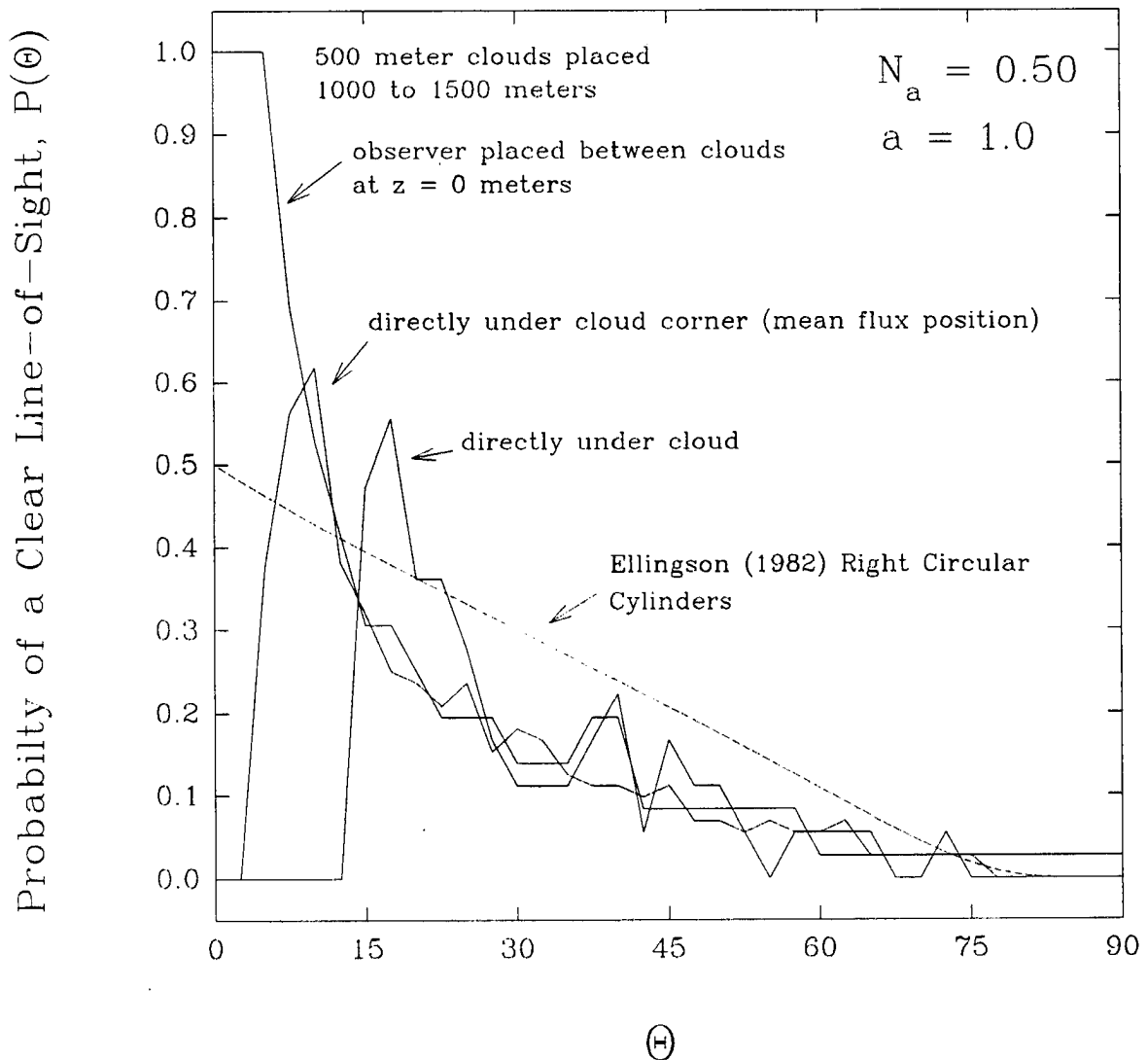ear line-of-sight functions from Ellingson (1982) and the model described in Chapter 3 are presented for comparison. The cloud aspect ratios of both simulations were unity but the clouds modelled in this study were cuboidal. The absolute cloud fraction in both simulations was 0.50. To show the dependence on the observer position, the model was run with the observer being directly under a cloud, directly between clouds and at the mean flux position. The mean flux position is the location where the observed flux approximates the horizontally averaged flux on at that level.

As shown in Fig. 4.3, the probability of a clear line-of-sight function generated by Ellingson (1982) produced significantly higher values than that modelled by this study. The present model produced an exponential decrease in P with increasing $\Theta$ while Ellingson's results show an almost linear decrease in P with $\Theta$. A similar linear decrease of P with $\Theta$ was shown by Niylisk (1972). The values of $N_c$ calculated by Ellingson and Niylisk are accordingly significantly lower than the values produced by the model developed in Chapter 3. Since the model used in this study produced $N_c$ values that agreed with theoretical values, the validity of these probability of clear line-of-sight function should be questioned. In the future, direct measurements of $P(\Theta)$ should be used to validate these probability of clear line-of sight functions used by Niylisk and Ellingson.

**Fig. 4.3** Comparison of Probability of Clear Line-of-Sight Functions for Isothermal Blackbody Cuboidal Clouds to Results from Ellingson (1982)

## 4.2 The Variation of $N_e$ with $N_a$ in Non-black Clouds.

The previous results have all been for clouds that behaved as isothermal blackbodies. In this section, the effect of optically thin clouds on the relationship between $N_e$ and $N_a$ will be explored. For this simulation, the cloud layer consisted of a regular array of cubic (a=1) clouds which extended to infinity in all directions. In addition, the cloud liquid water content was assumed to be vertically and horizontally homogeneous and the atmosphere was assumed to be non-interactive. Due to the homogeneity of the cloud liquid water, the optical depths, $\tau_n$, along each cloud face were identical.

Fig 4.4 shows the effect of varying $\tau_n$ on the relationship between $N_c$ and $N_a$. As mentioned by Harshvardhan and Weinman (1982), finite clouds approach blackbody behavior for values of $\tau_n$ greater than 10. In addition, the variation of $N_c$ with $N_a$ becomes more linear for smaller values of $\tau_n$. Assuming a mass absorption coefficient, $k_{abs}$, of 0.13 $m^2/g$ at 11 $\mu m$, a finite cloud would need a liquid water path of approximately 80 $g/m^2$ to be considered a blackbody. Since liquid paths lower than 80 are observed in marine stratocumulus, Duda et al. (1991), the practice of modelling finite marine stratocumulus as blackbodies in longwave radiative transfer in the 8-14 $\mu m$ window region is questionable.

## 4.3 The Effect of Non-cuboidal Cloud Shapes

To date, the variation of the effective and absolute cloud fractions has been studied only for cloud geometries that are cuboidal (Liou and Ou, 1981; Harshvardhan and Weinman ,1982) or right circular cylinders (Ellingson, 1981; Niylisk ,1972). In this section, the results for clouds with differing horizontal dimensions are compared to the results obtained above for cuboidal clouds. For this purpose, the clouds are again assumed to behave as blackbodies immersed in a non-interacting atmosphere.

Fig. 4.5 shows the comparison of the variation of $N_c$ and $N_a$ for cloud elements that are infinite rectangular cylinders. The mean aspect ratio for each cloud element was varied from 0.5 to 1 with the cloud dimensions being varied from 250 to 500 meters in the x direction and the z direction being held constant at 500 meters for both runs. The cloud elements extended to infinity in the y direction. The results are plotted along with the results obtained for black cuboidal clouds with mean aspect ratios of 0.5 and 1.0. The comparison shows the cloud field composed of infinite cylinders and cuboids give the same results as long as the mean aspect ratio of each element is the same. The results for infinite cylinders were shown since they represent the most non-cuboidal geometry, but any rectangular shape could have been used with the same results. The results show that the cuboidal results are applicable to other geometries as along as the mean aspect ratio of the cloud field is known.

Effective Cloud Fraction, $N_e$

1.0

0.8

0.6

0.4

0.2

0.0

$\tau_n = 0.2$

1.0

2.0

5.0

10.0

black

0.0    0.2    0.4    0.6    0.8    1.0

Absolute Cloud Fraction, $N_a$
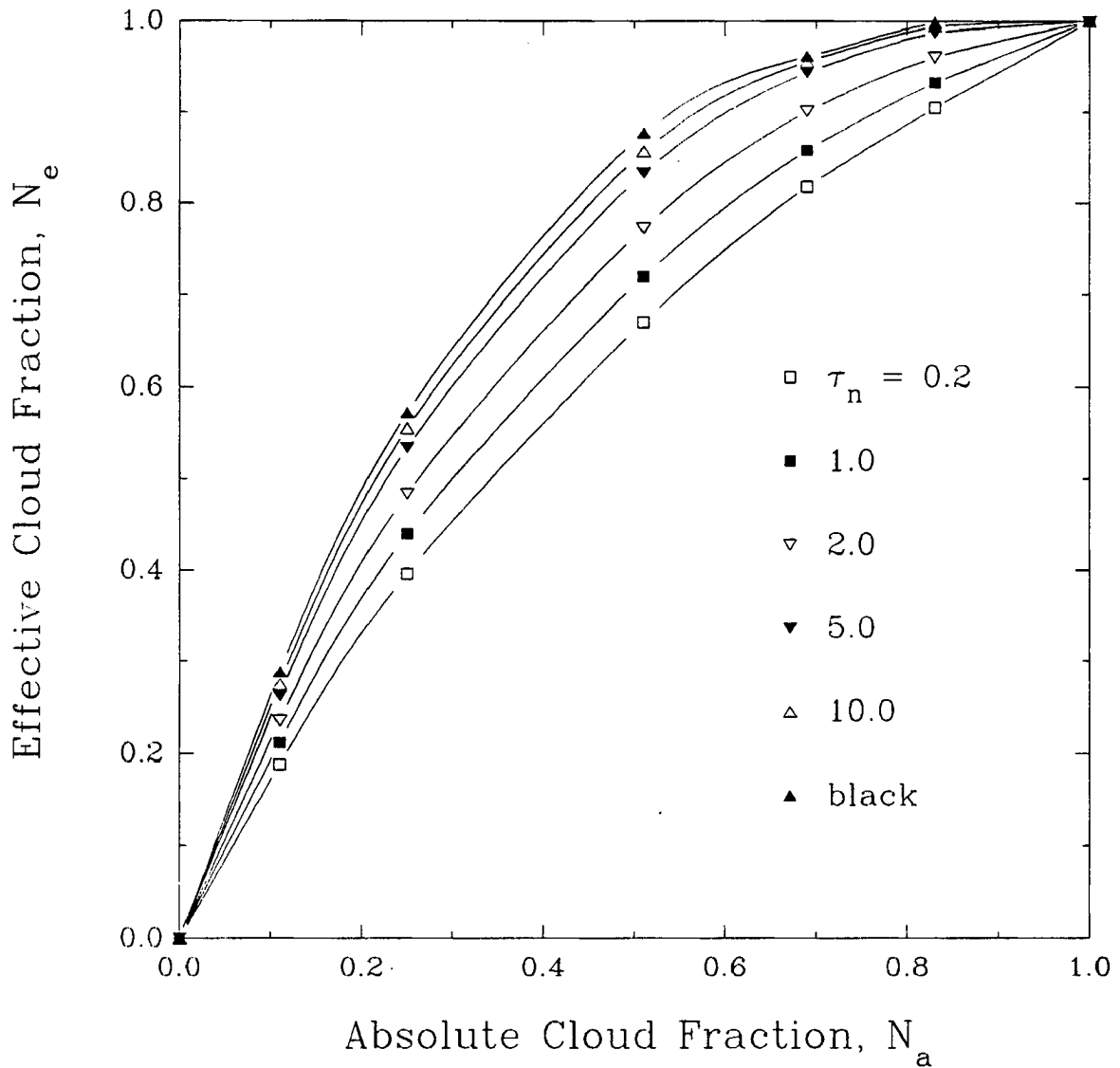
Fig. 4.4 Variation of $N_e$ with $N_a$ for clouds of differing optical depths, $\tau_n$. Cloud layer consists of a regular array of cubic clouds imbedded in a non-interacting atmosphere.

## 4.4    The Effect of Interacting Atmospheres on the Variation of $N_e$ with $N_a$

Up to this point, the atmosphere in which the cloud field was imbedded was assumed to be non-interacting. The effect of atmospheric absorption and emission on the variation of the effective and absolute cloud fraction has never been documented. The inclusion of a realistic atmosphere will affect the results in three ways. First, the addition of sub-cloud emission and absorption dictates that the solution will be dependent to some degree on the position of the observer with respect to the cloud layer. Second, clouds imbedded in a realistic atmosphere are not
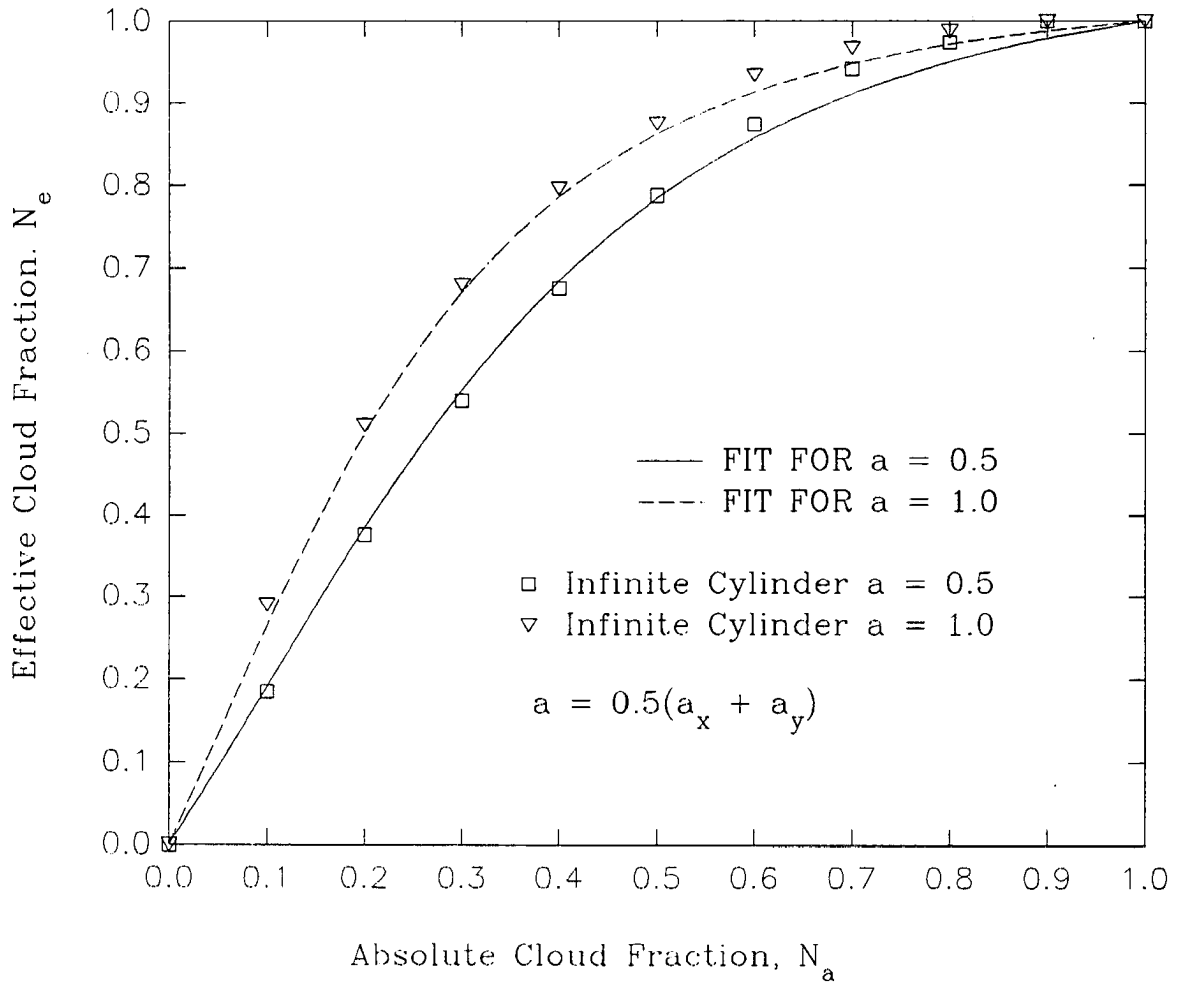
**Fig 4.5 Comparison of cuboidal and infinite cylinder results**

isothermal as assumed previously. Third, due to the varying spectral absorption properties in the longwave region, the solution will be dependent on the spectral range used.

To study the atmospheric effects on the variation of $N_e$ with $N_a$, the composite ASTEX atmosphere was used. The water vapor optical mass of this atmosphere was 2.16 $g/m^2$. In addition to this standard composite sounding, three other versions were used. One had its water vapor optical mass doubled to 4.33 $g/m^2$, another had it's optical mass halved to 1.08 $g/m^2$ and lastly one sounding had all water vapor removed. The temperature profiles in each sounding were identical. The cloud layer was again constructed of cuboidal clouds of an aspect ratio of unity and linear dimension of 500 meters. The cloud layer was placed between 1000 and 1500 meters and the observer was on the surface.

### 4.4.1 The Sensitivity of $N_e$ to Atmospheric Water Vapor

Fig 4.6 shows the effect of the sub-cloud moisture on the variation of $N_e$ with $N_a$. All values of $N_e$ in this figure were calculated at 11 $\mu$m. The ordinate in Fig 4.6 is the difference between the modelled $N_e$ and the $N_e$ predicted using the parameterization given in Eq. (4.3). Remember that this parameterization was developed with the model using an isothermal, non-interacting atmosphere so that $N_e$ is a function of the cloud layer geometry only. Fig 4.6 shows that the inclusion of atmospheric effects always reduces the value of $N_e$. This reduction in $N_e$ is due to the sub-cloud moisture preventing clouds at low zenith angles from affecting the surface flux.
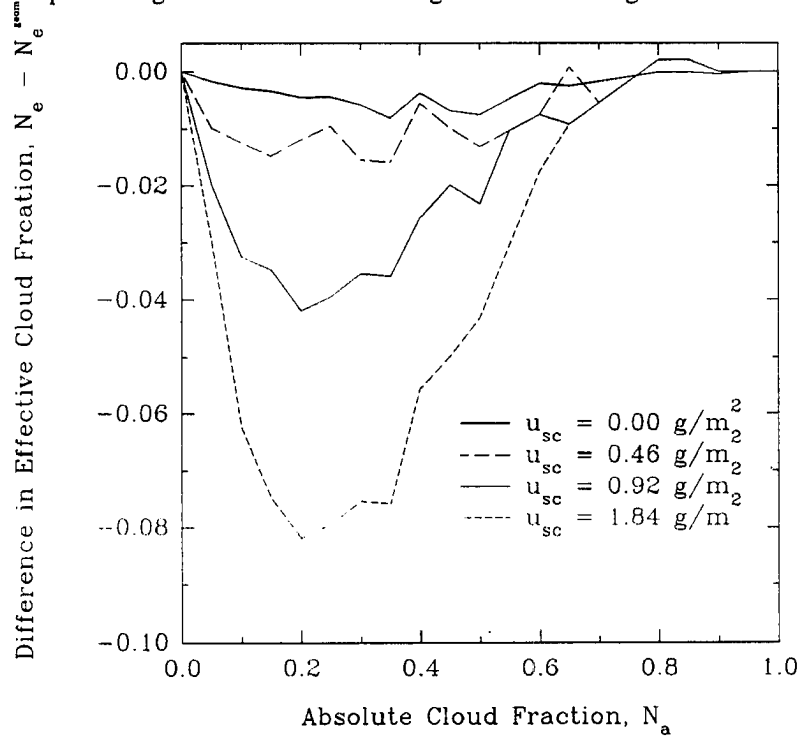
Fig. 4.6 Percentage error in $N_e$ from assuming an isothermal, non-interacting atmosphere.

Due to height dependence of the relative amount of water vapor between the observed and the cloud layer, the inclusion of the effects of atmospheric water vapor also causes $N_e$ to have a height dependence. Fig. 4.7 shows the vertical variation of $N_e$ for a cloud layer positioned between 1000 and 1500 meters. The simulated cloud layer consisted of cubic cloud with uniform liquid water contents of 0.2 $g/m^3$. The clouds were imbedded in an atmosphere determined by the standard ASTEX composite temperature and moisture sounding. The values of $N_e^+$ and $N_e^-$ are obtained applying Eq. (4.1) to the upward and downward directed fluxes respectively. $N_e^+$ becomes meaningless below the cloud as does $N_e^-$ above the cloud layer. The variation of $N_e^{+/-}$ in the cloud layer is discussed

in Section 8.3. As Fig. 4.7 shows, both $N_e^+$ and $N_e^-$ decrease with increasing distance from the cloud layer. This decrease is due the increase in the amount of water vapor between the observer and the cloud layer as the observer moves away from the cloud layer.
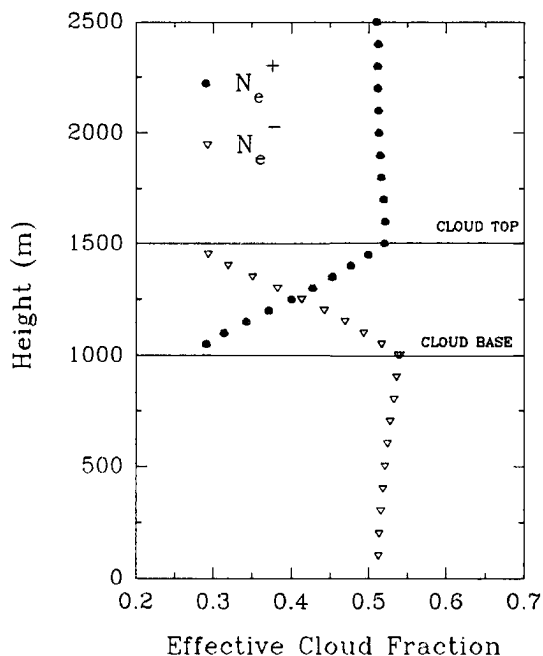


Fig. 4.7 Height dependence on $N_e$ for a cloud layer positioned from 1000 to 1500 meters in the standard ASTEX atmosphere. Cloud layer consists of a regular array of cuboidal clouds with $N_A$ = 0.25.

### 4.4.2 The Effect of Non-isothermal Clouds on $N_e$

The results in Fig 4.6 for $u_{sc}$ = 0, directly show the errors associated with the isothermal assumption in the parameterization of $N_e$ given by Eq. (4.3). Compared with the errors introduced by sub-cloud moisture, the error introduced by the isothermal assumption is virtually negligible. Since these results pertain to boundary layer clouds only, the non-isothermal nature of clouds with larger vertical dimensions might need to be accounted for.

### 4.4.3 The Spectral Nature of $N_e$ Calculations

To study the spectral variation of $N_e$, model runs were performed using a monochromatic spectral region of 11 $\mu$m and a broad-band spectral region of 4-50 $\mu$m. The 11 $\mu$m spectral region is relatively transparent to water vapor while the broad-band region is very opaque to water vapor. Fig. 4.8 shows the difference in $N_e$ for the two

spectral regions. The cloud configuration is identical to that in Section 4.4.1 and the unmodified composite ASTEX sounding was used. The results show that broad-band $N_e$ values are always smaller than the 11 $\mu$m values. This is analogous to the model runs in which the sub-cloud moisture was varied in Section 4.4.1. Since the broad-band region is more opaque to water vapor, there is a stronger sub-cloud moisture effect in the broad-band calculations of $N_e$ than in the 11 $\mu$m calculations.
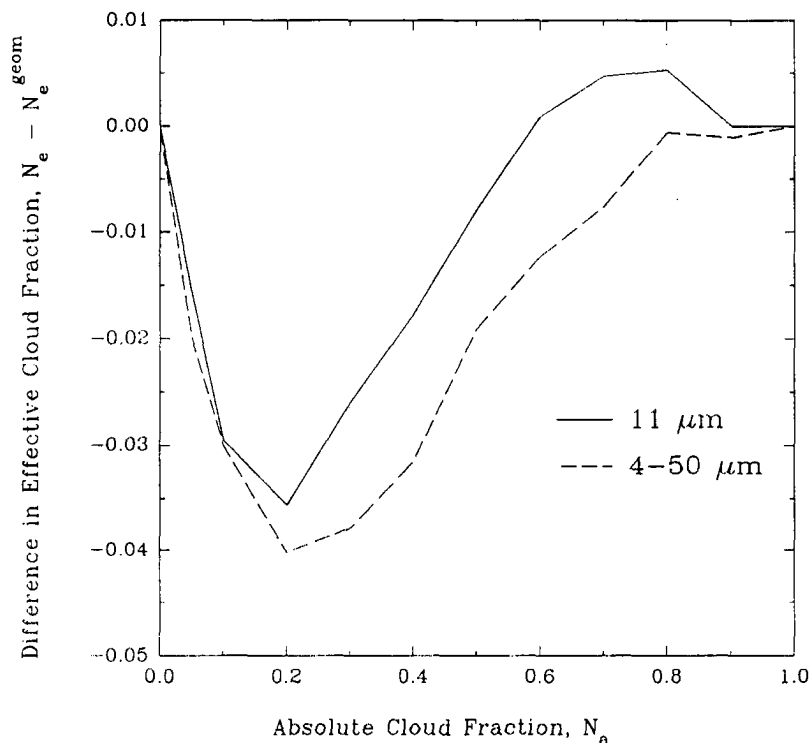


Fig. 4.8 The effect of differing spectral regions on the calculation of $N_e$.

## 4.5 Summary

This chapter used the model in developed in Chapter 3 to study the variation of $N_e$ with $N_a$. A parameterization was developed for $N_e$ based on $N_a$ and the cloud aspect ratio, a for isothermal, black cuboidal clouds in a non-interacting atmosphere. The parameterization was extended to non-cuboidal cloud fields when the mean cloud aspect ratio of the entire cloud field was used. The effect of non-black clouds was examined and the results were compared with more sophisticated model results. The inclusion of an interacting, non-isothermal atmosphere was shown to have a significant effect, especially during periods of sparse cloud cover.

Chapter 5

OBSERVED FINITE CLOUD EFFECTS DURING ASTEX

The results from the previous chapter have shown that the inclusion of finite cloud effects can significantly alter the fluxes exiting a partially cloudy layer. In this chapter, the sensitivity of the surface flux to finite cloudiness is explored through direct observations. The measurements used in this chapter were taken during the ASTEX phase of the FIRE field experiments. To the author's knowledge, these are the first measurements used to show directly the effect of clouds' finite dimensions on the observed longwave surface flux.

5.1    The ASTEX Dataset

The ASTEX (Atlantic Stratocumulus Transition Experiment) phase of Fire (First ISCCP Regional Experiment) occurred during June 1992 on the Island of Porto Santo in the Madeira Islands. The ASTEX Porto Santo data sets are described by Cox et al. (1992). This region, shown in Fig. 5.1, was chosen since it offered the opportunity to study the transition of the stratus to stratocumulus regime. This region was highly suitable for studying finite cloud effects since low single layer broken cloud fields were commonly observed and contamination from higher level clouds such as cirrus was rare. The surface measurement site was located on top of a 100 meter cliff near the northwest corner of the island.

5.2    Instrumentation

Two longwave radiometers were operated continuously on the Porto Santo site. One radiometer was an Eppley pyrgeometer and was used to measure the broad-band (4-50 $\mu$m) downwelling surface flux. The pyrgeometer was calibrated by the method of Albrecht and Cox (1976). The second radiometer installed at Porto Santo was a PRT-6 bolometer and was used to measure the downwelling 11 $\mu$m radiance. The PRT-6 had a 2° field

of view and was oriented vertically throughout the entire measurement period. Calibration in terms of 11 $\mu$m radiance was accomplished by using the intermittently run 5-15 $\mu$m Bomem interferometer.
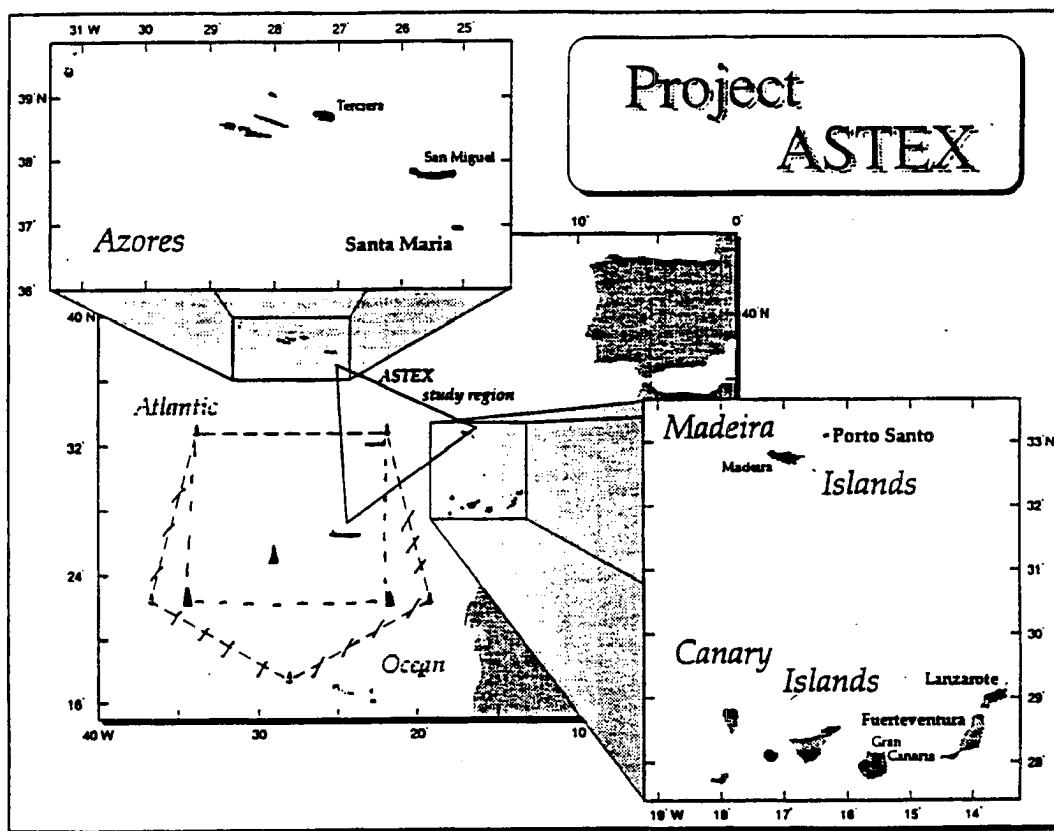


Fig. 5.1 The geographical location of the June 1992 ASTEX phase of FIRE II. (taken from the ASTEX Operations Plan)

## 5.3 Methodology

In order to observe the finite cloud effects in the ASTEX longwave radiometer data, values of the effective cloud fraction, $N_e$, were calculated using Eq. (4.1). To use Eq. (4.1) however, values of the clear sky longwave surface flux, $F_{clr}$, and the overcast surface longwave flux, $F_{ovc}$, were needed. The values of $F_{obs}$, the observed longwave surface flux, were supplied by the pyrgeometer. The goal of this section therefore is to describe the methodology used to provide the estimates of $F_{clr}$ and $F_{ovc}$.

### 5.3.1 Determination of Clear Sky Longwave Fluxes

Due to the rare occasions of totally clear skies at ASTEX, direct clear sky flux measurements were insufficient to calculate $N_e$ continuously. To obtain the temporal resolution in the clear sky surface flux needed, LOWTRAN 7 was used. LOWTRAN 7 was run to generate values of $F_{clr}$ for every sounding launched which corresponds to roughly one value every three hours. Data between soundings were linearly interpolated between the nearest sounding times. Fig. 5.2 shows the variation of $F_{clr}$ as modelled by LOWTRAN 7 for the entire ASTEX period. Since several totally clear periods did exist, these measured clear sky values are plotted against the corresponding LOWTRAN clear sky values in Fig. 5.3. Note there is generally good agreement except for some points where the measurements were noticeably higher than LOWTRAN. This is probably due to atmospheric haze or low horizon cloudiness effects in the measurements that were not accounted for in the LOWTRAN 7 runs. As Fig 5.3 shows, the use of LOWTRAN to generate the clear sky flux values introduced an error source of approximately 5 $W/m^2$ which is roughly the same magnitude of the errors associated with the actual pyrgeometer measurements.

### 5.3.2 Determination of Overcast Sky Longwave Fluxes

Once the measured and clear sky surface fluxes were known, only the overcast sky surface flux was needed to calculate $N_e$. The overcast sky flux, $F_{ovc}$, is defined as the downwelling longwave surface flux in the presence of overcast sky conditions. One method of obtaining the overcast sky flux would be to measure the cloud base, and assume that the cloud behaves as a blackbody emitting at the measured cloud base temperature. In addition, the

44
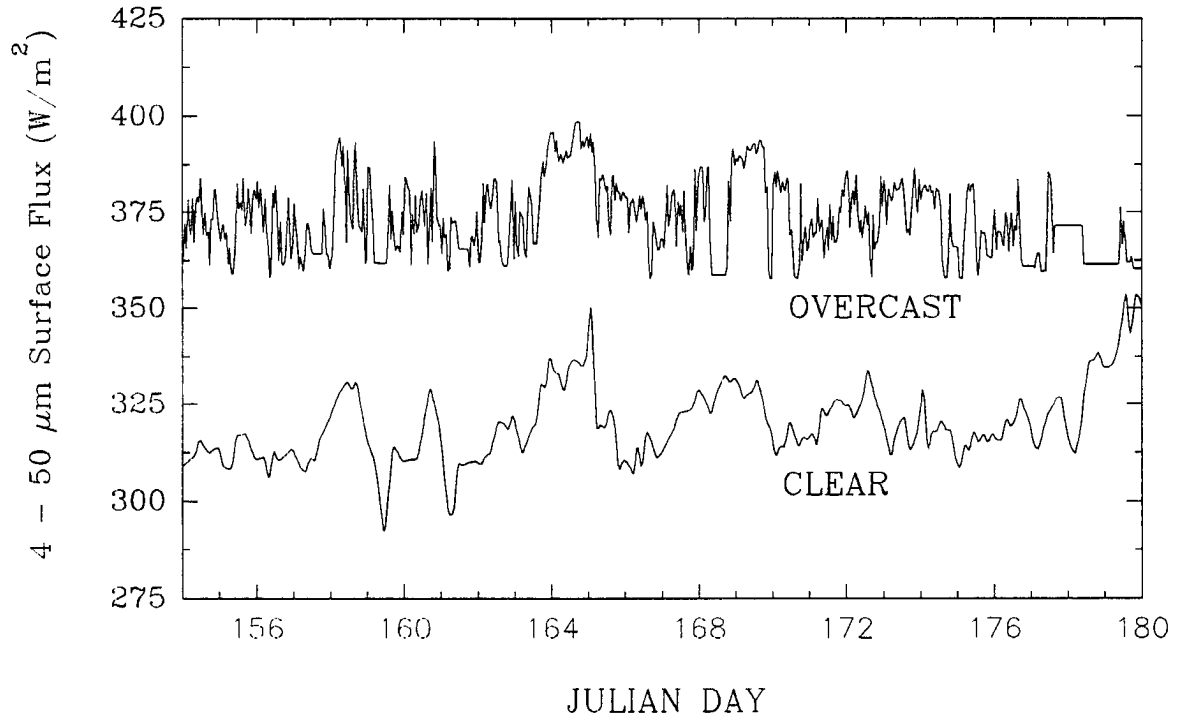
Fig 5.2 Variation of the clear and overcast sky longwave surface fluxes during ASTEX.
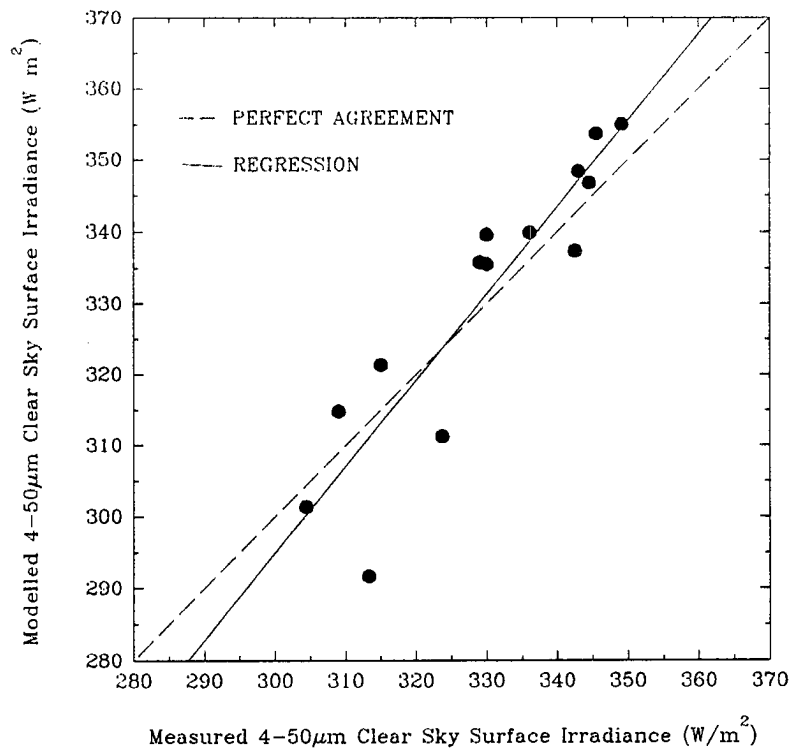


Fig 5.3 Comparison of measured and modelled clear sky surface fluxes

transmission and emission of the subcloud layer would also need to be included. To avoid the uncertainties and computational requirements of this method, another method was chosen which was based directly on measurements. Though conceptually simpler than the above method, the method described below will provide valuable insights into the longwave radiative behavior of stratocumulus clouds during ASTEX.

The method chosen to deduce $F_{ovc}$ relies directly on the comparison of narrow-band and broad-band measurements. In this method, $F_{ovc}$ was calculated directly from cloudy measurements of the PRT-6, which is a $2°$ field of view 11 $\mu$m radiometer. Cloudy PRT-6 measurements were those measurements where the $2°$ field was filled by cloud. The algorithm that determines cloudy from non-cloudy PRT-6 measurements was based on the strength of the measured signal. In the algorithm, any PRT-6 measurement with an 11 $\mu$m equivalent brightness temperature greater than 250 K was considered cloudy. This threshold in the algorithm was of sufficient strength to filter out partially cloudy views and views filled by cloud edges that have low emissivities. In using direct measurements to estimate $F_{ovc}$, the uncertainty in the haze effects present in the estimations of $F_{clr}$ is avoided.

To determine the relation between the cloudy narrow-band measurements and the overcast surface flux, the PRT-6 and pyrgeometer were compared for known overcast conditions. This comparison is shown in Fig. 5.4. Note the relatively small degree of scatter of the points. This is remarkable considering the cloud bases of the various points range from 200 to 1800 meters. The solid line plotted is a polynomial fit to the data. The dashed lines are discussed below. Using this fit, any PRT-6 measurement that is deemed cloudy, can be used to determine $F_{ovc}$. Even during periods of sparse cloud cover, cloudy PRT-6 measurements are common enough to give a fine temporal resolution in the $F_{ovc}$ data.

Also plotted in Fig. 5.4, are dashed curves corresponding to different values of 11 $\mu$m emissivity. The curves were produced using LOWTRAN by placing a horizontally infinite target at different heights and calculating the broad-band surface flux and the 11 $\mu$m zenith radiance. The target assumes the temperature of the environment and the sounding used is a composite of all the ASTEX soundings. The broad-band emissivity of the target was assumed to be unity and the effects of the atmosphere above the target were ignored. Comparison of the ASTEX data with the LOWTRAN simulations shows that the 11 $\mu$m emissivity of the ASTEX clouds was significantly less than unity and seemed to decrease with increasing cloud base height. This systematic decrease in the 11 $\mu$m

46
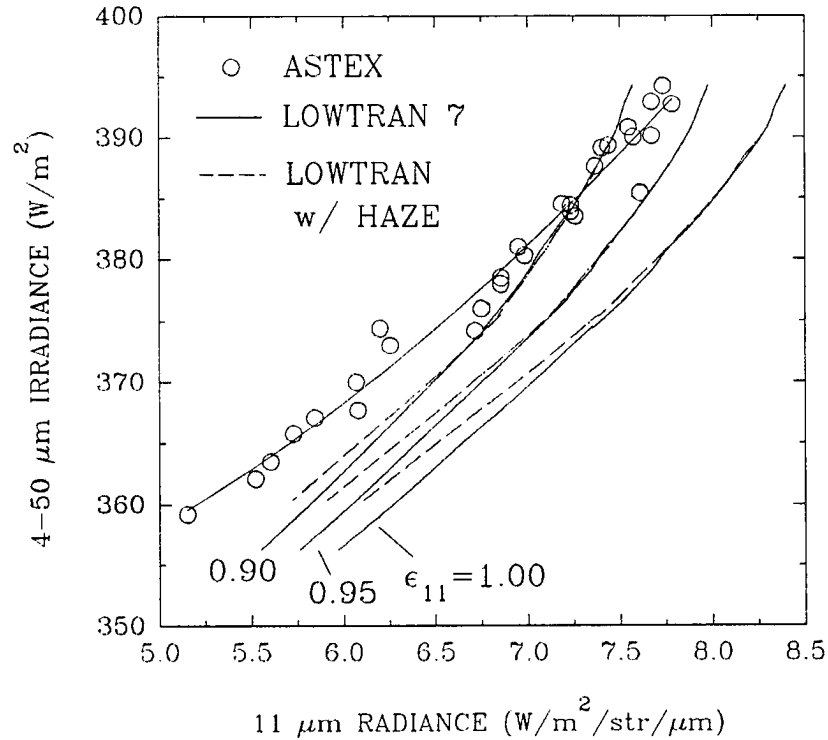
Fig. 5.4 Measured and modelled variation of the broad-band overcast surface flux with the 11 $\mu$m surface radiance.

emissivity with cloud base height is shown in Fig. 5.5. This decrease in emissivity is probably due to a decrease in cloud thickness as the cloud base increases. These data are the same as those plotted in Fig. 5.4.

## 5.3.3 Effect of Cirrus

The methodology described above neglects the presence of higher level clouds such as cirrus. To explore the sources of error with this assumption Fig. 5.6 was produced with a simulated cirrus cloud placed at 7.50 km in an average ASTEX sounding. The lower cloud field was composed of 500 m black-body cubes with a cloudbase of 1.0 km. The emissivity of the cirrus layer was varied from 1.0 to 0.5 as shown in the figure. Fig. 5.6 shows cirrus effects will cause a significant overestimation of the effective cloud cover only when the absolute cloud cover is below 0.5 with the overestimation increasing with decreasing $N_a$. Since cirrus conditions were present for approximately for 10% of the ASTEX period, they were ignored in this analysis.
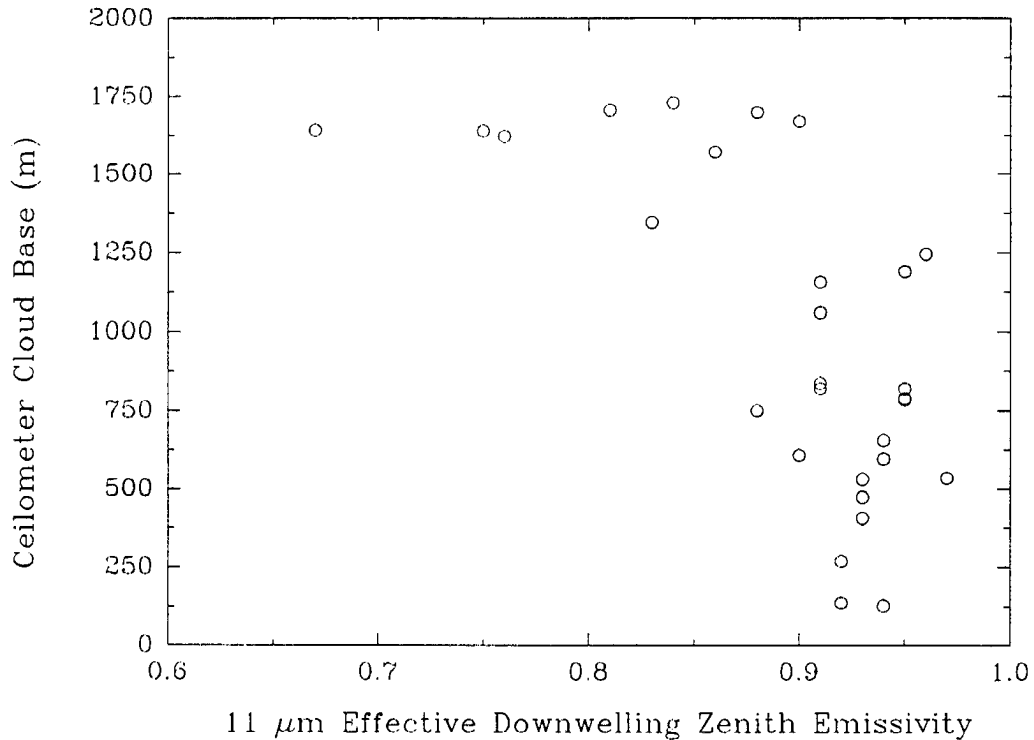
**Fig. 5.5** Variation of 11 μm downwelling effective emissivity with cloud base height for overcast conditions at ASTEX.

## 5.4 The ASTEX Observations

This section presents results from the surface data collected during June 1992 at ASTEX. Most values such as the surface fluxes, the cloud base and the liquid water path were measured every two minutes except for the 11 μm radiance which was recorded every ten seconds.

### 5.4.1 The Longwave Cloud Radiative Surface Forcing (LW CRSF)

One quantity of paramount importance to surface energy studies is the longwave cloud radiative surface forcing (LW CRSF). The LW CRSF is defined as the difference in the longwave surface fluxes measured under cloudy, $F_{meas}$, and clear, $F_{clr}$, sky conditions. Symbolically, this can be expressed as:

$$LW\ CRSF = F_{meas} - F_{clr} \qquad (5.1)$$

Values of LW CRSF are always positive with the largest values occurring in the presence of low, thick clouds as was frequently the case during ASTEX. A histogram of the hourly averaged values of the LW CRSF observed
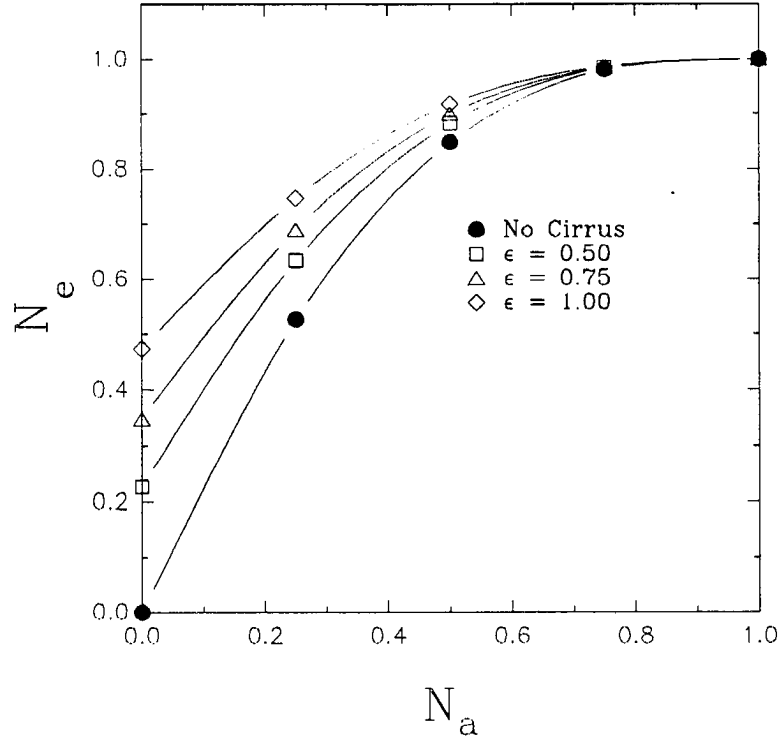
**Fig. 5.6 The sensitivity of $N_e$ to the presence of cirrus**

during ASTEX is shown in Fig. 5.7. Average hourly LW CRSF values greater than 70 $W/m_2$ were observed. The daily averaged values for the ASTEX period are shown in Fig. 5.8. These daily mean values range from near 0 $W/m^2$ for clear days to near 60 $W/m^2$ for predominantly overcast days.

## 5.4.2 The Enhancement of the LW CRSF due to Finite Cloud Effects

One useful means of showing the effect of the cloud's finite dimensions on the LW CRSF is to calculate the ratio of the observed surface forcing, LW CRSF, to the surface forcing that would be measured if the three dimensional clouds were replaced by flat two dimensional planar clouds, LW $CRSF_{2D}$. As shown below in Eq. (4.2), the ratio of these two values of LW CRSF is identical to the ratio of $N_e$ to $N_a$.

$$\frac{LW\ CRSF_{3D}}{LW\ CRSF_{2D}} = \frac{N_e\,(F_{ovc}-F_{clr})}{N_a\,(F_{ovc}-F_{clr})} = \frac{N_e}{N_a} \qquad (3.2)$$

Since the ratio of $N_e$ to $N_a$ is always greater than unity, finite cloud effects always act to increase the LW CRSF

49
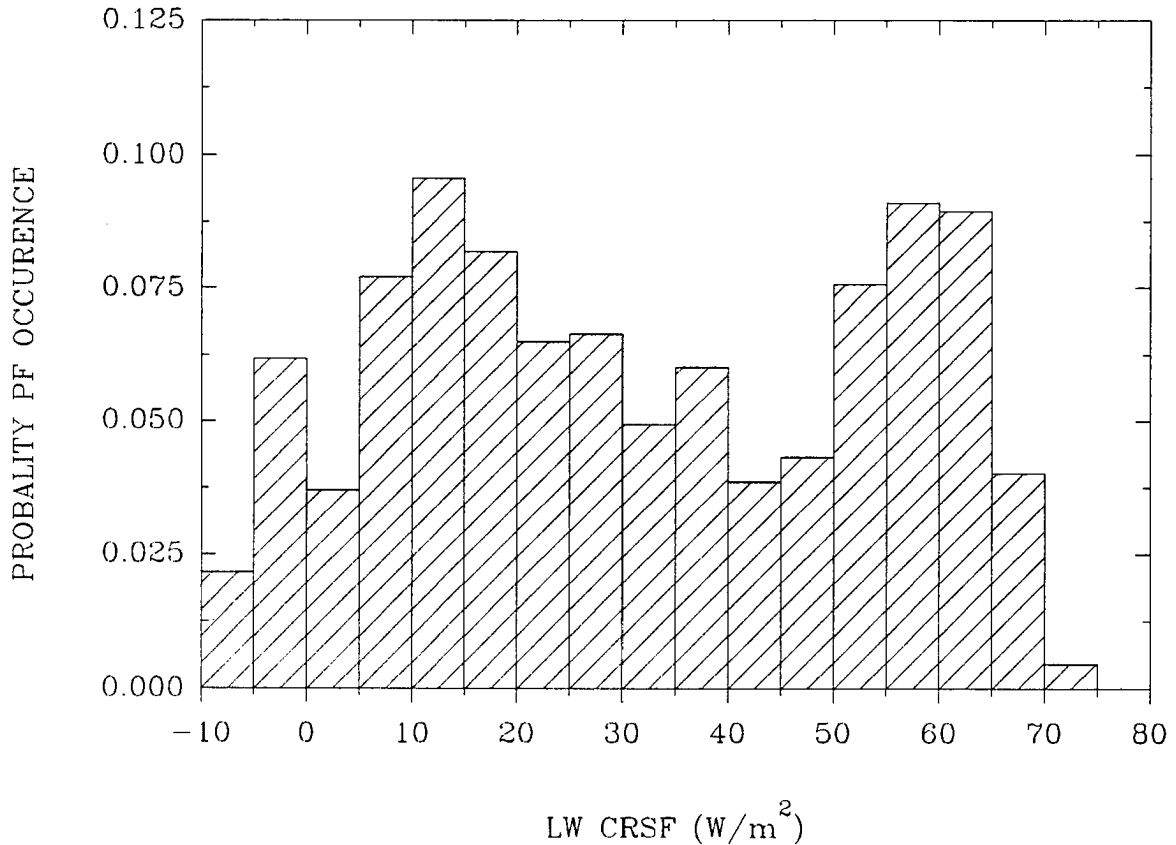
Fig 5.7  Histogram of measured hourly LW CRSF values at ASTEX

relative to the value in the presence of planar clouds.

The daily variation of the ratio of $N_c$ to $N_a$ during ASTEX is shown in Fig. 5.9. The daily values observed during ASTEX ranged from near 1 to over 2 with a period mean of 1.5. This mean value of 1.5 in the ratio of $N_c$ to $N_a$ shows that calculations of the LW CRSF during ASTEX which ignored the vertical dimensions of the cloud field would be on average one third too low. This is an issue for satellite retrieval methods of LW CRSF, since the current cloud cover estimates from satellites do not account for the vertical dimensions of the cloud fields.

Another meaningful way to demonstrate the finite cloud effects in the LW CRSF during ASTEX is to plot the difference of the measured LW CRSF and the estimated LW $CSRF_{2D}$. This difference represents the absolute increase in the LW CRSF due to the emission from the vertical edges of clouds. The daily means of the difference between the measured LW CRSF and LW $CRSF_{2D}$ is shown in Fig. 5.10. The mean value for the ASTEX period is 9 $W/m^2$ while daily values ranged from 0 to 15 $W/m^2$. Clearly, if one desires to know the surface longwave
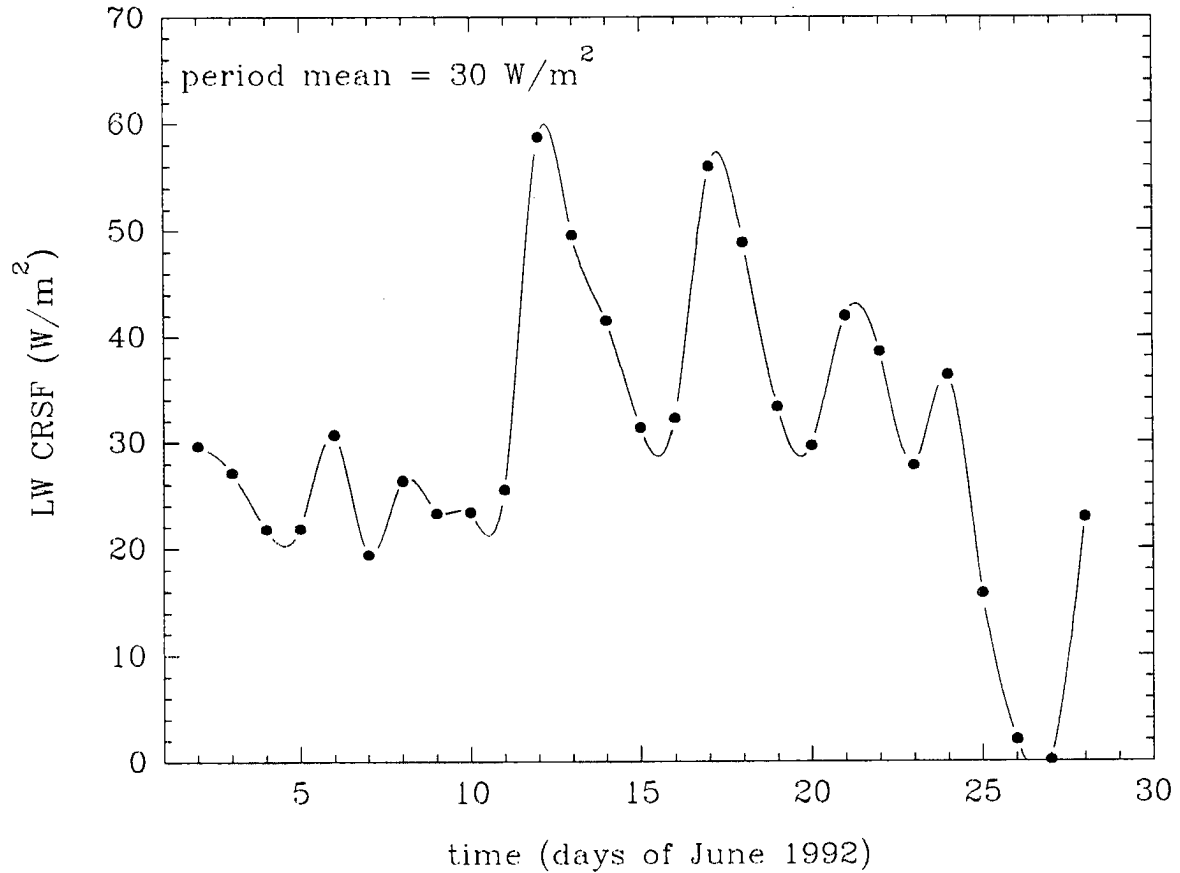
**Fig 5.8** Daily LW CRSF values for ASTEX

budget to an accuracy of 10 or 20 W/m$^2$, even on a daily basis, accounting for the cloud field's vertical dimensions is imperative.

### 5.4.3 The Effective Cuboidal Cloud Aspect Ratio

Using the parameterization of $N_c$ given in Eq. (4.3), each measured value of $N_c$ and $N_a$ can be used to retrieve an effective cuboidal cloud aspect ratio, $a_{cub}$. This aspect ratio is the aspect ratio of the clouds in a cuboidal cloud field that would possess the same $N_c$ and $N_a$ as the observed cloud field. Remember that the term cuboidal implies a cloud with equal dimensions in both the x and y directions. The variation in the mean daily acub during ASTEX is shown in Fig. 5.11. The mean value of $a_{cub}$ for ASTEX was 0.55 with the daily means ranging from near 0 for mainly overcast days to approximately 1.5 for days with sparse cloud cover.

51

## 5.4.4  Data Processing

The above results were constructed from hourly averages. No filtering was used in the construction of these hourly averages except the exclusion of erroneous measurements. From these hourly averages, approximately 10% were rejected as being unrealistic. The criteria for the rejection of these data included points where the ratio of $N_c$ to $N_a$ exceeded 10 or was below unity. The most likely cause for erroneous data were the measurements of $N_a$ taken with the PRT-6. Most of the rejected hourly averages were from periods with high ($>0.9$) or low ($<0.2$) values of $N_a$. The probable reason for these errant points was the measured zenith fractional cloudiness not being representative of the true hemispheric absolute cloudiness.

As mentioned above, ratios of $N_c$ to $N_a$ greater than 10 were excluded. These values occurred for very small values of $N_a$. Another reason for rejecting these points from the daily averages is due to enhanced sensitivity of the ratio of $N_c$ to $N_a$ to small values of $N_a$, as shown in Fig. 5.12. In addition, not only does this sensitivity
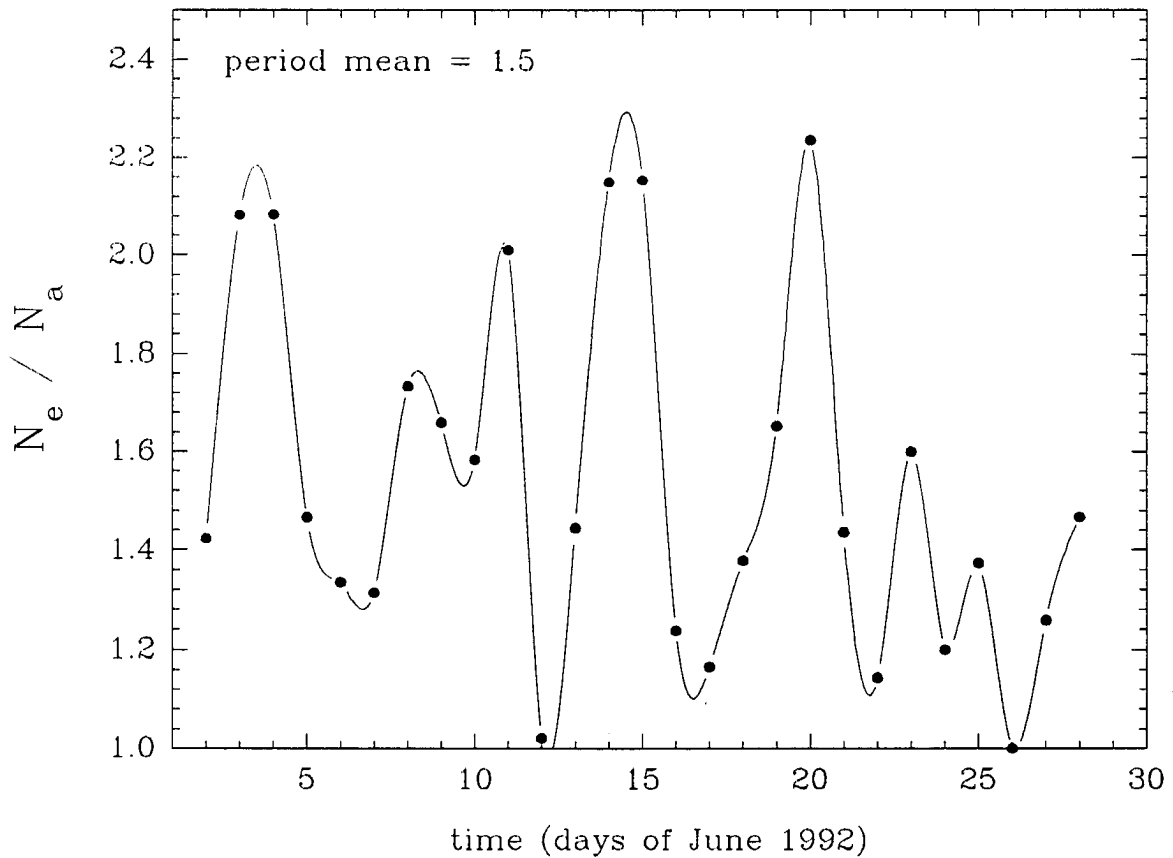


Fig 5.9  The daily values of $N_c/N_a$ at ASTEX.

52
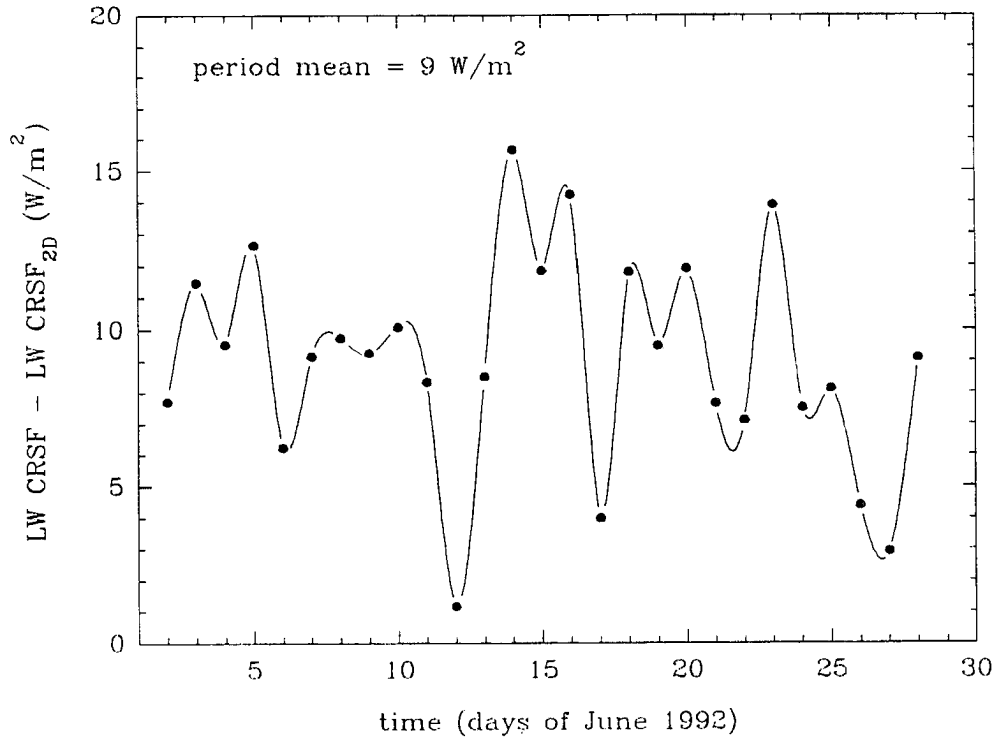
Fig. 5.10 Observed values of the difference between LW CRSF and LW $CRSF_{2D}$ during ASTEX.

increase for small values of $N_a$, but it also increases for large values of cloud aspect ratio, a. This increase in the

sensitivity with aspect ratio compounds the problem since the large values of aspect ratio and small values of $N_a$

tend to occur together. Therefore, the measurements of $N_c$ at low $N_a$ are the most prone to errors.

In addition to the hourly averages rejected at low values of $N_a$, significant numbers of hourly averages with

high values of $N_a$ were also rejected. As Fig. 5.12 shows, the sensitivity of the ratio of $N_c$ to $N_a$ was not a factor

in the rejection of these measurements. One probable cause for rejection of data with high values of $N_a$ could be

broken cloud fields that appeared overcast to the zenith looking instruments but not overcast to the hemispheric

looking instruments. Lappen (1994) reported the presence of a stationary gravity wave over the Porto Santo

experiment site which could have anchored a cloud feature over the site itself, thus producing this effect. In such

instances, values of $N_c$ that were less than the measured values of $N_a$ are possible.

53
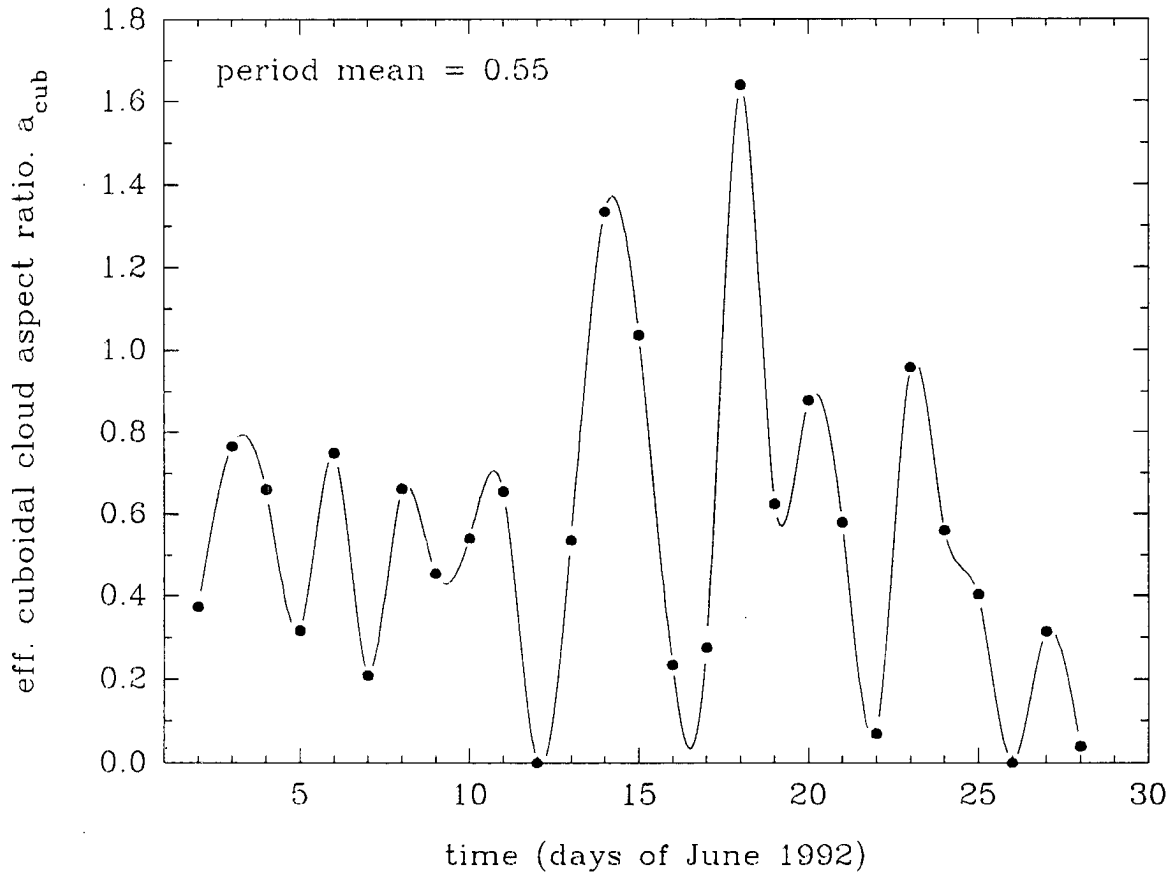
Fig 5.11 Daily averaged values of the effective cuboidal aspect ratio.

## 5.5 The Diurnal Cycle

As observed during FIRE I in the San Canalina Islands off the coast of California during 1989, a strong diurnal cycle was observed in the cloud amount and in the LW CRSF at ASTEX. The diurnal cycle in the cloud amount is shown in Fig 5.13. The maximum cloudiness tended to occur during the early morning hours with a minimum occurring in the late afternoon. This is the same phase reported in FIRE I (Minnis 1992) though the magnitude of the ASTEX cycle appears to weaker.

This diurnal cycle in the cloud fraction at ASTEX also manifested itself in the diurnal cycle in the LW CRSF data. Fig. 5.14 shows the observed diurnal cycle in the LW CRSF. There appears to be a 20 W/m$^2$ diurnal cycle in the LW CRSF data with the largest values occurring in the early morning and the smallest values occurring in the late afternoon. There is also a peak in the average daily cloud forcing shortly afternoon which is not present in the average daily cloud cover.

54
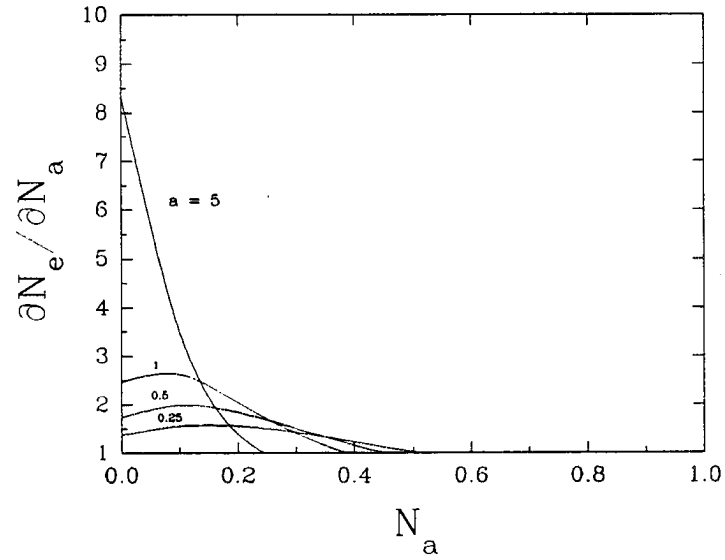
Fig. 5.12 Sensitivity of $N_e$ to changes in $N_a$ for varying cloud aspect ratios, a.
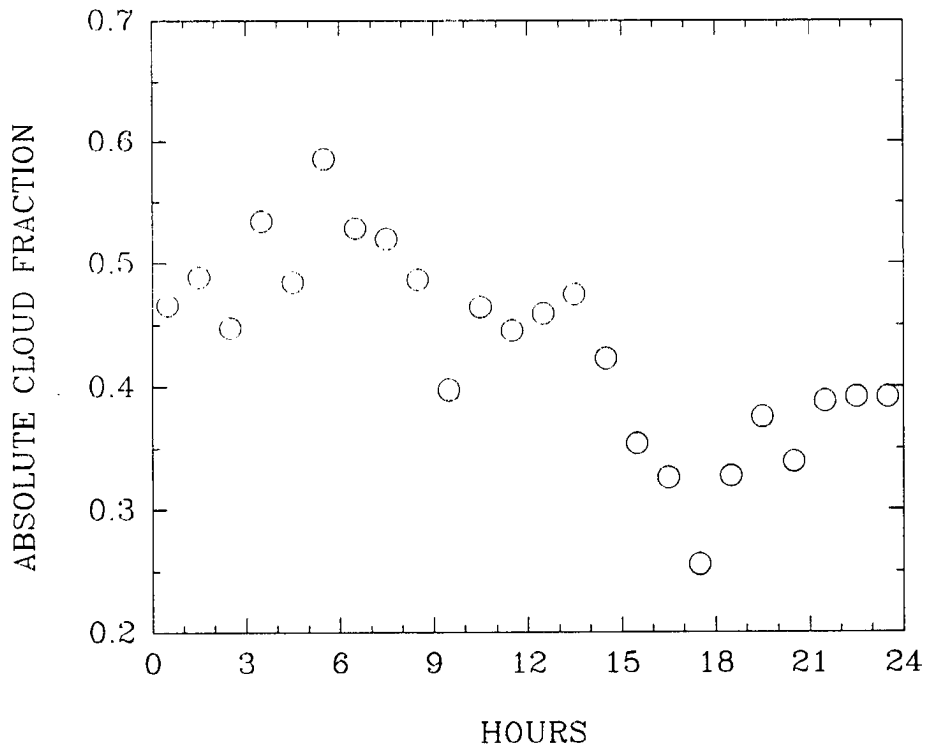


Fig. 5.13 Diurnal cycle in the absolute cloud cover, $N_a$, during ASTEX.
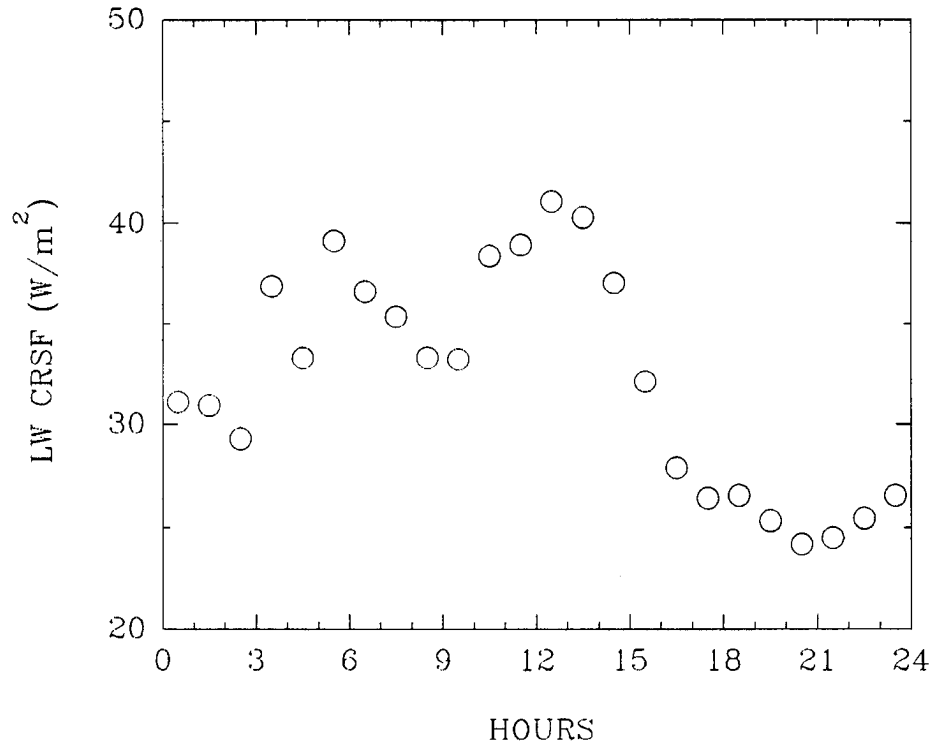
**Fig. 5.14 Diurnal cycle in the LW CRSF during ASTEX.**

## 5.6 Summary

This chapter discussed the observed role that finite cloud effects have on the LW CSRF as seen during ASTEX. A technique was described to calculate the broad-band overcast sky flux from narrow-band, narrow field-of-view measurements collected under broken cloudiness conditions. Using this technique, the average ratio of the effective and absolute cloud fractions over the entire ASTEX period was found to be 1.3. It was shown that the ratio of $N_e$ to $N_a$ also represents the ratio of the LW CRSF for three dimensional clouds to that for two dimensional clouds. The mean effective cuboidal aspect ratio for the entire period was found to be approximately 0.5. The diurnal cycle in both the cloud fraction and the LW CRSF was found to be similar to the cycle seen in Minnis (1992).

.

# Chapter 6

# A FINITE CLOUD EFFECT CASE STUDY: JUNE 14, 1992


In the previous chapter, ASTEX measurements were used to show that emission from the lateral sides of clouds accounted for about one third of the observed LW CRSF over the entire ASTEX period. In this chapter, the results from one day, June 14, 1992 will be shown in detail as an illustrative example of the role of finite cloud effects in the LW CRSF. This day was chosen since only one low layer of cloudiness was observed and the cloud cover ranged from near overcast to near clear conditions. To explore the role of cloud aspect ratio, the model developed in Chapter 3 will be applied to the data taken on June 14, 1992.


## 6.1 The Observed Cloud Cover Variations on June 14, 1992

The observed absolute cloud cover for June 14 is shown in Fig. 6.1. The diurnal cycle observed during this day has the same trend as the diurnal cycle for the entire ASTEX period, Fig. 5.15. The PRT-6 derived values of $N_a$ reached a maximum of 0.98 from 4 to 5 UTC and reached a minimum of 0.10 during the hour between 14 and 15 UTC. In addition, the variation of $N_e$ during June 14 is shown in Fig. 6.1. Note that the values of $N_e$ are significantly greater than the values of $N_a$ especially during the period from 12 to 22 UTC.


## 6.2 The Observed LW CRSF Variations on June 14, 1992

The observed variation in the absolute cloud cover, $N_a$, can be compared to the variation of LW CRSF for June 14. The values of the LW CRSF on this day, shown in Fig. 6.2, varied from 67 to 16 W/m². The pattern is similar to the cloud cover variation with higher values occurring in the morning with lower values occurring in the afternoon and evening. Note the relative maximum in the LW CRSF shortly after noon. This increase is not reflected in the absolute cloud cover which decreases sharply during the period from 10 to 14 UTC. It is

hypothesized that the reason for the lack of a corresponding decrease in the LW CRSF during this time is due to finite cloud effects. Even though the absolute cloud fraction, $N_a$, decreased dramatically, the effective cloud fraction, $N_e$, did not due to the emission from the lateral sides of the clouds. This emission from the sides of
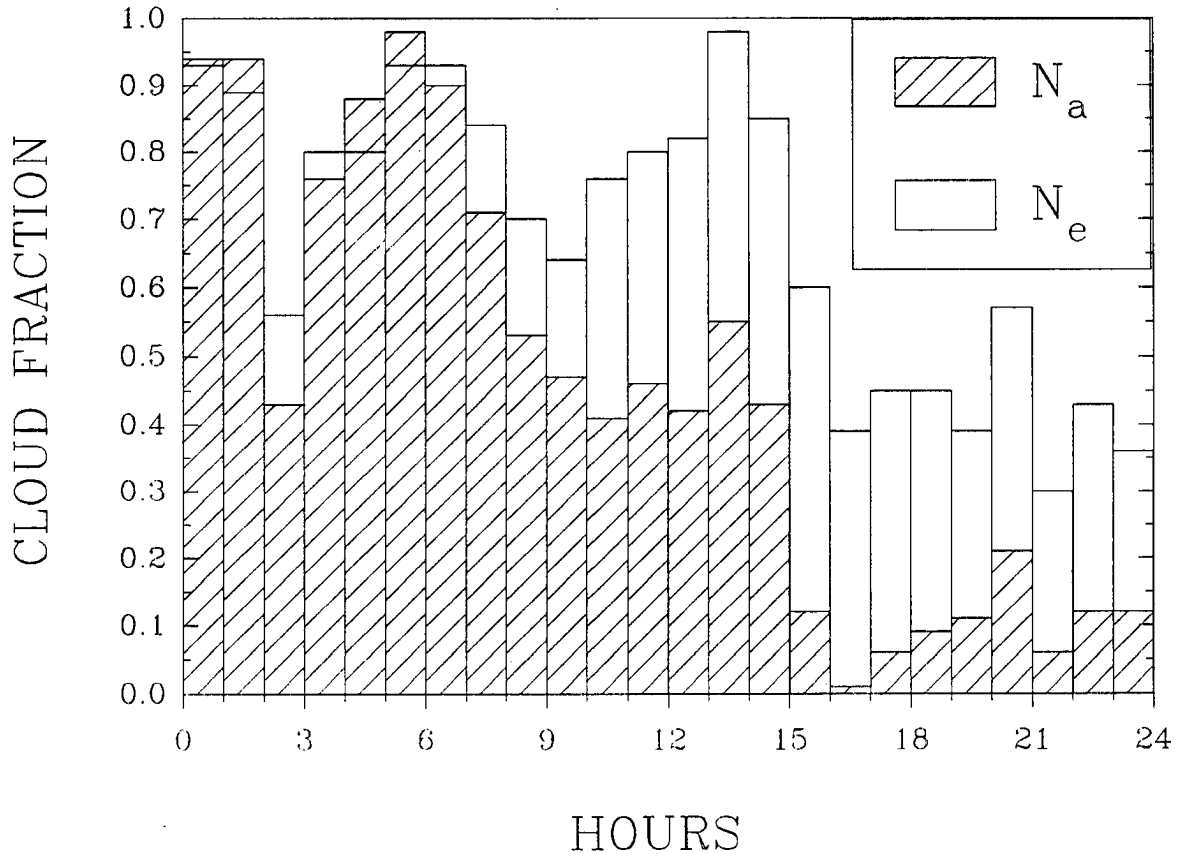


**Fig 6.1  The observed cloud fraction for June 14, 1992**

clouds acted as a buffer keeping the LW CRSF elevated. On this day, the LW CRSF did not begin to decrease dramatically until the absolute cloud fraction fell below 0.5 which occurred during the hour 14 UTC. Clearly, any algorithm that assumed a linear relationship between the LW CRSF and $N_a$ would have under predicted the LW CRSF during this period.

## 6.3  Cloud Field Aspect Ratio During June 14, 1992

For a cloud layer composed of many irregularly shaped clouds, the cloud field aspect ratio is the ratio of the mean cloud depth to the mean cloud width. Using the NOAA/WPL 8.7 mm radar, the mean cloud depth can

be determined. Fig. 6.3 shows the hourly averaged cloud top, base and depth for June 14, 1992. The cloud base on this day varied from 1300 to 570 meters and the cloud depth varied from 94 to 480 meters. Generally the clouds became lower and thinner as the day progressed.
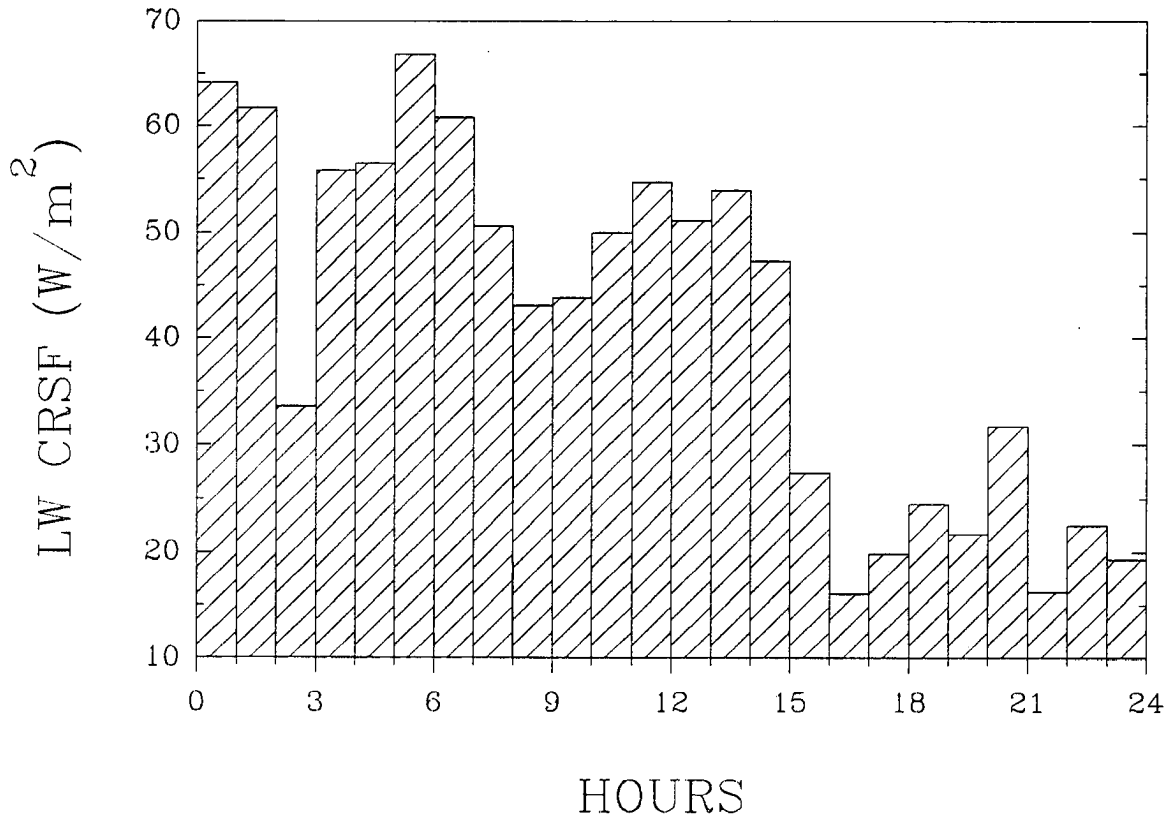


**Fig 6.2 The hourly averaged LW CRSF for June 14, 1992**

Once the mean cloud depth is known, the mean cloud width must be determined to calculate the mean cloud aspect ratio. The method chosen was to measure the cloud width using the PRT-6. This method involved using a threshold of 260 K to distinguish between cloud and clear measurements. An average time for a cloud to pass over the vertical looking PRT-6 was determined using this threshold. Assuming the clouds were uniformly distributed and that the clouds moved at the mean wind speed, the mean cloud width could be determined as the product of the cloud speed and the average time for a cloud to pass over the PRT-6. The mean wind speed was chosen to be 12 m/s from the rawinsonde data collected on June 12, 1992. Fig 6.4 shows the variation in the rawinsonde measured horizontal wind speeds through the cloud layer during June 14, 1992.

Now that an estimate of the mean cloud width is available, the mean cloud aspect ratio can be calculated.
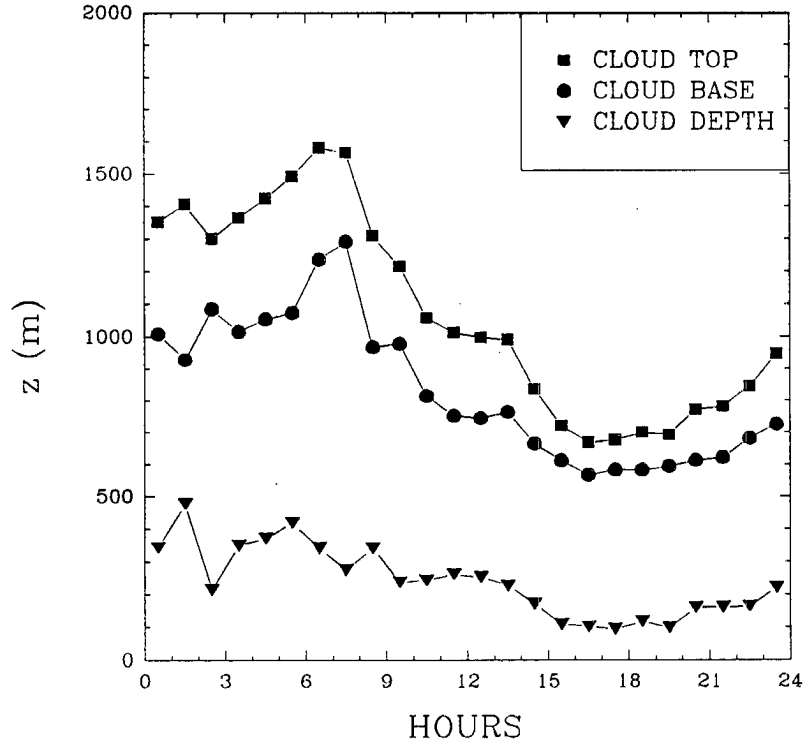
**Fig 6.3 NOAA/WPL 8.7 mm radar derived cloud top, base and depth for June 14, 1992**

Fig. 6.5 shows the variation the hourly averaged cloud aspect ratio on June 14, 1992. Also plotted is the effective cuboidal cloud aspect ratio determined from Eq. (4.3) using the measured values of $N_e$ and $N_a$. Note that the measured values of aspect ratio are significantly smaller than the values of $a_{cub}$, especially after 12 UTC when the aspect ratios become large. Even if all the measurement uncertainties were eliminated and the observed cloud aspect ratios were correct, discrepancies might still exist between the observed aspect ratios and the values of $a_{cub}$. Unlike the measured aspect ratios, $a_{cub}$ is dependent not only on the cloud shapes, but also on the spatial arrangement of the clouds in the cloud layer. Therefore, only if the clouds are distributed evenly in the cloud layer will the measured aspect ratio approach the derived value of $a_{cub}$.

## 6.4 Model Simulation of June 14, 1992

As hypothesized, the lack of a corresponding decrease of the LW CRSF with the absolute cloud fraction, $N_a$, during the afternoon of June 14, 1992 at ASTEX could be due to emission from the sides of the finite cloud elements in the cloud layer. To test this hypothesis the model described in Chapter 3 was run to generate broad-

60
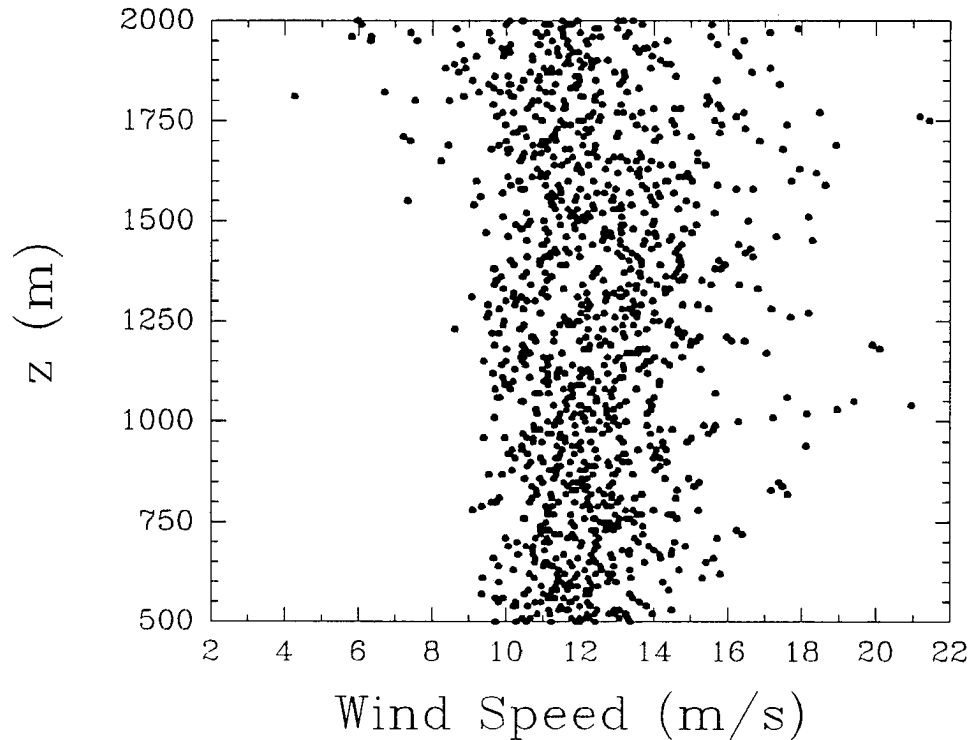
**Fig 6.4 Rawinsonde derived horizontal wind speeds for June 14, 1992**

band surface fluxes. The cloud layer position was specified by the radar determined cloud top and base and the PRT-6 derived absolute cloud fraction. The cloud elements were assumed to be blackbody cuboidal clouds with the temperature of their environment. The sounding used was a composite of all the ASTEX soundings.

Fig. 6.6 shows a comparison of the modelled and the measured LW CRSF. The model was run twice using both the PRT-6/radar measured cloud aspect ratios and the effective cuboidal aspect ratios calculated in section 6.3. In addition, the results for a planar cloud field are also plotted. This planar cloud forcing was determined by weighting the measured LW surface flux and the LOWTRAN modelled clear sky surface flux by the PRT-6 measured absolute cloud fraction, $N_a$. The curve for the planar cloud case can be construed as the LW CRSF predicted by any scheme that ignores finite cloud effects.

Comparison of the measured, modelled and planar curves in Fig. 6.6 shows good agreement between the hours of 0 and 6 UTC. This would be expected since $N_a$ was high during this period and finite cloud effects would therefore be minimal. The purpose of this modelling study was to show that the inclusion of finite cloud effects could account for the significant difference between the measured and planar LW CSRF. Looking at Fig. 6.6
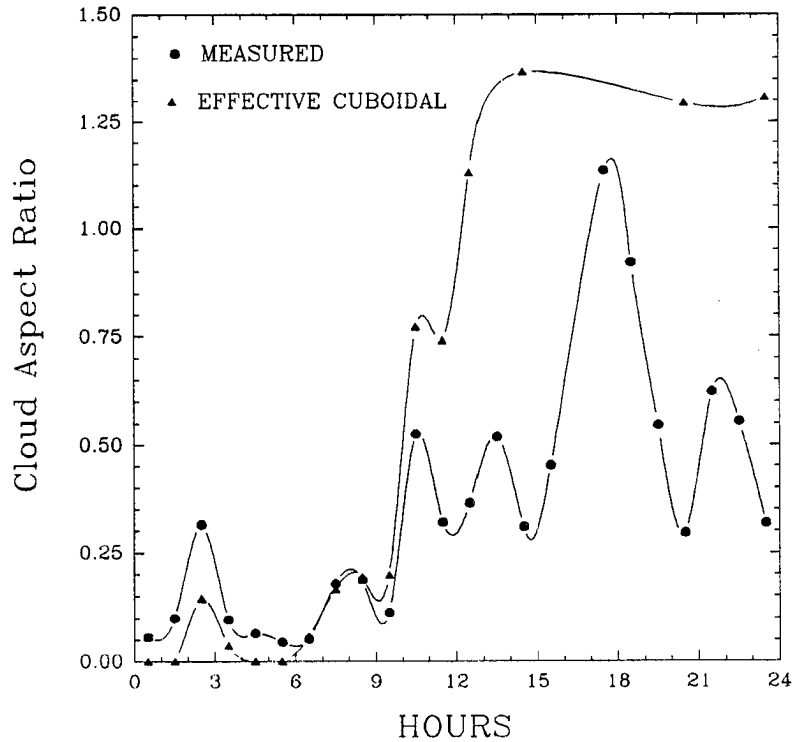
**Fig 6.5 Measured and effective cuboidal cloud aspect ratio for June 14, 1992**

during the period from 6 to 15 UTC shows that the inclusion of the lateral cloud emission does indeed account for the observed variation in LW CRSF. Much of the difference between the modelled and measured curves might be due to uncertainties in $N_a$. This can be clearly seen around 17 UTC where the measured $N_a$ goes to zero. For this case, the model assumed clear sky conditions and predicted zero LW CRSF but clearly some cloudiness existed and influenced the measured LW CRSF.

## 6.5 Summary

This chapter used the analysis techniques described in Chapter 5 to study in depth the role of finite cloud emission in the surface flux on June 14, 1992 at ASTEX. This day was chosen since the complicating factors of multilevel and cirrus cloud decks were absent. Cloud aspect ratios were measured with a vertically oriented narrow beam radiometer and 8mm radar data. The measured aspect ratios varied from 0 to near 1. The model described in Chapter 3 was utilized to show that finite cloud effects could reproduce the observed LW CRSF. Significant errors in the LW CRSF were observed when the finite cloud effects were ignored.
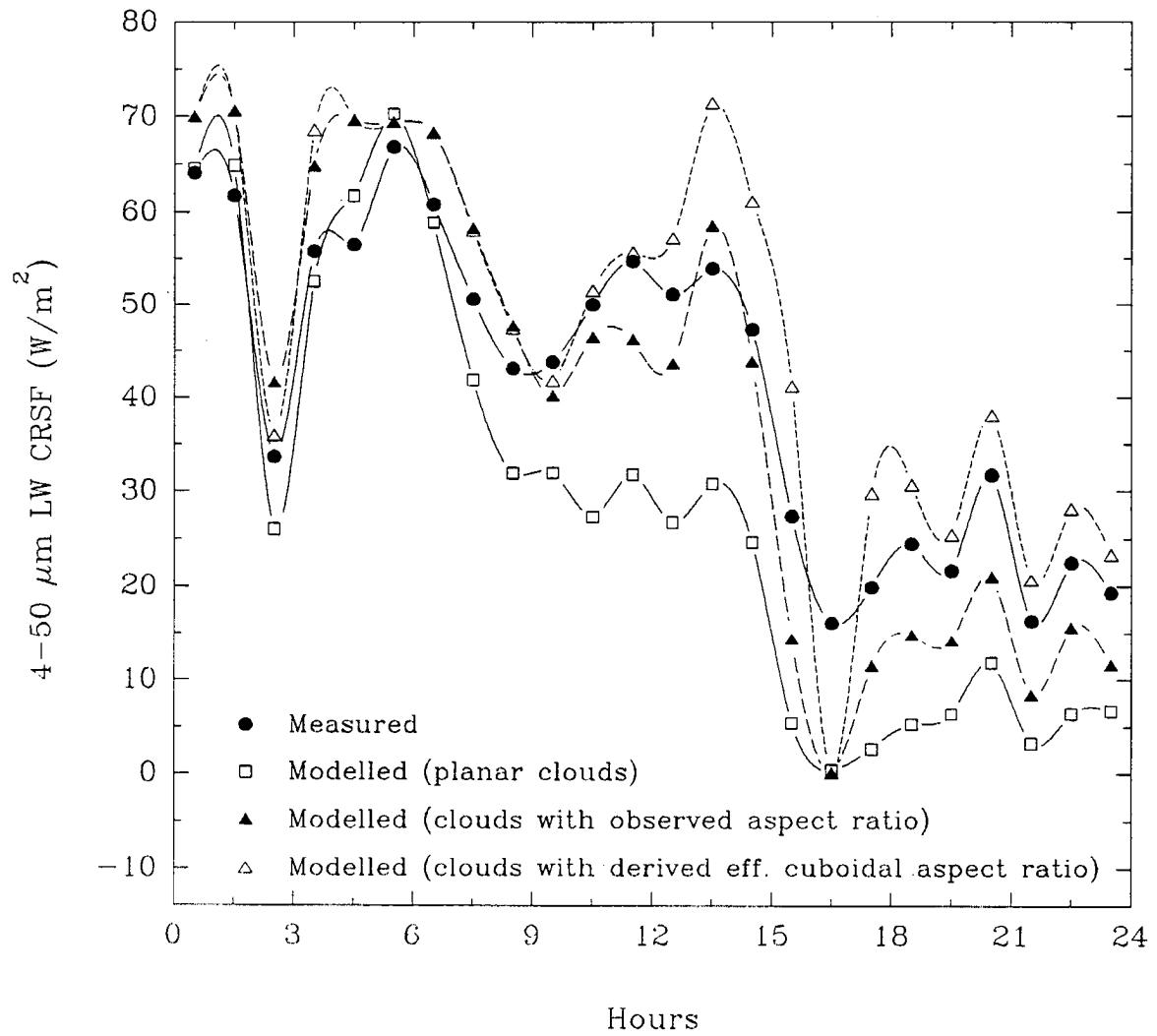
62

**Fig. 6.6 Comparison of measured and modelled results for ASTEX June 14, 1992**

# Chapter 7

## LONGWAVE HEATING RATES IN ISOLATED AND NON-ISOLATED CLOUDS

Though the three dimensional studies of Liou and Ou (1980) and Harshvardhan *et al.* (1981) have shown the dramatic difference between the longwave heating rates of isolated finite and plane-parallel clouds, the radiative effect of neighboring clouds was ignored. Some aspects of radiative transfer through an array of clouds were explored in Harshvardhan and Weinman (1982), but no results showing the heating rates in non-isolated finite clouds were presented. Since clouds can rarely be considered as radiatively isolated from other clouds, the effect of neighboring clouds on the distribution of heating in non-isolated clouds warrants further study. The goal of this chapter, therefore, is to explore the heating rate profiles in both isolated and non-isolated finite clouds.

To study the heating rates in isolated and non-isolated finite clouds, the three dimensional longwave radiative transfer model described in Chapter 3 was used. The simulated clouds were cubically shaped with each side being 1000 meters in length. The cloud liquid water content, LWC, was assumed to be 0.1 $g/m^3$ and to have no vertical variation. For the non-isolated simulations, the cloud was imbedded into a regular array of identical clouds with absolute cloud fractions of 0.25, 0.51 and 0.83 being simulated by cloud separations of 2000, 400, and 100 meters respectively. The clouds were assumed to be isothermal with temperatures of -10°C. In addition, the underlying surface was assumed to behave as a blackbody with a temperature of 15°C. Note that the values used for the cloud and surface temperatures, the cloud size and the cloud LWC were chosen to produce clouds similar to those modelled by Liou and Ou (1979) and Harshvardhan (1981).

Since longwave radiative transfer in clouds is dominated by liquid water, the effects of atmospheric water vapor are ignored in these calculations. Even though the results in this chapter are limited to the spectral region of 11 $\mu$m, Stephens (1978) showed that the heating rates in the 8-14 $\mu$m region dominate the total longwave heating for plane-parallel clouds. Since the 11 $\mu$m region is representative of the entire 8-14 $\mu$m window region, the results

presented in this chapter are therefore representative of the total longwave heating rates.

For three dimensional radiative transfer, the heating rate can be expressed as:

$$\frac{dT}{dt} = -\frac{1}{\rho C_p} \nabla \cdot F_{3D}^{net} \qquad (7.1)$$

where the gradient of the net flux is given by:

$$\nabla \cdot F_{3D}^{net} = \frac{d(F_x^+ - F_x^-)}{dx} + \frac{d(F_y^+ - F_y^-)}{dy} + \frac{d(F_z^+ - F_z^-)}{dz} \qquad (7.2)$$

The definitions of the fluxes $F_{x,y,z}^{+/-}$ are given in Section 3.3. For the model simulations presented in this chapter, the heating rates were calculated using a finite differentiation with a horizontal and vertical resolution of 50 meters. Values of 1 kg/m$^3$ and 1000 J/kg/K were assumed for the density, $\rho$, and the specific heat, $c_p$, of air respectively.

## 7.1 Comparison of the Vertical Heating Rates in Isolated and Non-isolated Cubic Clouds

The vertical heating can be calculated by ignoring the horizontal flux divergences in Eq. (7.1). The horizontally averaged vertical heating rates profiles for the cubic cloud simulations described above are shown in Fig. 7.1. Since the effects of atmospheric water vapor were ignored in these simulations, no radiative heating or cooling occurs outside of the cloud layer which spans from 1000 to 2000 meters. Therefore, only results from the cloud layer will be shown in this chapter. As the results show, the mean vertical heating profile for the isolated cubic cloud, the non-isolated clouds and the plane-parallel cloud are virtually indistinguishable. As Fig 7.1 shows, the isolated cloud exhibits slightly less vertical cooling at the cloud top and warming at the cloud base relative to the plane-parallel cloud. This behavior is due to the influence of the cloud edges, which vertically warm and cool much less than the cloud center. Since this effect is confined to the cloud edges, the horizontally averaged profiles show little difference. Careful analysis of Fig. 7.1 shows that the non-isolated cloud vertical heating rates varied between the isolated and plane-parallel values. As expected, of the three values of $N_a$ shown, the $N_a = 0.25$ non-isolated cloud mostly closely resembled the vertical heating rates in the isolated cloud and the $N_a = 0.83$ non-isolated

cloud most closely resembled the vertical heating rates in the plane-parallel cloud.
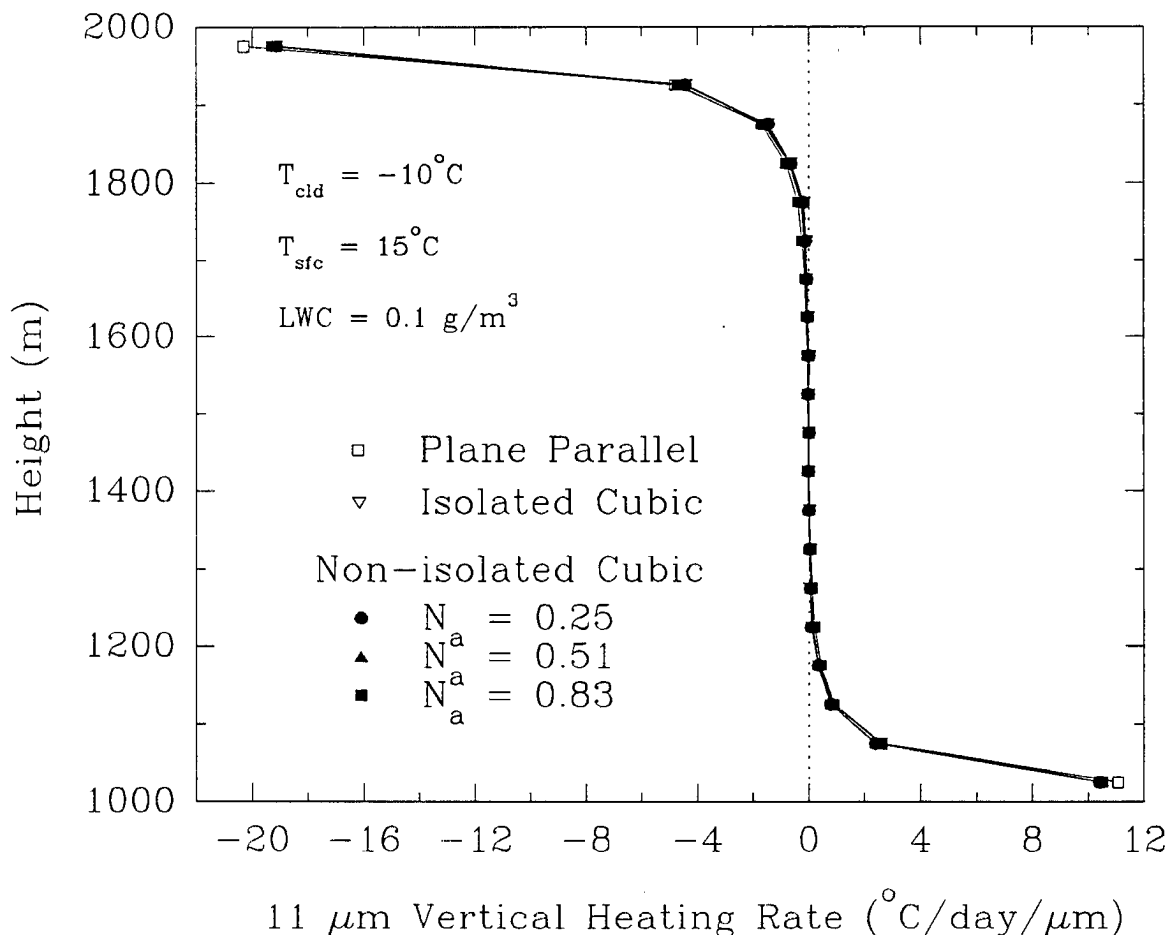


Fig. 7.1 The vertical heating rates for the simulated isolated, non-isolated and plane-parallel clouds.

## 7.2 Comparison of the Horizontal Heating Rates in Isolated and Non-isolated Cubic Clouds

The horizontally averaged horizontal heating rate profiles for the simulated isolated, non-isolated and plane-parallel clouds are shown in Fig 7.2. Due to the horizontal homogeneity in the plane-parallel cloud, the plane-parallel horizontal heating rate is zero throughout the cloud. Looking at the horizontal heating profile for the isolated cloud shows a maximum cooling near the cloud base and maximum warming near the cloud top. These results are qualitatively opposite to the results in Fig 7.1, where the vertical heating caused warming near the cloud base and cooling near the cloud top. This horizontal cooling near the isolated cloud's base can be explained using Fig 7.3, a schematic of a vertical cross section through the cloud. Imagine two points near the base of the cloud,
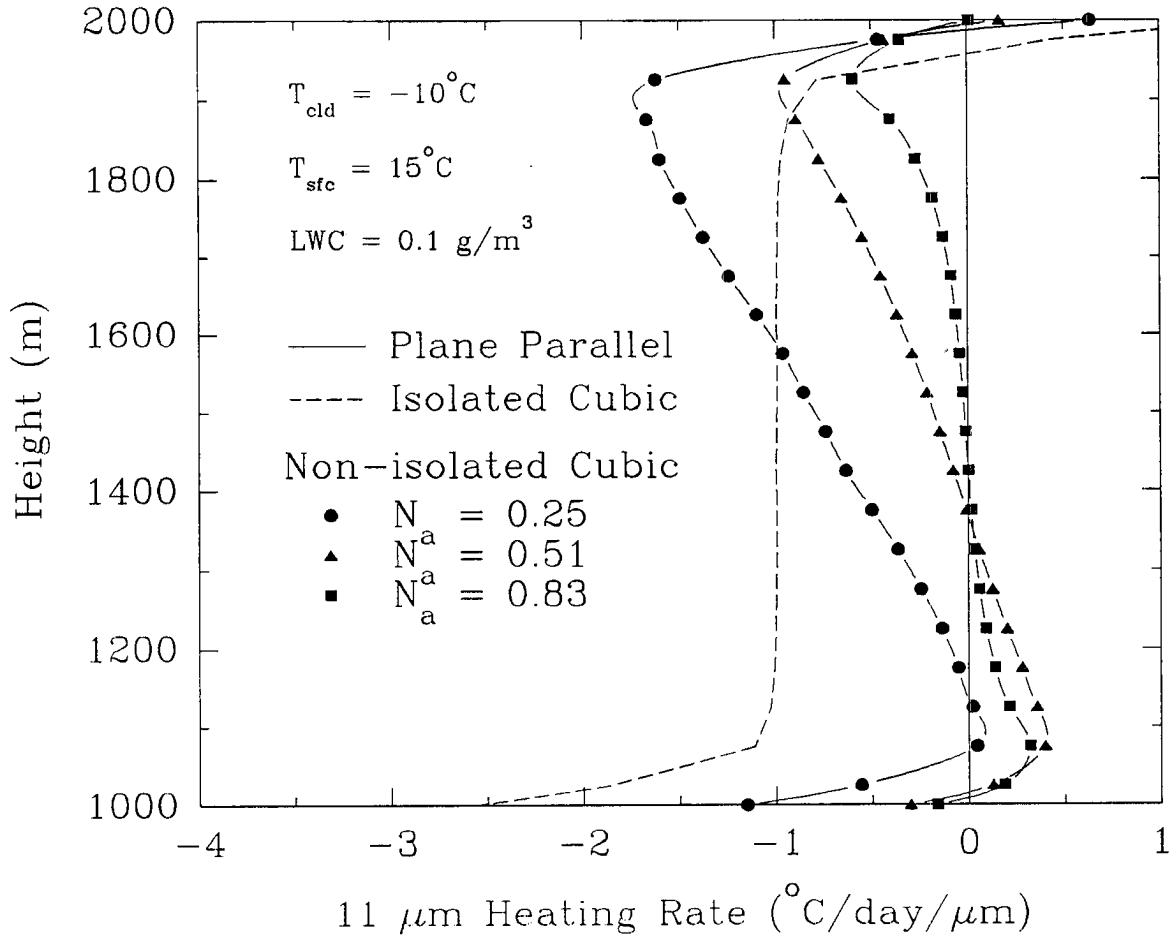
**Fig. 7.2** The horizontally averaged horizontal heating rate profiles for the simulated isolated, non-isolated and plane-parallel clouds.

$A_1$ and $A_2$, with $A_2$ being near the edge of the cloud and $A_1$ being more towards the center. Since both $A_1$ and $A_2$ see the same amount of cloud and the underlying surface in the -x direction, the values of $F_x^+$ at $A_1$ and $A_2$ will be identical. Looking in the +x direction however, $A_2$ sees no cloud while $A_1$ does. Therefore, $F_x^{net}$ will increase from $A_1$ to $A_2$ and a horizontal cooling will result. Similarly, the values of $F_x^{net}$ at $C_1$ and $C_2$ can explain the horizontal cloud top warming in the isolated cloud. Since $C_2$ is able to see the underlying surface while $C_1$ sees only cloud and the clear sky, $F_x^{net}$ will decrease from $C_1$ to $C_2$ and a horizontal warming will occur. The horizontal cooling in the center of the cloud can be explained by the net flux at $B_2$ being greater than the net flux at $B_1$. This cooling however, is dependent on the difference in temperature between the cloud and the ground. If the surface were warm enough so that its emission was more than twice that of the cloud's emission, a horizontal warming

would occur in the center of the cloud. For this simulation, the temperature of the underlying surface would have

to be greater than 32°C to cause a horizontal warming in the center of cloud, which had a temperature of -10°C.
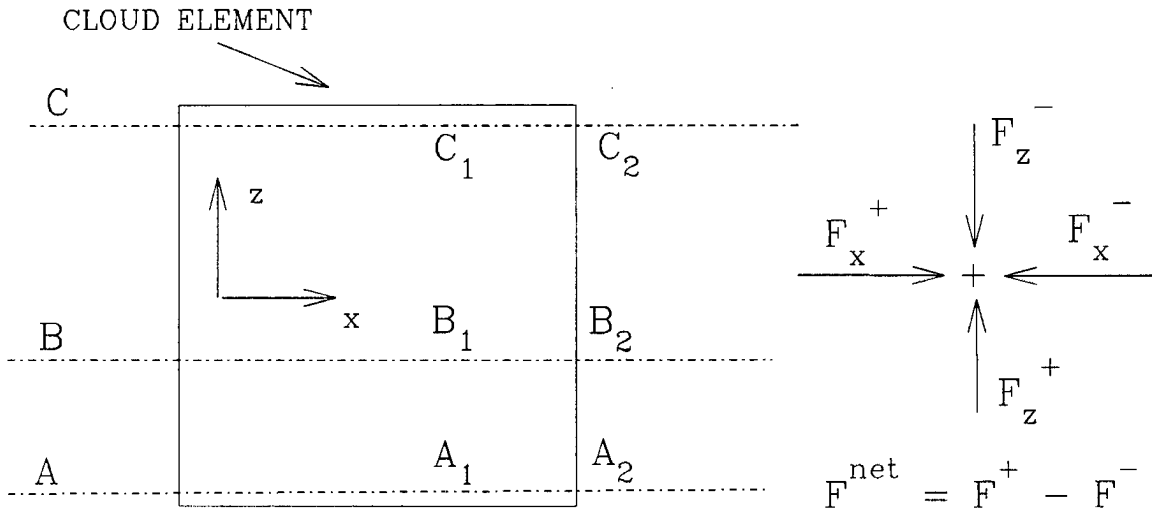


Fig 7.3 Schematic of a vertical cross section through the center of a cubic cloud.

As shown in Fig 7.2, relative to the isolated cloud, the non-isolated clouds exhibited less cloud base

horizontal cooling and cloud top horizontal warming. Once again, these behaviors can be conceptually explained

through Fig. 7.3. Due to the presence of the neighboring clouds, the gradient of the horizontal net flux between

$A_1$ and $A_2$ for the non-isolated clouds will still be positive but less positive than the isolated cloud. Therefore less

horizontal cooling will occur along the edges of non-isolated cloud base than in the isolated cloud. Similarly, the

neighboring clouds will act to block surface emission from point $C_2$ and cause the gradient of the horizontal net flux

along $C_1$ and $C_2$ to be in the same direction but of less magnitude than the isolated cloud. Consequently, the cloud

top heating on the edges of non-isolated clouds is less than that in isolated clouds. In these two instances, the cloud

base warming and cloud top cooling, the non-isolated cloud results fall between the isolated and plane-parallel

results.

As Fig 7.2 shows, the horizontal heating rates of the non-isolated clouds are not always bounded by those

in the isolated and plane-parallel clouds. For example, in the $N_a$ = 0.51 and 0.80 simulations, the presence of

neighboring clouds caused a significant horizontal warming near the cloud base (1200 meters). In addition, the

presence of neighboring clouds in the $N_a$ = 0.25 and 0.51 simulations caused a significantly greater horizontal

cooling near the cloud top than in the isolated cloud. This behavior can be explained by imagining the fluxes at points $B_1$ and $B_2$ in Fig. 7.3. At point $B_1$, the net horizontal flux in the isolated and non-isolated cloud will be identical. For this simulation, the net horizontal flux at $B_2$ in the isolated cloud is greater than that at $B_1$. In the non-isolated cloud, if $B_2$ gains more emission from the surface than it losses to the clear sky, a horizontal warming will occur between $B_1$ and $B_2$. If the neighboring clouds shield enough of the surface from $B_2$, $B_2$ will lose more energy to the clear sky than it gains from the surface below and a horizontal cooling will occur between $B_1$ and $B_2$. Therefore, near the cloud base where $B_2$ sees more of the surface than the clear sky, the non-isolated clouds experience a horizontal warming and near the cloud top, where $B_2$ sees more of the clear sky, the non-isolated clouds experience a horizontal cooling. This cooling near the cloud top and warming near the cloud base is maximum for the $N_a = 0.51$ simulation. Significant warming near the cloud base and cooling near the cloud top also occurs for the $N_a = 0.83$ and the $N_a = 0.25$ simulations respectively.

## 7.3 Comparison of the Total Heating Rates in Isolated and Non-isolated Clouds

The horizontally averaged total heating rate profiles shown in Fig. 7.4, are simply the sum of the profiles shown in Figs. 7.1 and 7.2. In agreement with Harshvardhan and Weinman (1981) and Liou and Ou (1980), the total cooling of the isolated cloud is always greater than that of the plane-parallel cloud. Throughout most of the cloud's depth, the isolated cubic cloud cools approximately 1°C/day more than the plane-parallel cloud with the difference being as large as 2°C/day near the cloud base and cloud top. As mentioned in Section 7.2, this increase in cooling in the isolated cloud is due primarily to the horizontal cooling near the cloud's edges.

This cooling along the edges of the cloud may feedback into dynamical and microphysical processes occurring in the cloud. For example, parcels of air along the cloud edges that cool, will sink and as they sink, they will continue to cool. If this sinking is strong enough to cause or to enhance convergence below the cloud, the cooling along the cloud edges may act to perpetuate the existence or growth of the cloud. In Roach (1976), radiative cooling was shown to enhance cloud droplet growth even in the slightly subsaturated environments typically found near the edges of clouds. This is a positive feedback since radiative cooling will increase with increasing cloud droplet size. This increase in cooling due to cloud droplet growth is due to the conversion of water vapor,

which is relatively transparent in the 8-14 $\mu$m atmospheric window, to the more opaque liquid water. Therefore, the enhancement of the longwave radiative cooling along isolated cloud sides would tend to increase cloud droplet sizes compared to the center of the cloud which is in approximate radiative equilibrium. Both of these longwave radiative feedbacks will be modulated by the absorption of shortwave radiation. Since the magnitude of the longwave heating rates are typically larger than the shortwave heating rates in clouds, the effect of shortwave absorption would be not to negate the feedbacks but to lessen them in the regions where shortwave absorption is occurring.
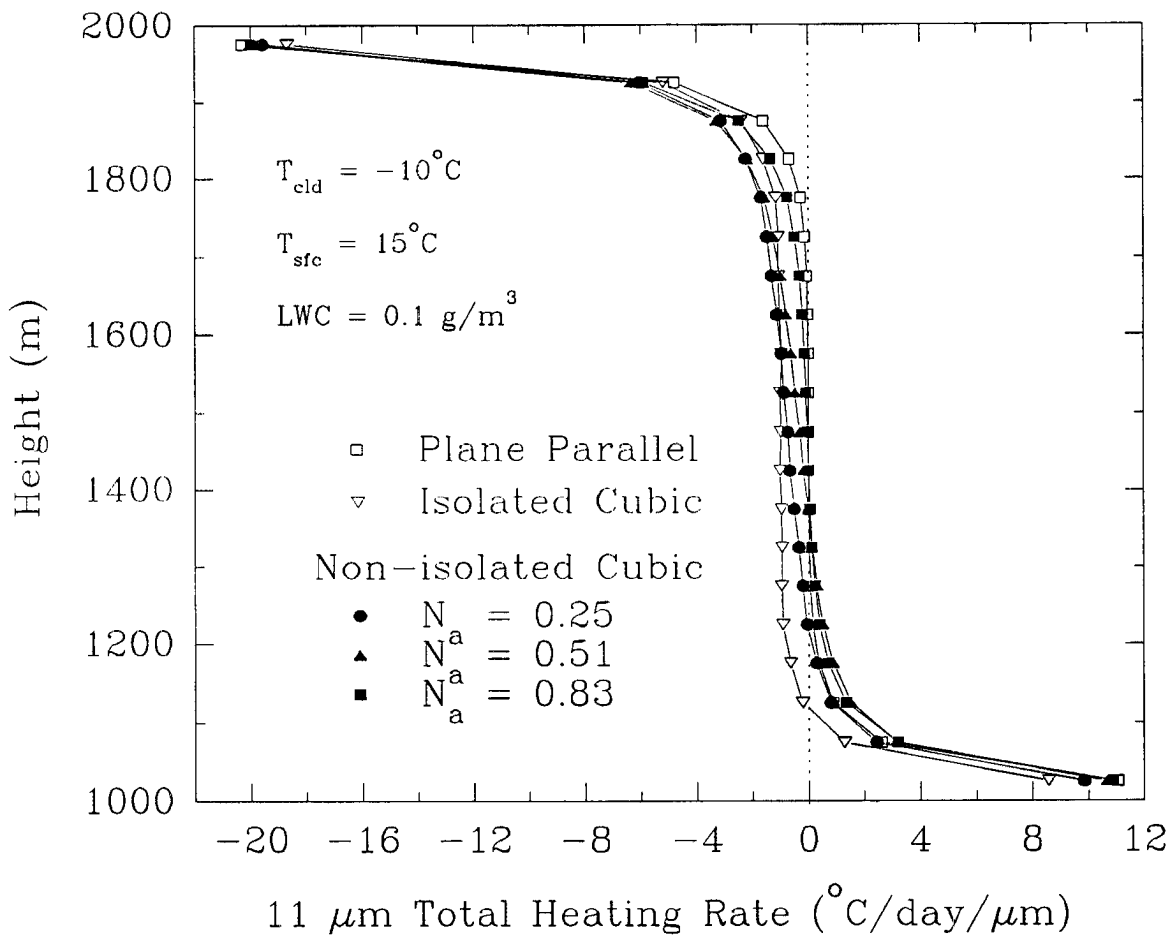


Fig. 7.4. The horizontally averaged total heating rate profiles for the simulated isolated, non-isolated and plane-parallel clouds.

The total heating rate profiles for the non-isolated clouds are also presented in Fig. 7.4. As in the horizontal heating rate profiles, regions exist near the cloud base and cloud top where the non-isolated total heating

rates do not fall between the isolated and plane-parallel values. For example, 200 meters above the cloud base, the isolated cloud is experiencing a significant cooling while the non-isolated clouds, with $N_a = 0.51$ and $0.83$, are experiencing a warming which is significantly larger than the plane-parallel cloud warming. In addition, the non-isolated clouds with $N_a = 0.25$ and $0.51$ experience a cooling rate, 200 meters below the cloud top, which is greater than both the isolated and plane-parallel cooling rates.

Since the total heating rates in the non-isolated cloud simulations do not fall between the isolated and plane-parallel values, the dynamical feedback discussed above will not be diminished when considering non-isolated clouds, but will be fundamentally different. For example, consider Figs. 7.5 and 7.6 which show the total heating rates along one side of an isolated and a non-isolated, $N_a = 0.51$, cloud respectively. As Figs. 7.5 and 7.6 show, both the isolated and non-isolated cloud sides experience a maximum cooling near the cloud top. While the isolated cloud side experiences cooling over its entire surface, the non-isolated cloud side experiences warming along the lower 350 meters of the cloud side, with a maximum warming occurring near the cloud base.

Unlike the isolated cloud, however, the distribution of heating along the non-isolated cloud side would tend to cause air parcels either to rise or to sink depending on the location of the parcel on the cloud side. In addition, this distribution of heating along the non-isolated cloud sides will encourage cloud droplet growth in the upper sections of the cloud which are cooling and discourage droplet growth along the lower sections of cloud sides which are warming.

Note that these simulated differences between the heating rates in isolated and non-isolated clouds are limited to the transparent 8 - 14 $\mu$m window region. Due to the opacity of a moist atmosphere to longwave radiation outside of the 8-14 $\mu$m window region, little cooling would occur in both isolated and non-isolated clouds outside of the atmospheric window. Therefore, the differences in the isolated and non-isolated cloud heating profiles from these 11 $\mu$m simulations, which neglected atmospheric water vapor, are larger than what would be expected if a realistic treatment of atmospheric water vapor were included. Due to the transparency to water vapor of the 8-14 $\mu$m window region, however, the inclusion of atmospheric water vapor should not qualitatively alter the results of the simulations presented here.

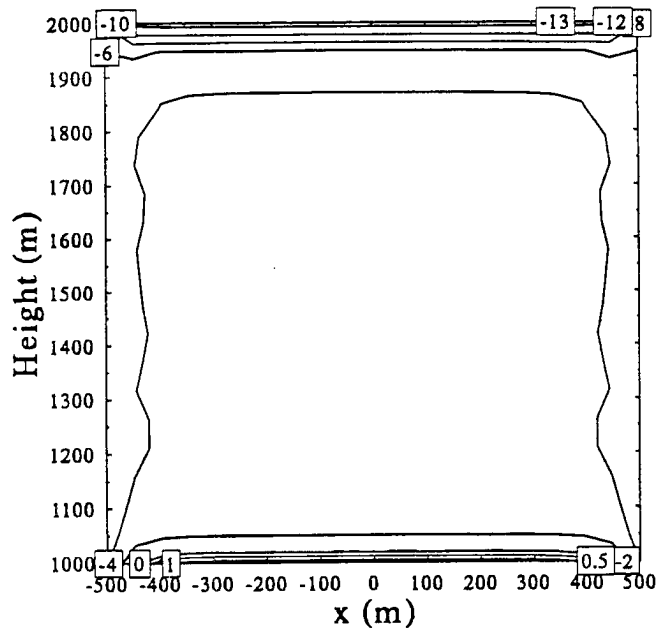Fig. 7.5 The total 11 $\mu$m heating rates (°C/day/$\mu$m) along one lateral side of an isolated cubic cloud.
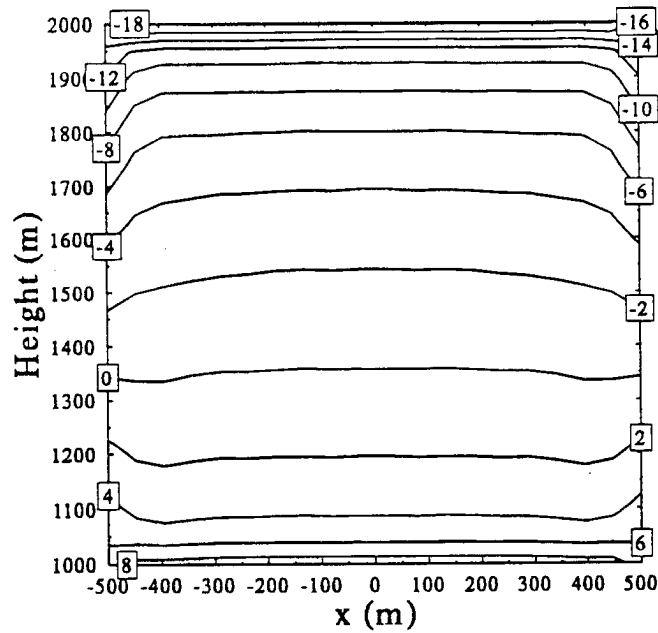


Fig. 7.6 The total 11 $\mu$m heating rates (°C/day/$\mu$m) along one lateral side of a non-isolated ($N_a=0.51$) cubic cloud.

### 7.3.1 The Sensitivity to Cloud Spacing

The sensitivity of the mean total 11 $\mu$m heating rate in non-isolated clouds to the distance between the clouds is shown in Fig. 7.7. In this figure, the results are shown as the ratio of the mean total 11 $\mu$m heating rate of the cloud , $H_{mean}$, to the heating rate predicted by plane-parallel theory, $H_{mean,pp}$. Results for clouds with aspect ratios of 0.5 and 1.0 are shown. The ratios of these values for the non-isolated clouds ranged from 1.0, the plane-parallel value to the value for an isolated cloud which was 1.6 and 2.3 for the clouds with aspect ratios of 0.5 and 1.0 respectively. This isolated cloud values of the ratio of the total heating in an isolated to a plane-parallel cloud were found to be nearly independent of the assumed cloud and underlying surface temperatures. As this figure shows, for cloud layers consisting of clouds with aspect ratios near 1.0, the neighboring clouds have a significant influence on the total heating rates of non-isolated clouds if the clouds are spaced less than 2 cloud widths apart. For cloud layers consisting of clouds with aspect ratios near 0.5, the total cooling of the clouds approaches the isolated cloud value when the clouds are spaced only one half cloud width apart. The simulations used in Fig. 7.7 are identical to simulations described above. In addition, Fig 7.7 shows that plane-parallel theory does not accurately predict the total 11 $\mu$m heating in finite clouds until the separation distance between clouds approaches 10% of the mean cloud width.


### 7.4 Summary

This chapter explored the heating rates in simulated isolated and non-isolated cubic clouds. The non-isolated clouds consisted of cubic clouds imbedded into regular arrays of cubic clouds with differing values of $N_a$. The results showed that the heating rate profiles of non-isolated clouds do not always fall between the heating rate profiles of isolated and plane-parallel clouds. Results were shown that indicate that the dynamical and microphysical effects of the longwave heating in isolated and non-isolated clouds are significantly different. Neighboring clouds were shown to have a significant effect on the heating rates of non-isolated clouds when the clouds were separated by less than twice the mean cloud width.
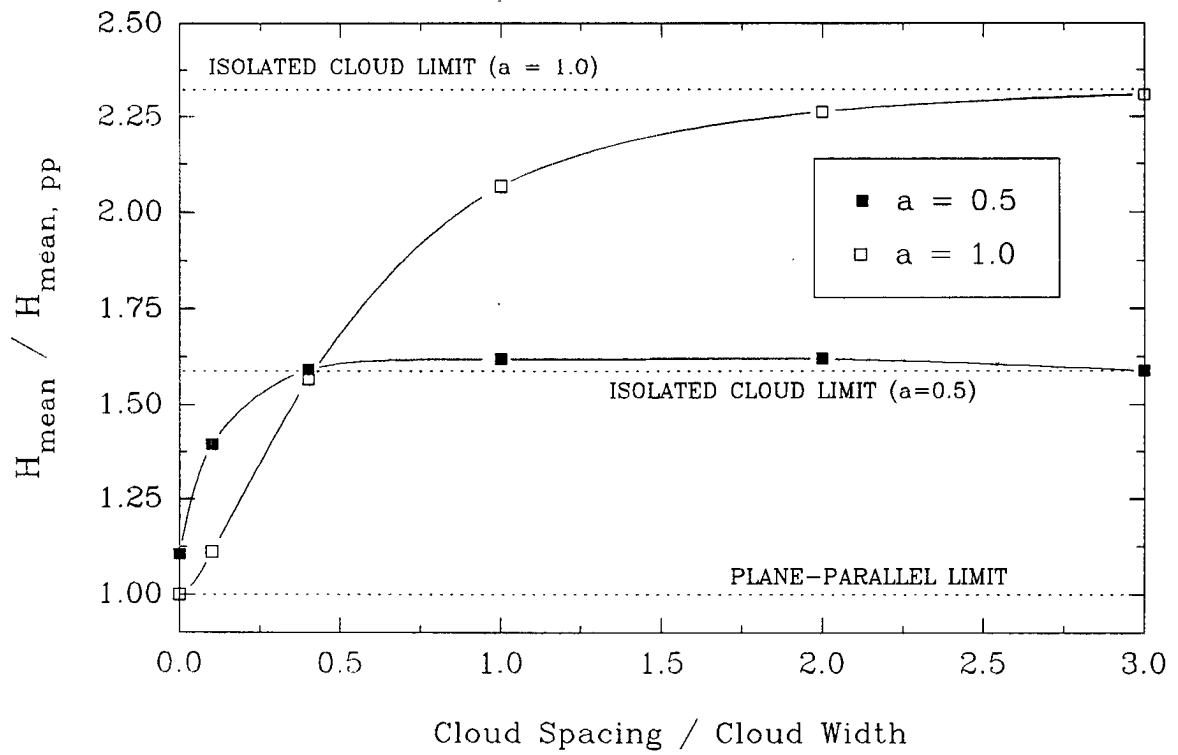
**Fig. 7.7** The sensitivity in the mean total 11 $\mu$m heating rate in non-isolated clouds to the amount of separation between clouds.

# Chapter 8

## THE INCLUSION OF THREE DIMENSIONAL FINITE CLOUD EFFECTS IN ONE DIMENSIONAL LONGWAVE RADIATIVE TRANSFER SCHEMES

In the previous chapters, observations and three dimensional modelling studies have shown that finite cloud effects can significantly alter longwave radiative transfer. This sensitivity of longwave radiative transfer to finite cloud effects is large enough to warrant the inclusion of these effects into numerical weather and climate prediction models. Due to the computational requirements of three dimensional (3D) radiative transfer schemes, the inclusion of finite cloud effects into numerical weather and climate prediction models requires that these effects be incorporated into the existing computationally efficient one dimensional (1D) radiative transfer schemes. This chapter will compare several techniques which allow 1D radiative transfer schemes to account for 3D finite cloud effects.

Since the radiative quantity most useful to numerical weather and climate models is the radiative heating rate, the various methods, discussed below, will be judged on their ability to reproduce the mean heating calculated by the fully 3D radiative transfer model developed in Chapter 3. The longwave heating rate, H(z), can be expressed in terms of the vertical divergence of the net flux, $F_{net}(z)$, as:

$$H(z) \ = \ = -\frac{1}{\rho c_p} \frac{\partial F_{net}}{\partial z} \tag{8.1}$$

where $F^{net}(z)$ is expressed as :

$$F^{net}(z) \ = \ F^+(z) \ - \ F^-(z) \tag{8.2}$$

The superscripts "+" and "-" refer to the upwelling and downwelling fluxes respectively. Note that the horizontal flux divergence was ignored in the calculation of these heating rates. Since the quantities in this chapter are obtained by horizontally averaging through a cloud layer that extends infinitely, the horizontally averaged horizontal

net flux and horizontal flux divergence is zero. This would not be the case for an isolated cloud, as shown in Chapter 7, where the horizontal flux divergence does play a large role in the overall heating of the clouds.

## 8.1 One Dimensional Finite Cloud Methods

Four methods were chosen as candidates for the inclusion of three dimensional finite cloud effects into one dimensional longwave radiative transfer codes. Only methods that could be relatively easily implemented into existing 1D radiative transfer schemes were examined. These four finite cloud methods are listed below.

1) A weighting scheme based on $N_a$.

2) A weighting scheme based on $N_e$.

3) A scheme based on the effective emissivity.

4) A scheme based on a linear variation of $N_c^{+/-}$ in the cloud layer.

The remainder of this section will explain each method in detail.

### 8.1.1 Weighting Schemes Based on $N_a$

Traditionally, radiative transfer in the presence of partial cloudiness conditions has been solved by weighting the radiative transfer solutions for clear and overcast sky conditions (Stephens 1984). The most common weight used in this method is the absolute cloud fraction, $N_a$. As discussed in Chapter 4, $N_a$ is the cloud fraction that accounts only for the horizontal extent of the clouds. It is this absolute cloud fraction that is currently predicted in numerical models and most often measured by satellites.

The use of $N_a$ as the weighting factor allows the upwelling, $F^+$, and downwelling, $F^-$, fluxes in the presence of partial cloudiness to be written as:

$$F^+(z) = N_a F_{ovc}^+(z) + (1-N_a) F_{clr}^+(z) \qquad (8.3)$$

$$F^-(z) = N_a F_{ovc}^-(z) + (1-N_a) F_{clr}^-(z) \qquad (8.4)$$

where the first terms on the right hand sides of Eqs. (8.3) and (8.4) represent the cloudy sky contribution and the second terms represent the clear sky contribution to the fluxes. The subscripts "clr" and "ovc" refer to the values

under clear and overcast sky respectively. Using the above expressions for the upwelling and downwelling fluxes the net flux in the presence of partial cloudiness using this weighting scheme can be expressed as:

$$F^{net}(z) = F^+(z) - F^-(z) = N_a F^{net}_{ovc}(z) + (1-N_a) F^{net}_{clr}(z) \qquad (8.5)$$

Since $N_a$ is not a function of position, the mean heating rate profile, H(z), using a weighting scheme based on $N_a$, is simply calculated by weighting the overcast, $H_{ovc}(z)$, and clear sky, $H_{clr}(z)$ heating rates and can be written as:

$$H(z) = N_a H_{ovc}(z) + (1-N_a) H_{clr}(z) \qquad (8.6)$$

where $H_{clr}(z)$ and $H_{ovc}(z)$ are calculated by using the appropriate values in Eq. (8.1).

### 8.1.2 Weighting Schemes Based on $N_e$

As mentioned, the use of weighting scheme based on $N_a$ ignores the radiative effect of the vertical dimensions of the clouds. One obvious way to incorporate the effect of the cloud 3D finite dimensions would be to replace $N_a$ in the above weighting scheme with the $N_e$, the effective cloud fraction. Using such a scheme, the mean heating rate profile for a partially cloudy atmosphere would now be expressed as:

$$H(z) = N_e H_{ovc}(z) + (1-N_e) H_{clr}(z) \qquad (8.7)$$

In Chapter 4, the inclusion of atmospheric effects introduced a slight altitude dependence on $N_e$ and $N_e$ was shown to have a large directional dependence inside the cloud layer. The $N_e$ value used in this weighting scheme was assumed to be the quasi-constant value occurring outside of the cloud layer and to have no vertical variation. In this method, the directional dependence of $N_e$ is ignored.

### 8.1.3 The Use of an Effective Emissivity

Unlike the two previous methods for the inclusion of 3D finite cloud effects in 1D longwave radiative schemes, the use of an effective emissivity does not involve the weighting of clear and overcast sky values. This

method allows the mean heating rate profile to be calculated using a 1D longwave radiative scheme where the partially cloudy layer is replaced by a homogeneous layer with the desired effective emissivity, $\epsilon_e$. Unlike the other 1D finite cloud methods discussed in this chapter which weigh overcast and clear sky flux profiles, only one net flux profile would have to be calculated for the effective emissivity method.

The term effective emissivity used in this study actually refers to the downwelling effective emissivity defined by (Cox, 1969) as:

$$\epsilon_e = \frac{F_b^- - F_t^-}{B(T_b) - F_t^-} \qquad (8.8)$$

where $F_b^-$ and $F_t^-$ are the mean downwelling fluxes at the cloud base and top respectively and $B(T_b)$ is the Planckian emission at the cloud base temperature, $T_b$. The directional dependence on $\epsilon_e$ is assumed negligible in this study which is appropriate for optically thick boundary layer clouds.

The above definition of the effective emissivity can compared to the expression for $N_e$ given in Eq. (4.1). Rewriting the definition for $N_e$ in a form similar to the definition of $\epsilon_e$ gives:

$$N_e = \frac{F^- - F_{clr}^-}{F_{ovc}^- - F_{clr}^-} = \frac{[F_b^- T_{sc} + F_{sc}^-] - [(F_t^- T_{cld,clr} + F_{cld,clr}^-) T_{sc} + F_{sc}^-]}{[F_{b,ovc}^- T_{sc} + F_{sc}^-] - [(F_t^- T_{cld,clr} + F_{cld,clr}^-) T_{sc} + F_{sc}^-]} \qquad (8.9)$$

where $F_{sc}$ and $F_{cld,clr}$ are the downwelling clear sky emissions from the sub-cloud layer and the cloud layer respectively. Similarly, $T_{sc}$ and $T_{cld,clr}$ represent the clear sky transmissions from the sub-cloud and cloud layer respectively. If the clouds are optically thick, then $F_b^-$ can be assumed to be $B(T_b)$ and the expression for $N_e$ can be simplified to :

$$N_e = \frac{F_b^- - F_{b,clr}^-}{B(T_b) - F_{b,clr}^-} \qquad (8.10)$$

where $F_{b,clr}^-$ is the downwelling clear sky flux at the cloud base altitude.

The similarity of Eqs. (8.10) and (8.8) would predict a corresponding similarity between the values of $N_e$

and $\epsilon_e$. As shown by Fig 8.1, the values of $N_e$ and $\epsilon_e$ are in relative agreement except for cases with low values of $N_a$ when the difference between $F_{b,clr}^-$ and $F_t^-$ is no longer negligible compared to $F_b^-$. Fig 8.1 was produced using the 3D model developed in Chapter 3 with a simulated cloud field consisting of cubic clouds with horizontal dimensions of 500 meters. A detailed description of this cloud field simulation is provided in Section 8.2
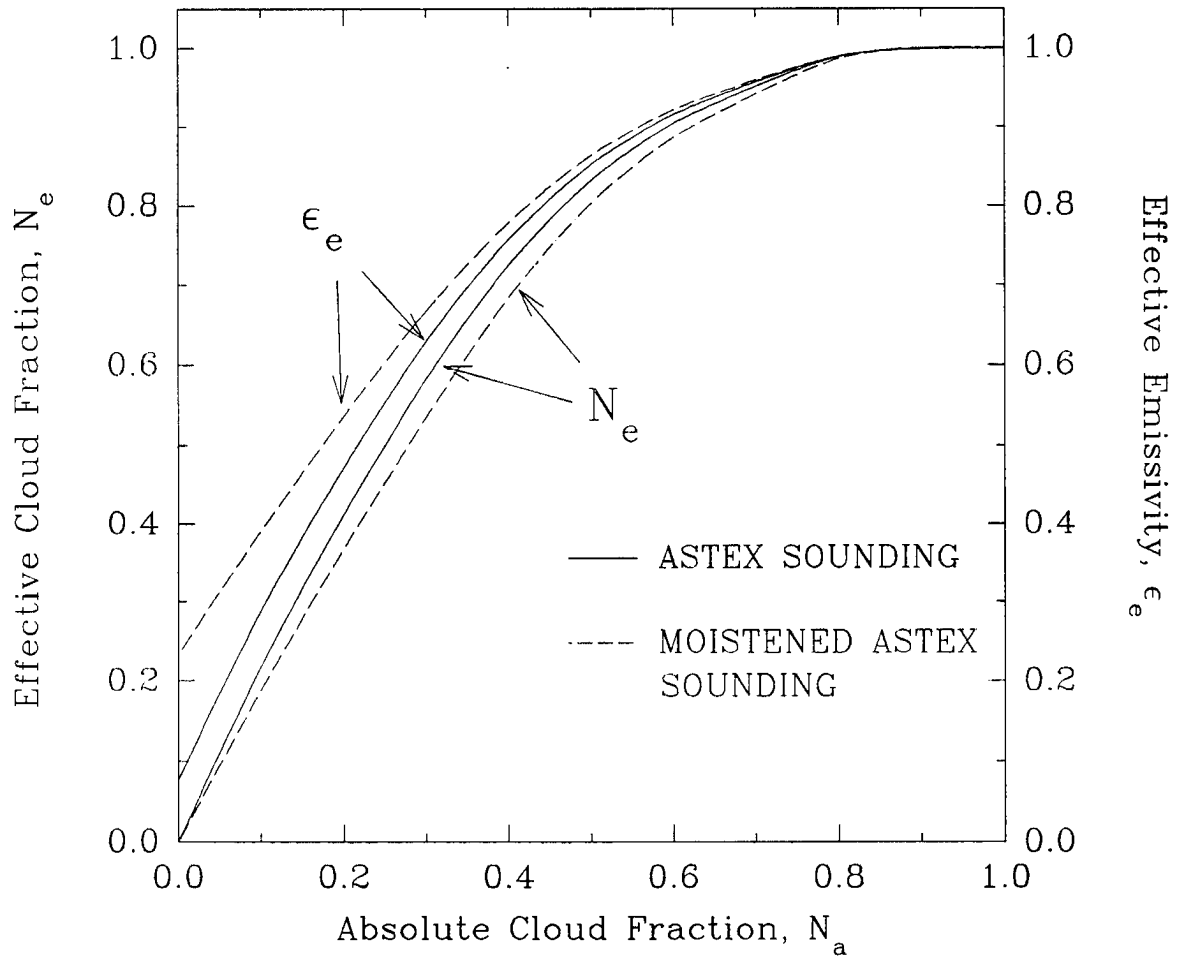


**Fig. 8.1 The Variation of $N_e$ and $\epsilon_e$ for cubic clouds in differing atmospheres.**

To study the effect of the atmosphere on the relationship between $N_e$ and $\epsilon_e$, Fig. 8.1 shows results obtained using the standard composite ASTEX sounding and a moistened composite ASTEX sounding. As described in Chapter 4, the moistened sounding is identical to the original except that the water vapor content has been doubled throughout the entire atmosphere. As Fig. 8.1 shows, the addition of more water vapor acted to increase the difference between $N_e$ and $\epsilon_e$ and this difference increased as $N_a$ decreased. The decrease in $N_e$ with the addition

79

of more water vapor is due to the sub-cloud buffering effect discussed in Chapter 3 while the increase in $\epsilon_c$ is due directly to the increase of the flux down at the cloud base. Unlike $N_e$, $\epsilon_c$ does not become zero as $N_a$ goes to zero. At a cloud fraction of zero, $\epsilon_c$ represents the emissivity of the ambient water vapor in the cloud layer.

## 8.1.4 Weighting Schemes Based on a Linear Variation of $N_e^{+/-}$ in the Cloud Layer

As discussed in Chapter 4, $N_e$ is relatively constant outside of the cloud layer. Inside of the cloud layer however, $N_e$ takes on a strong directional dependence as shown by the profiles of $N_e^+$ and $N_e^-$ in Fig. 4.7. Remember that $N_e^+$ is used to weight the upwelling fluxes while $N_e^-$ is used to weight the downwelling fluxes. This directional dependence is due to the aspect ratio of the cloud elements above and below the observer being dependent on the depth of the observer in the cloud layer. For example, at the base of a cloud layer, $N_e^-$ will have the value of the effective cloud fraction calculated outside of the cloud layer, $N_e$. As the observer approaches the cloud top from below, the relative aspect ratio of the cloud elements becomes smaller and smaller. For small aspect ratios, the effective and absolute cloud fractions become equal so that the value of $N_e^-$ near the top of the cloud should approach the value of $N_a$. The same reasoning applies to the variation of $N_e^+$ through the cloud layer.

One method to account for the variation of $N_e^{+/-}$ through the cloud layer is to assume that each value simply varies linearly between $N_e$ and $N_a$ throughout the depth of the cloud layer. This linear variation of $N_e^{+/-}$ through the cloud layer together with the assumption of a height independent $N_e$ outside of the cloud would produce a profile of $N_e$ as shown in Fig 8.2.

Using an $N_e^{+/-}$ profile similar to Fig 8.2, the calculation of the net flux, $F_{net}(z)$ and heating rate, $H(z)$, profiles outside of the cloud layer is identical to that using the weighting scheme based on a constant $N_e$, discussed in section 8.1.2. Inside the cloud layer, the upwelling and downwelling fluxes using this scheme can be expressed as:

$$F^+(z) = N_e^+(z) F_{ovc}^+(z) + (1 - N_e^-(z)) F_{clr}^+(z) \qquad (8.11)$$

$$F^-(z) = N_e^-(z) F_{ovc}^-(z) + (1 - N_e^-(z)) F_{clr}^-(z) \qquad (8.12)$$

Due to the variation of $N_e^{+/-}$ in the cloud layer, the net flux and heating rate profiles can not be calculated by simply

weighting the overcast and clear sky heating profiles as was done in sections 8.1.2 and 8.1.3. The heating rates

inside the cloud layer using this scheme must be calculated by a finite differentiation of the net flux profile.
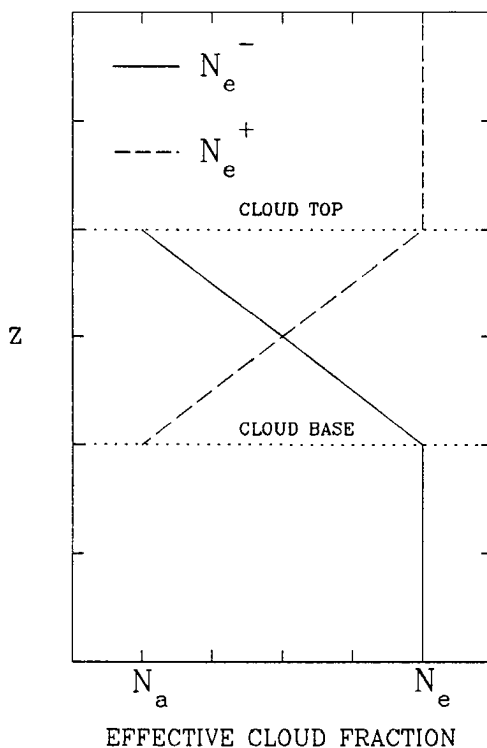


Fig. 8.2 The assumed variation of $N_e^{+/-}$ used in the linear $N_e^{+/-}$ 1D finite cloud method.


## 8.2 A Comparison of the Longwave Heating Rate Profiles Produced by the Different Methods

Since the model developed in Chapter 3 included the effects of the three dimensional variation in the cloud

geometry and radiance fields, its results were used as the basis for the comparison of the different methods for the

implementation of finite cloud effects into 1D radiative transfer codes. In the following figures, the results from

this model are labelled "3D" to distinguish them from the results produced by the methods outlined in section 8.1.

Unlike Chapter 7, where heating rates were calculated only in an individual cloud, the heating rates presented here

are horizontally averaged over the entire cloud layer.

The simulated cloud field consisted of cubic cloud elements with horizontal widths of 500 meters. As Fig.

8.3 shows, this cloud geometry is representative of fair weather cumuli. Differing absolute cloud fractions where

obtained by manipulating the spacing between the cloud elements. The cloud layer was situated between 1000 and
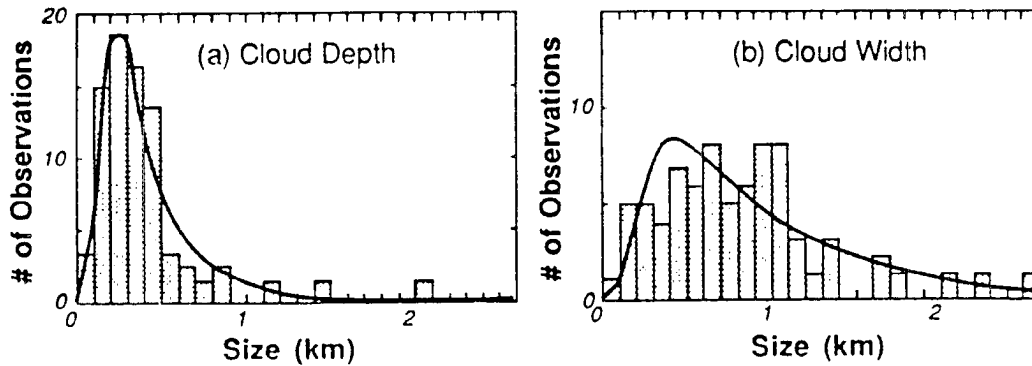
**Fig. 8.3** Histograms of (a) cloud depth and (b) cloud width, as measured from an airborne forward-looking automatic camera system for a total of 78 fair weather cumulus. (taken from Stull, 1984)

1500 meters above the surface. The liquid water content of the clouds was 0.2 $g/m^3$ and was vertically uniform. A temperature of 280 K was assumed for the clouds and the underlying surface was assumed to behave as a blackbody with temperature of 290 K. The effects of atmospheric water vapor were ignored. The neglecting of atmospheric water vapor is reasonable since the heating rate profile is dominated by the heating in the cloud layer, where liquid water is the dominant radiative species. All results in this section were calculated for the 11 $\mu$m spectral region.

### 8.2.1 The Cloud Layer

This section discusses the errors in the heating rate profiles through the cloud layer from the four 1D finite cloud methods discussed in Section 8.1. In this simulation, the cloud layer extended from 1000 to 1500 meters. Figs. 8.4 to 8.7 show the heating errors for each of the methods as a function of height in the cloud layer and $N_x$. These errors were defined as the difference between heating rate predicted by the 1D finite cloud method and that produced by the fully 3D model. Therefore, regions with errors greater than zero, represent regions were the particular 1D finite cloud method overestimated the heating or equivalently underestimated the cooling.

Accordingly, regions with errors less than zero represent regions were the 1D finite cloud method underestimated the heating or overestimated the cooling.

The results for the $N_c$ weighting scheme 1D finite cloud method are shown in Fig. 8.4. As shown, this method produced large overestimations of the cloud top cooling and cloud base warming. Through these results, it is evident that the $N_c$ weighting scheme biases the heating rates too close to the overcast cloud values near the cloud base and top. Away from the cloud boundaries, the errors are less but this method tended to underestimate the small amount of cooling occurring in the center of the finite cloud layer.

Fig. 8.5 shows the results for the comparison of the $N_a$ weighting scheme with the 3D model heating rates. A comparison with the $N_c$ weighting scheme errors reveals that the $N_a$ weighting scheme produced significantly smaller errors near the cloud top and base. As with the $N_c$ weighting scheme, both the cloud top cooling and cloud base warming were overestimated. As Fig 8.5 shows, a large region exists where the $N_a$ weighting scheme underestimated the cooling in the cloud away from the cloud boundaries. This underestimation of the cooling seems to be maximum 50 meters below the cloud top for a cloud fraction of 0.7. In addition, a region characterized by an underestimation of the heating can be found extending through most of the lower half of the cloud layer. The underestimation in the heating maximizes 50 above the cloud base for a cloud fraction 0.7.

The results for the method based on a linear variation of $N_c^{+/-}$, shown in Fig. 8.6, are similar to those produced by the $N_a$ weighting scheme. Once again, both the cloud top cooling and cloud base warming are overestimated. Similar to the $N_a$ weighting scheme, a region of cooling underestimation occurred in top half of the cloud layer and a region of heating underestimation occurred in the lower half of the cloud layer. Unlike the $N_a$ weighting case, the errors in these regions are roughly of the same magnitude and are distributed symmetrically about the cloud layer center.

Fig 8.7 shows the results for the 1D finite cloud method that uses the effective emissivity, $\epsilon_c$. Unlike the other 1D finite cloud methods, the effective emissivity method produces significant underestimations of both the cloud top cooling and the cloud base warming. In addition, contrary to the linear $N_c^{+/-}$ method, the cooling in the upper half of the cloud below was overestimated while the heating in the lower half of the cloud layer was slightly overestimated.

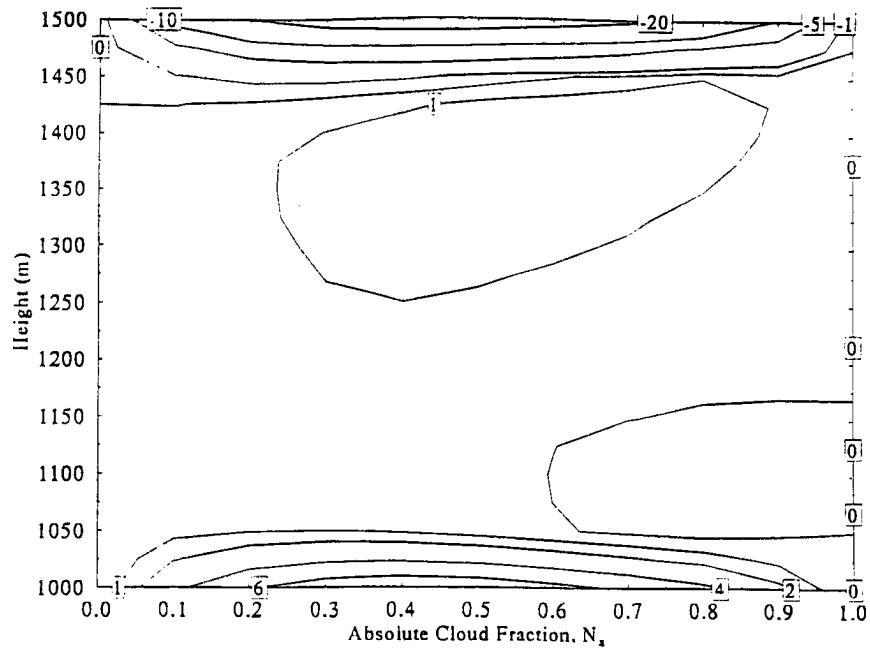**Fig. 8.4** The errors in the 11 $\mu$m heating rates due to the $N_e$ weighting scheme 1D finite cloud method. (°C/day/$\mu$m)



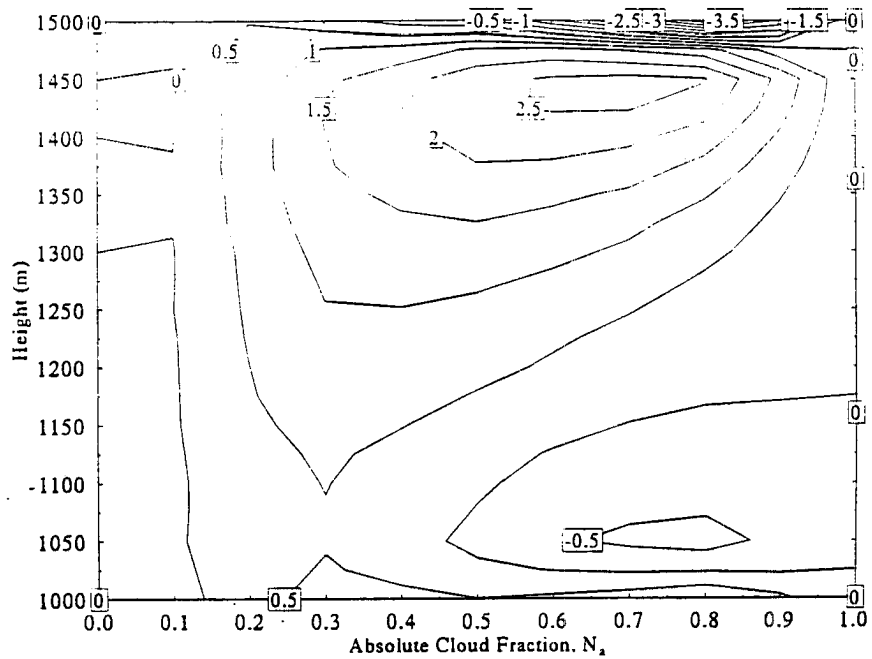**Fig. 8.5** The errors in the 11 $\mu$m heating rates due to the $N_a$ weighting scheme 1D finite cloud method. (°C/day/$\mu$m)
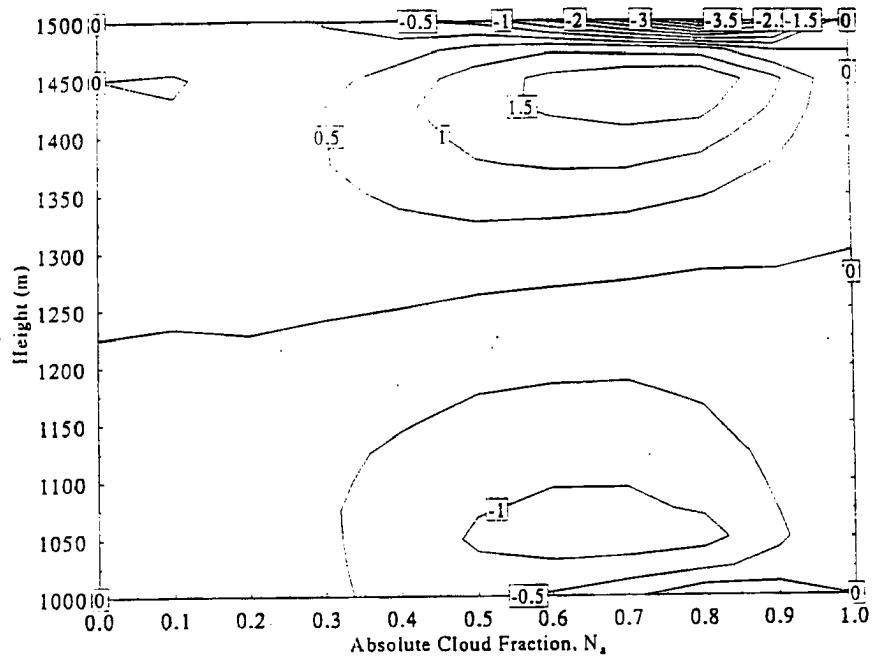
**Fig. 8.6** The errors in the 11 $\mu$m heating rates due to the linear $N_e^{+/-}$ 1D finite cloud method. (°C/day/$\mu$m)
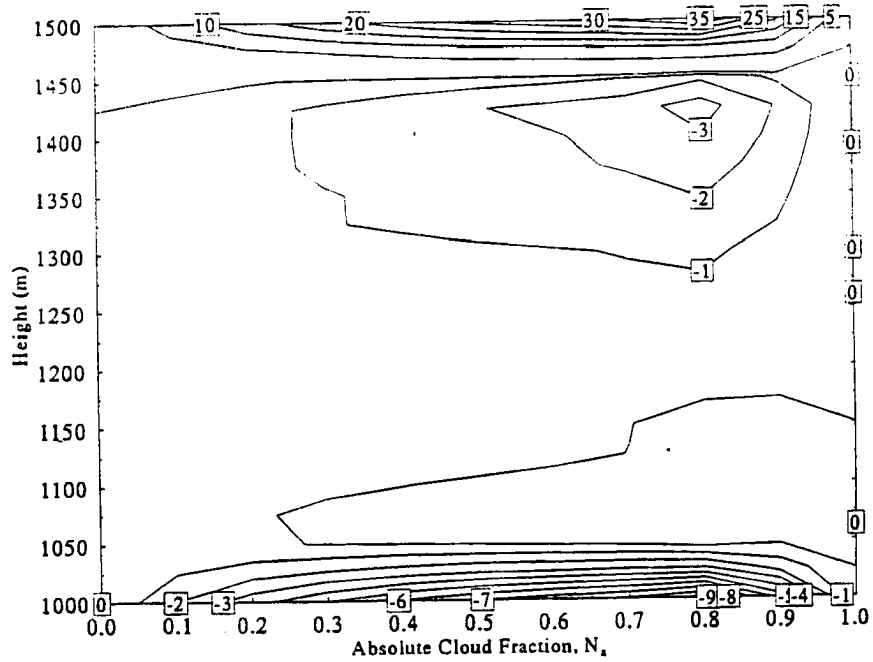


**Fig. 8.7** The errors in the 11 $\mu$m heating rates due to effective emissivity 1D finite cloud method. (°C/day/$\mu$m)

In order to better visualize the strengths and weakness of each of the 1D finite cloud methods, the results for one cloud fraction, 0.25, are isolated in Fig. 8.8. As expected from the previous results, the method that assumes a linear variation of $N_c^{+/-}$ most accurately reproduces the horizontally mean heating rate profile produced by the 3D model.

Fig 8.8 also shows a weakness inherent to the $N_a$ and $N_e$ weighting schemes. In this simulation, the cloud's are optically thick and the heating rates in the overcast cloud approach zero near the center of the cloud layer. Therefore, both the $N_e$ and $N_a$ weighting schemes predict heating rates near zero throughout the center of the cloud layer. Due the vertical flux divergence occurring near the cloud lateral boundaries, the actual mean horizontal heating rate in the center of the cloud layer never becomes zero.
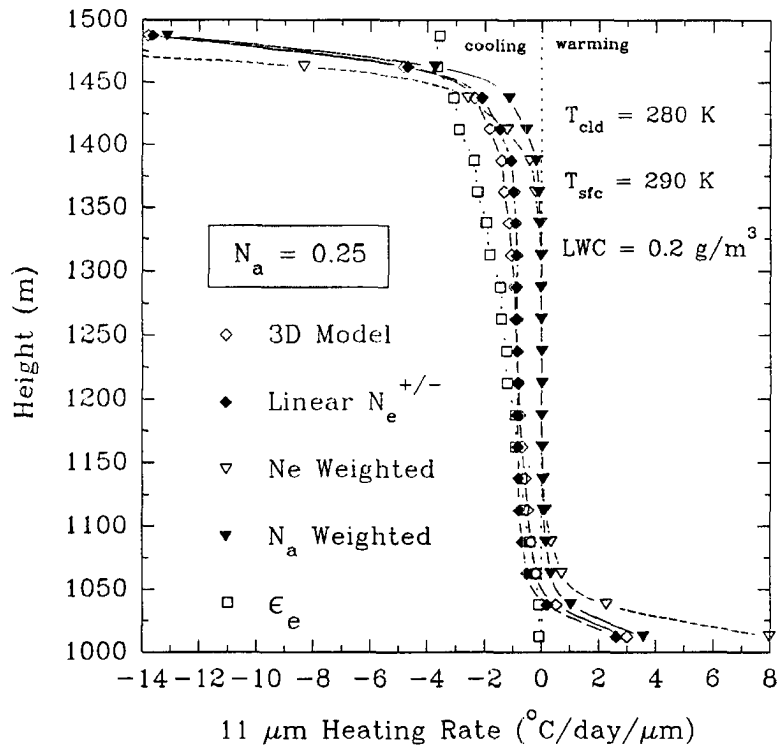


Fig. 8.8 The mean 11 $\mu$m heating rate results for the $N_a$=0.25 simulation.

In addition, Fig 8.8 also shows a weakness of the effective emissivity method. In order to reproduce the fluxes exiting from the finite cloud layer, the liquid water content of the effective homogenous cloud was extremely low (0.0052 g/m3) when compared to value used in the 3D model runs (0.2 g/m3). Due to this low liquid water content, the heating rate profile in the effective cloud lacks the strong cloud base warming and cloud top cooling

present in the actual 3D simulation.

## 8.2.2 Summary of the Cloud Layer Results

The results from Figs. 8.4-8.7 have been summarized in Fig. 8.9, which represents the mean 11 $\mu$m heating rate error integrated throughout the cloud layer for each cloud fraction. These errors were defined as the absolute value of the difference between the heating rates produced by the 1D finite cloud methods and the 3D model. As Fig 8.9 shows, the method that assumes of linear variation of $N_e^{+/-}$ throughout the cloud layer produces the lowest mean 11 $\mu$m heating rate error for most cloud fractions. For very high cloud fractions, the $N_a$ weighting scheme produced slightly lower errors than the linear $N_e^{+/-}$ method. The $N_e$ weighting schemes error are larger than the $N_a$ weighting scheme errors for all cloud fractions. The errors from the effective emissivity method are largest for high cloud fractions.
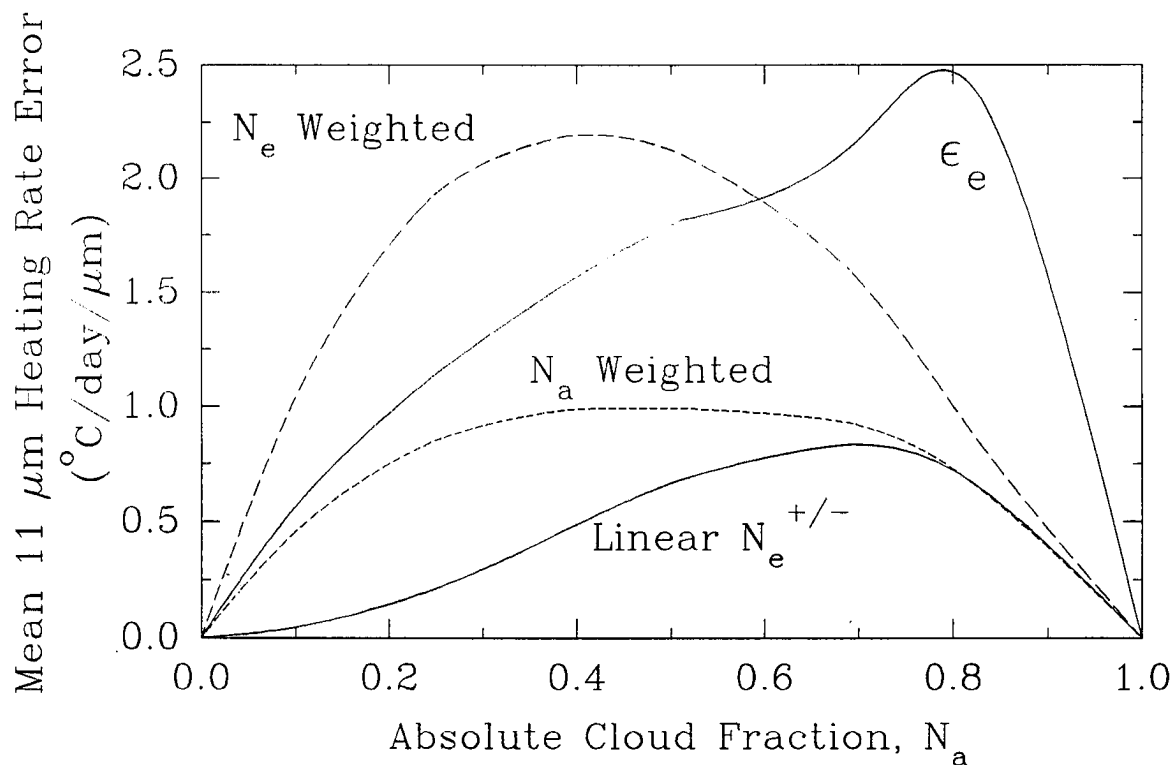


Fig 8.9 The vertically integrated mean 11 $\mu$m heating rate errors for the different 1D finite cloud methods.

### 8.2.3 The Total Heating of the Cloud Layer

Up to this point, the four 1D finite cloud methods have been judged on their ability to reproduce the horizontally mean heating rate profile through a simulated cloud layer. Another important consideration is the ability of each method to reproduce the total net cooling of the cloud layer. Since the linear variation of $N_e^{+/-}$ method, the $N_e$ weighting scheme, and the effective emissivity method all accurately predict the fluxes exiting the cloud layer, these methods also accurately predict the net cooling of the cloud layer. Unlike the other methods, the commonly used $N_a$ weighting scheme underestimates the difference between the net fluxes at the cloud layer boundaries and therefore underestimates the net cooling of the entire cloud layer. This underestimation of the total cooling of the cloud layer is shown in Fig. 8.10. Even though the $N_a$ weighting scheme's mean 11 $\mu$m heating rate error, Fig 8.9, was comparable to that from the linear $N_e^{+/-}$ method, the error from the $N_a$ weighting scheme did not cancel when integrated throughout the cloud layer as they did for the other methods. Therefore, the $N_a$ weighting scheme always underestimates the net cooling of the cloud layer and, as Fig 8.10 shows, this underestimation is largest for values of $N_a$ between 0.4 and 0.6.
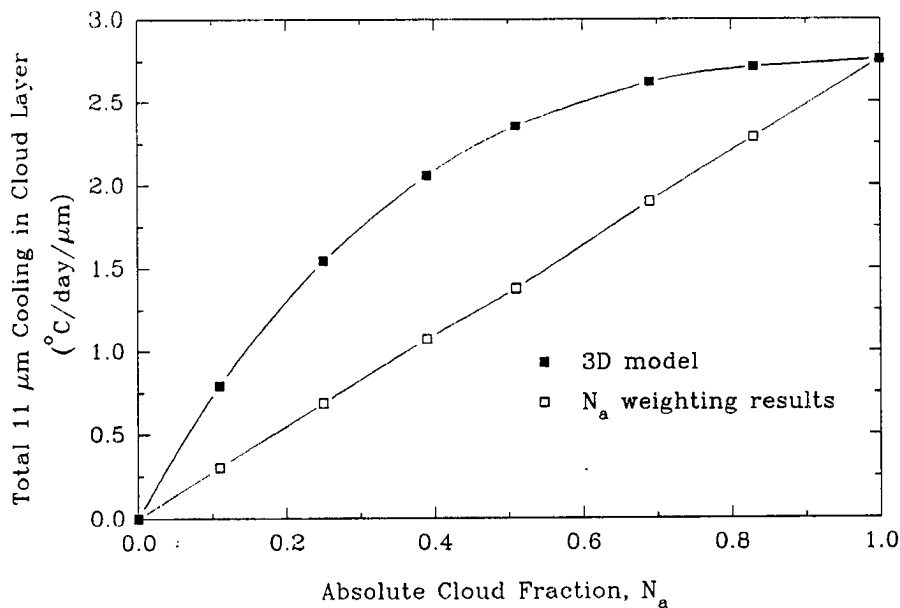


Fig. 8.10 A comparison of the net cooling in the cloud layer predicted by the $N_a$ weighting scheme and the 3D radiative transfer model for a regular array of cubic clouds.

### 8.2.4 The Sub-cloud and the Above Cloud Layers

Since this cloud simulation ignored atmospheric water vapor, no heating or cooling occurred in the sub-cloud and above-cloud layers. Since the linear $N_c^{+/-}$ method, the $N_c$ weighting scheme and the effective emissivity approach all accurately reproduce the fluxes exiting the cloud layer, little error in the net flux and heating rate profiles in the sub-cloud and above-cloud layers would be expected. Due to the errors in the fluxes exiting the layer calculated by the $N_a$ weighting scheme, the net flux profiles in these layers from this method will be in error. The heating rate errors from the $N_a$ weighting scheme in these layers would still be small however, due to the transparent behavior of the atmosphere in the modelled spectral region.

### 8.3  The Sensitivity of the Variation of $N_e^{+/-}$ to Cloud Liquid Water Distribution and Cloud Geometry

As discussed in Section 8.2.1, the 1D finite cloud method that assumed a linear variation of $N_c^{+/-}$ through the cloud layer produced the most accurate mean heating rate profiles of all the 1D finite cloud methods. In this section, the validity of this assumption will explored for several different cloud simulations. These simulations will explore the sensitivity of the variation of $N_e^{+/-}$ through the cloud layer to changes in $N_a$, the distribution of liquid water and the cloud layer geometry.

### 8.3.1  The Sensitivity of the Variation of $N_e^{+/-}$ to $N_a$

The cloud simulation performed here is identical to the one described in Section 8.2.  The cloud layer consisted of cubic clouds arranged in a regular array which extended infinitely. The cloud layer was placed between 1000 to 1500 meters. As Fig. 8.9 showed, the errors of the linear $N_e^{+/-}$ method tended to increase for large values of $N_a$.  A comparison of the actual variation and the assumed linear variation of $N_c^{+/-}$ through the cloud layer for three different values of $N_a$ is shown in Fig. 8.11.  As Fig. 8.11 shows, the actual variation of $N_e^{+/-}$ becomes less linear as $N_a$ increases, which explains the increase in the errors shown in Fig. 8.9 as $N_a$ increases. It is evident from this figure that the linear variation always under predicts the value of $N_c^+$ and $N_c^-$.  As seen in Eq. (8.11), the error in the value of $N_e^+$ will have less on an effect on the value of $F^+$ due to the closeness in the values of $F_{clr}^+$ and $F_{ovc}^+$ for low boundary layer clouds.  Due to the significant difference in the values of $F_{ovc}^-$ and $F_{clr}^-$ , especially

at 11 $\mu$m, underestimations in $N_e^-$ will lead to significant underestimations in F⁻. Therefore, most of the errors in

the linear $N_e^{+/-}$ method are due to underestimation of F⁻, the downwelling flux, in cloud layer. Since the inclusion

of atmospheric water vapor would act to decrease the difference between $F_{ovc}^-$ and $F_{clr}^-$, the errors associated with

these simulations, which neglected atmospheric water vapor, are larger than those expected from simulations with

realistic atmospheric effects.
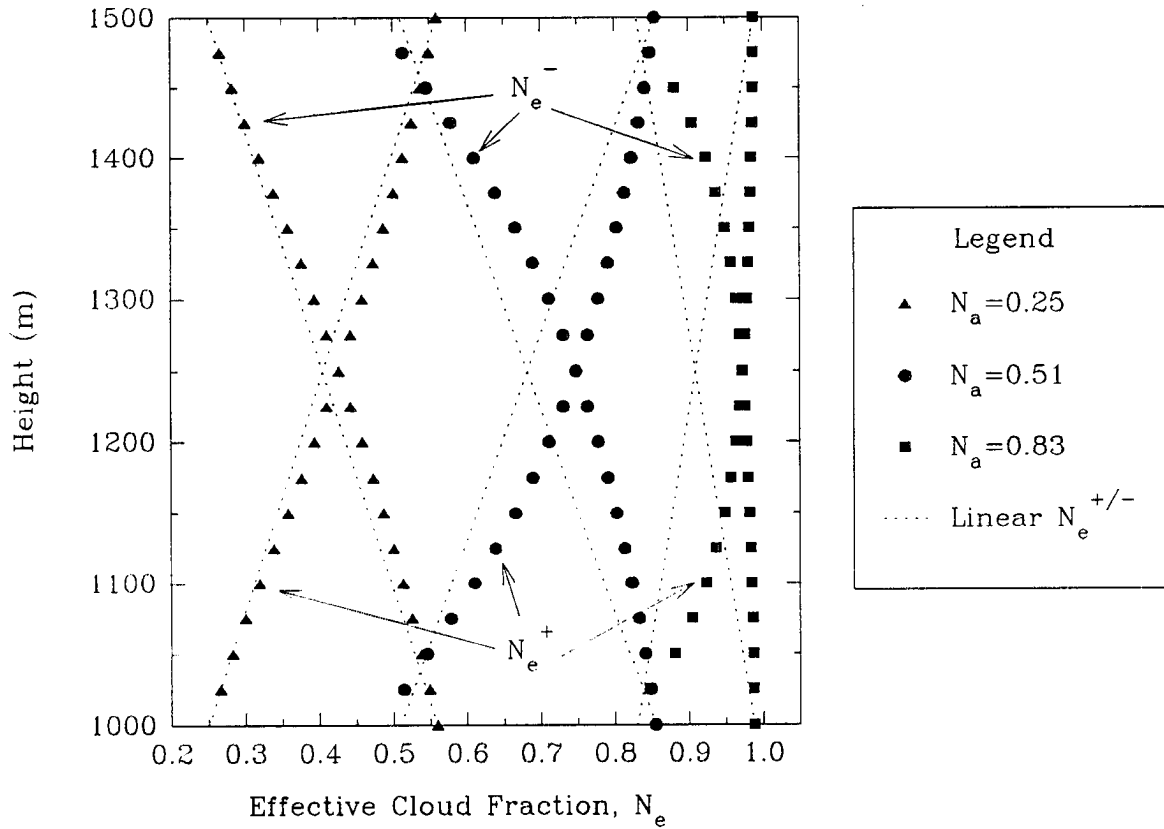
Fig. 8.11 The variation of $N_e^{+/-}$ through layers of cubic clouds for $N_a$ = 0.25, 0.51 and 0.83.

## 8.3.2 The Sensitivity to the Cloud Layer Geometry

In this section, the effect of varying the cloud geometry on the variation of $N_e^{+/-}$ through the cloud layer

is studied. A horizontal cross section of the cloud geometry used in this section is shown Fig. 8.12. The cloud layer

was constructed by repeating the cloud pattern shown in Fig 8.12 until the cloud layer extended to the horizon in

all directions. Except for the differing cloud geometry, the cloud simulation is identical to the one described in

90

Section 8.2. To isolate the effect of cloud layer geometry, this cloud layer was designed to produce approximately

the same values of $N_a$ and $N_e$ as the cloud layer consisting of a regular array of cubic clouds with $N_a = 0.50$. In

Fig. 8.13, the variation of $N_e^{+/-}$ through this cloud layer is compared with the variation of $N_e^{+/-}$ through a regular

cubic cloud layer. From Fig. 8.13, it can be seen that little additional errors would be expected in the heating rates

from the linear $N_e^{+/-}$ due to the differing cloud geometry.
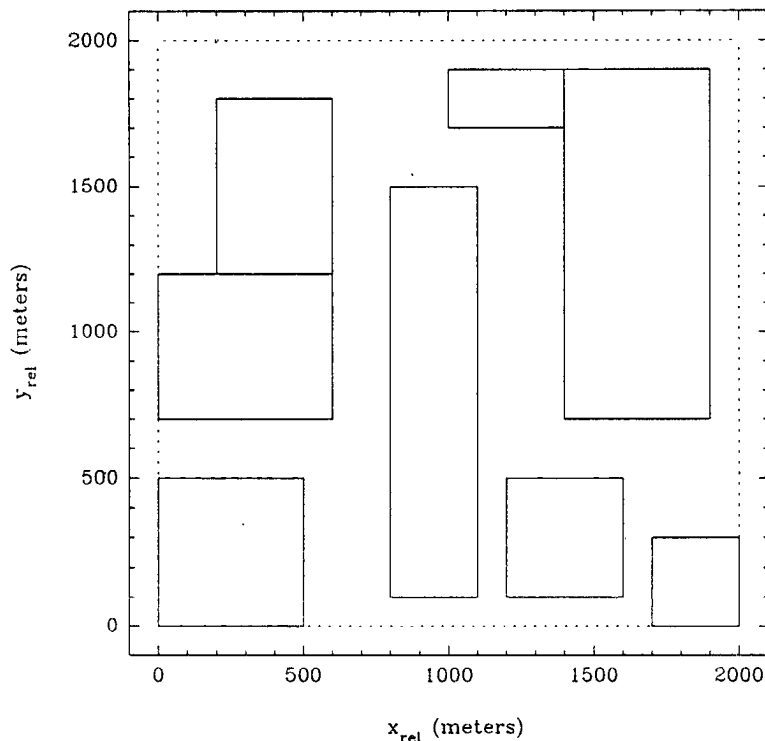


Fig. 8.12 A horizontal cross section of the non-regular non-cubic cloud layer geometry used in Section 8.3.2

## 8.3.3 The Sensitivity to the Distribution of Cloud Liquid Water

In the cloud simulation performed in Section 8.2, the vertical distribution of the cloud liquid was assumed

to be uniform. Measurements of the profiles of the cloud liquid water contents (LWC) in marine stratocumulus

clouds have shown that the LWC generally increase with height in the cloud (Duda *et al.* 1990). To test the

sensitivity of the variation of $N_e^{+/-}$ to the vertical LWC profile, a cloud simulation was run with a LWC profile

that increased linearly with height. The mean LWC of the cloud was still 0.2 g/m$^3$ but the LWC varied from 0.1

91
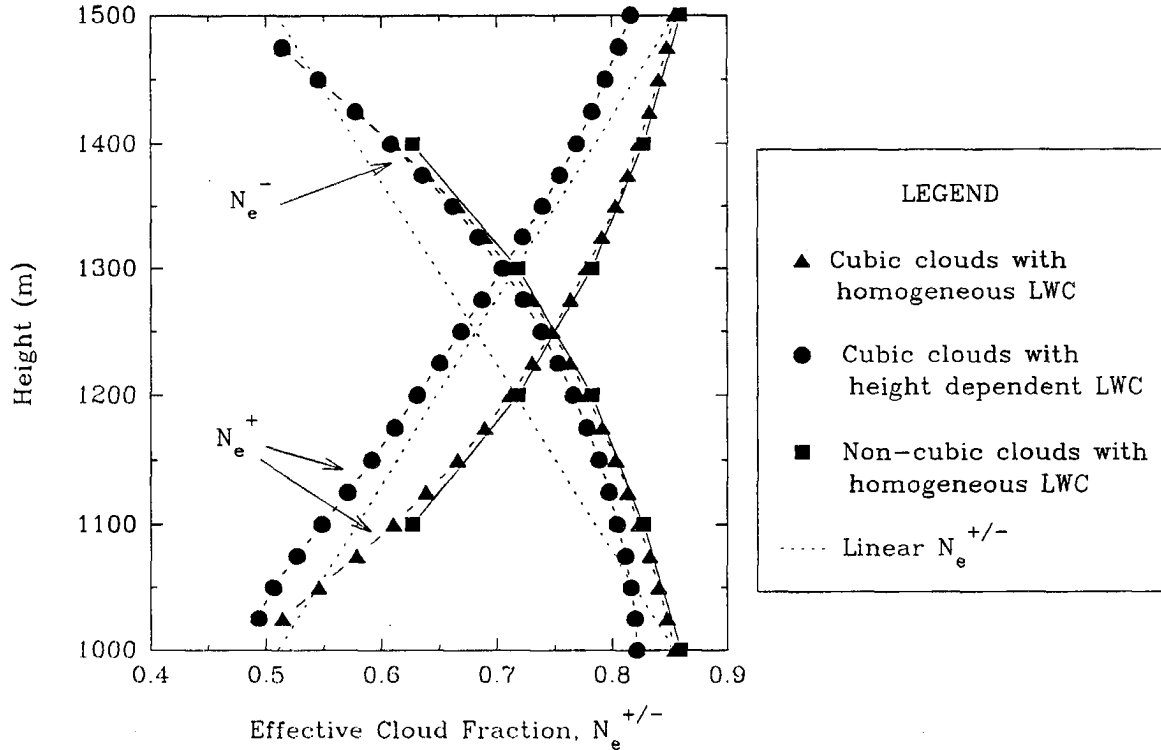
**Fig. 8.13 The effect of cloud geometry and LWC distribution on the variation of $N_e^{+/-}$.**

to 0.3 g/m³ from the base to the top of the cloud respectively. Except for the LWC, the cloud simulation was identical to the $N_a = 0.51$ simulation performed in Section 8.2.

The effect of the height dependent LWC on the variation of $N_e^{+/-}$ in the cloud layer is shown in Fig. 8.13. In this simulation, the $N_e^{+/-}$ profiles do show a significant difference the profiles of $N_e^{+/-}$ generated with a vertically homogeneous LWC. However, as Fig 8.13 shows, the linear $N_e^{+/-}$ assumption produced similar errors for the vertically homogeneous and vertically varying LWC profiles. Therefore, the linear $N_e^{+/-}$ method suffers no significant loss of accuracy when applied to clouds with LWC profiles that vary with height.

## 8.4 Summary

In this chapter the problem of incorporating 3D finite cloud effects into 1D radiative schemes was addressed. Four different methods were discussed which tried to reproduce the horizontally averaged heating rates in finite cloud layers. Of these methods, the one which assumed a linear variation of $N_e^{+/-}$ in the cloud layer was shown to be the most accurate. The commonly used method of weighting the overcast and clear sky heating profiles with the absolute cloud fraction, $N_a$, was shown to underestimate the total cooling of the cloud layer.

# Chapter 9

## PARAMETERIZATION OF THE EFFECTIVE CLOUD FRACTION

In the previous chapter, a method was developed which allowed for the inclusion of 3D finite cloud effects in 1D longwave radiative transfer schemes. To use this method, values of both the absolute, $N_a$, and the effective cloud fraction, $N_e$, were needed. Though values of $N_a$ are readily produced by numerical weather prediction models and measured by satellites, values of $N_e$ are not. Since numerical models rarely resolve individual clouds, the determination of $N_e$ must be accomplished through a parameterization in terms of other quantities produced by these models. The goal of this chapter, therefore, is to discuss possible parameterization methods of $N_e$. A second aim of this chapter is to suggest possible satellite measurement techniques which would allow for $N_e$ parameterizations on a global scale.

One possible parameterization of $N_e$ is given by Eq. (4.3). In this parameterization, $N_e$ was given as function of $N_a$ and the mean cloud aspect ratio, a. To be useful to numerical modelers, a parameterization needs to be based on quantities available in numerical models. Cloud aspect ratio, however, is not routinely calculated in numerical models nor is the routine measurement of cloud aspect ratio feasible. In addition, even if a model or measurement technique could calculate a mean aspect ratio of the cloud layer, it is the effective cloud aspect ratio that determines $N_e$. The effective cloud aspect ratio differs from the mean cloud aspect ratio in that the effective aspect ratio accounts for the relative positioning of the clouds in the cloud layer. For the regular array of cuboidal clouds used to produce Eq. (4.3), the effective and mean cloud ratios are identical.

## 9.1 Parameterization of $N_e$ Based on ASTEX Data

This section will explore the development of a parameterization of $N_e$ based on data collected during ASTEX. As described in Chapter 5, the predominant cloud regime during ASTEX consisted of marine stratocumulus. The method of calculating $N_e$ through the use of broad-band and narrow-band longwave radiometers

93

was described in Chapter 4.

### 9.1.1 A Parameterization Based on $N_a$

Since $N_a$ is a commonly measured and routinely estimated quantity in numerical models, a parameterization of $N_c$ based solely on $N_a$ would be highly desirable. Fig 9.1 shows the observed variation of $N_c$ with $N_a$ for the entire ASTEX period. Each data point in Fig 9.1 represents daily averaged quantities. As a reference in Fig 9.1, the variation of $N_c$ with $N_a$ given by Eq. (4.3) is shown for three values of $a_{cub}$. In addition, the dashed line represents a curve fit of the ASTEX data and is given by:

$$N_e = N_a [e^{0.6416(1-N_a)}]$$

(9.1)

The mean rms difference for Eq. (9.2) is 0.11. Though the uncertainty in these measurements is large, as discussed in Chapter 5, $N_a$ does seem to provide a satisfactory basis for parameterizations of $N_c$ for marine stratocumulus.

Assuming a systematic variation of $N_c$ with $N_a$, is equivalent to assuming a systematic variation in the effective cloud aspect ratio with $N_a$. Comparison of the ASTEX data in Fig 9.1 with the results for constant values of $a_{cub}$ shows that there is a tendency for the values of $a_{cub}$ of ASTEX clouds to decrease with increasing $N_a$. The observed variation of $a_{cub}$ with $N_a$ is shown in Fig. 9.2. As described in Section 5.4.3, $a_{cub}$ represents the cloud aspect ratio of a hypothetical cuboidal cloud layer which possesses the known values of $N_c$ and $N_a$. Fig 9.2 shows, the observed variation of $a_{cub}$ with $N_a$ for ASTEX. As in Fig 9.1, each data point represents a daily averaged value. The linear curve fit, shown by the solid line, does show an inverse relationship between $a_{cub}$ and $N_a$. This relationship between $a_{cub}$ and $N_a$ implies that the horizontal extent of marine stratocumulus clouds decrease as $N_a$ decreases.

### 9.1.2 A Parameterization Based on LWP

Another possible basis for a parameterization of $N_c$ is the mean liquid water path, LWP. Like $N_a$, LWP is a quantity that is readily produced by numerical models, and is therefore also a desirable basis for a parameterization of $N_c$. The observed daily averaged variation of $N_c$ with LWP from ASTEX is shown in Fig. 9.3.
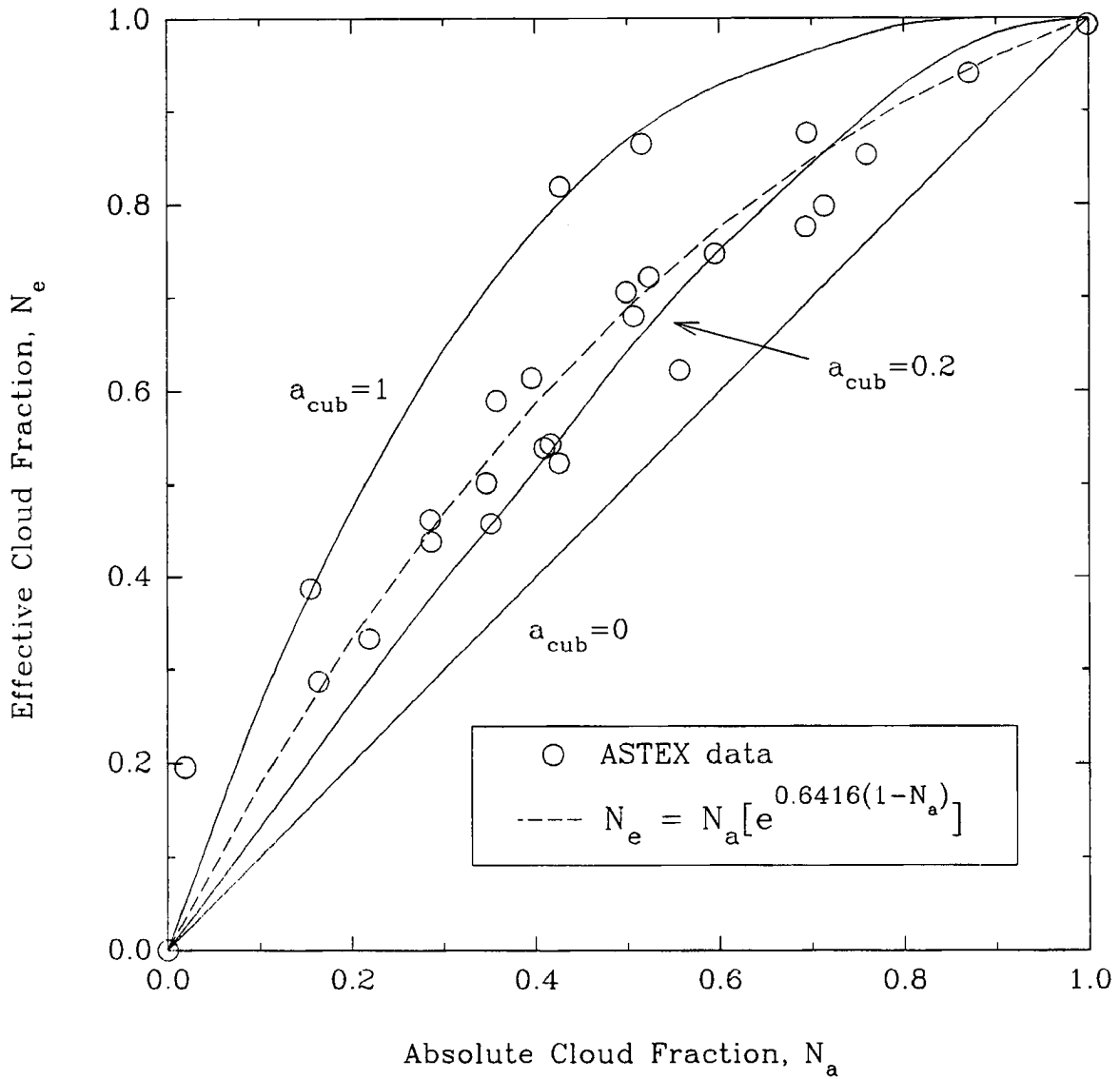
**Fig. 9.1** The observed daily-averaged variation of $N_e$ with $N_a$ during ASTEX. Solid lines represent results of Eq. (4.3) for $a_{cub}$ = 0,0.2 and 1.0.

The LWP values were obtained by averaging the measurements of a zenith looking microwave radiometer operated by Dr. Jack Snider of NOAA. The dashed line in Fig. 9.3 is a curve fit of the ASTEX data as is given by :

$$N_e = 1 - e^{-0.0237 LWP} \qquad (9.2)$$

The mean rms difference of the fit given by Eq. (9.2) is 0.28, which is more than double the value from the curve fit based of $N_a$, Eq. (9.1). From this data, $N_a$ appears to be a better basis for a parameterization of $N_e$ for marine stratocumulus than LWP. One problem with a LWP based parameterization is that two different distributed cloud

95

Effective Cuboiudal Aspect Ratio, $a_{cub}$

0.5

○ ASTEX data

0.4

0.3

0.2

0.1

0.0

0.0    0.2    0.4    0.6    0.8    1.0

Effective Cloud Fraction, $N_a$
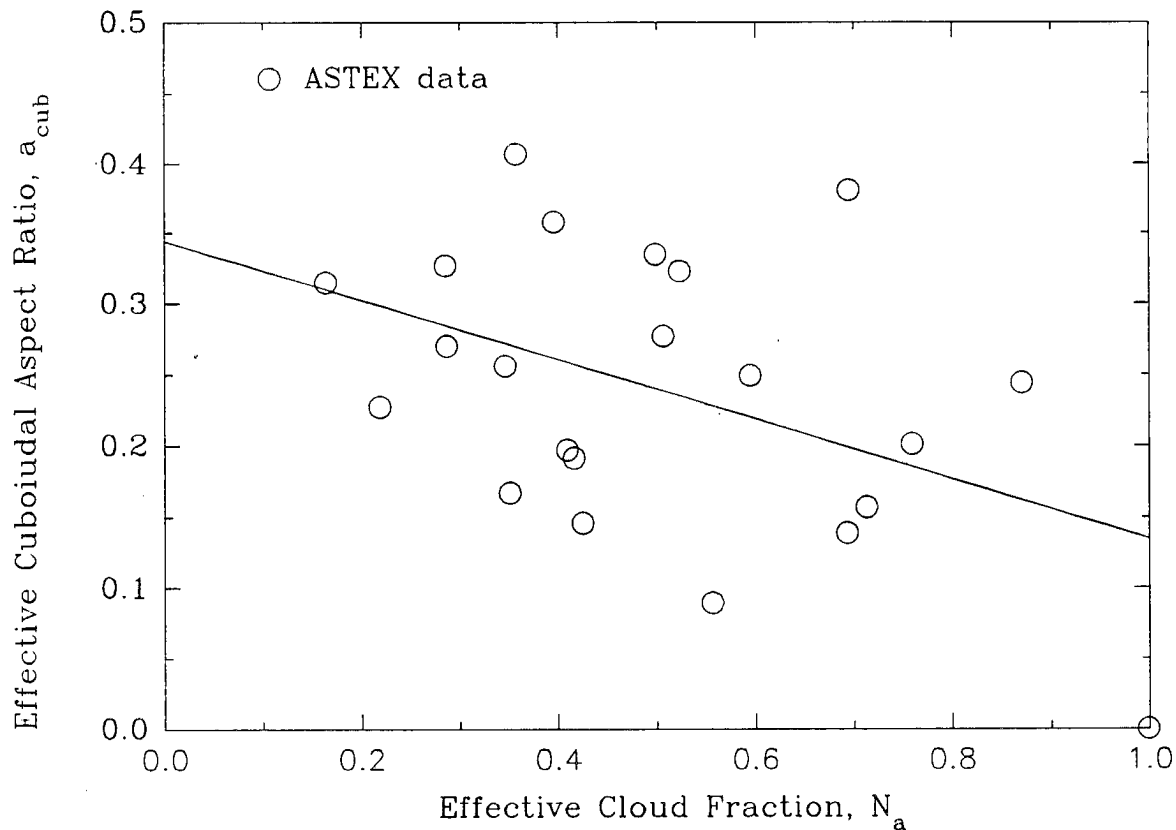
Fig 9.2 Observed daily-averaged variation of $a_{cub}$ with $N_a$ during ASTEX.

layers could have the same averaged LWP but different values of $N_a$ and $N_c$. If such regions exist where this situation commonly occurs, parameterizations based on LWP in these regions should be avoided.

## 9.2 Direct Measurement of $N_c$ by Satellites

The parameterization described above were based upon only one month of data from one geographical location. In order to determine the geographical and seasonal variation of any parameterization of $N_c$, a global study of the variation of $N_c$ with differing cloudiness regimes needs to be accomplished. One method of studying the geographical and seasonal variation of $N_c$ globally would be to use satellite data. Though satellites routinely produce estimates of cloud fraction, this cloud fraction is more closely related to $N_a$ than $N_c$ due to the satellite viewing geometry. Therefore, values of $N_c$ are not currently produced from satellite data. The goal of this section, therefore, is to suggest possible techniques to enable satellites to estimate $N_c$.
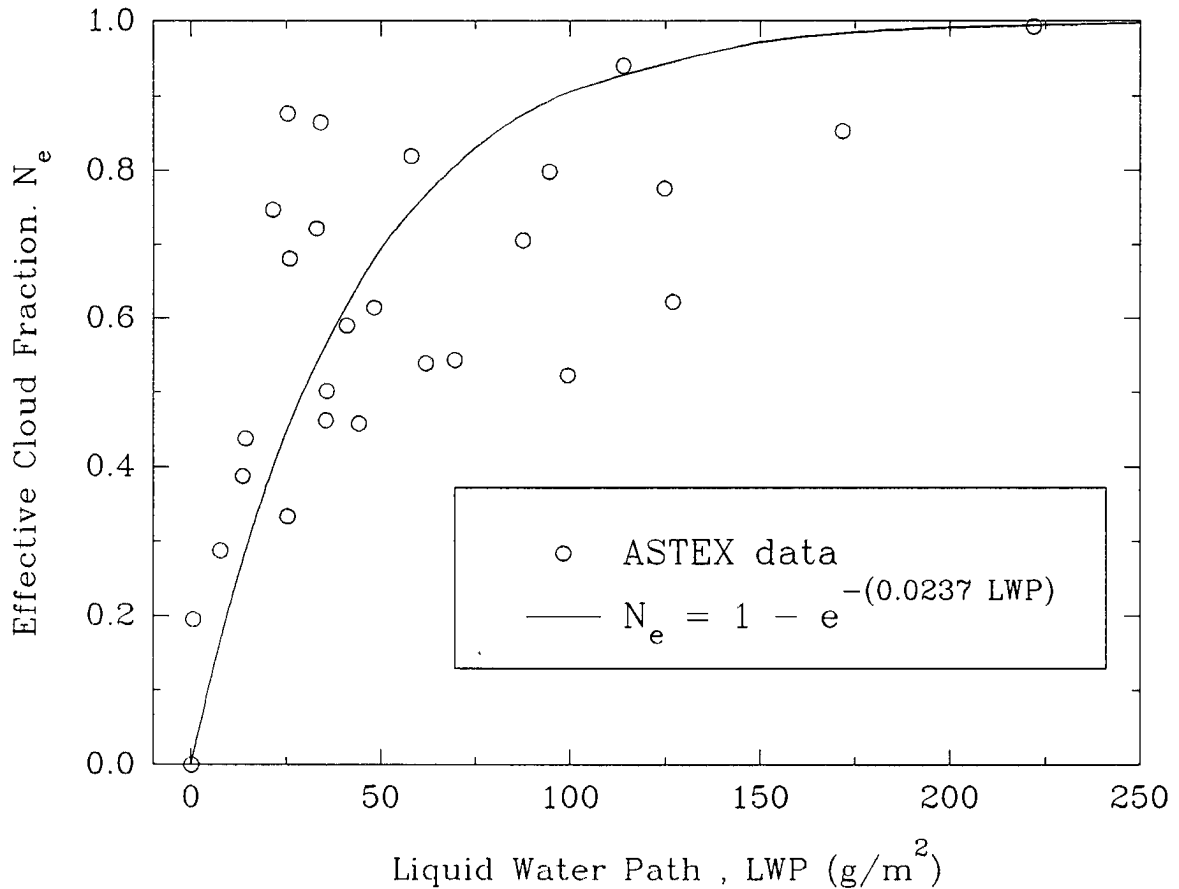
Fig. 9.3 Observed daily-averaged variation of $N_e$ with LWP during ASTEX.

### 9.2.1 The Estimation of $N_e$ from Measurements of $\epsilon_e$

As described in Section 7.2, there exists a strong relationship between the effective cloud fraction of a cloud layer, $N_e$, and the effective emissivity of the cloud layer, $\epsilon_e$. Using the 11 $\mu$m model developed in Chapter 3, values of $\epsilon_e$ were shown to be always greater than $N_e$ with the differences increasing with the amount of atmospheric water vapor. Assuming that satellites could measure $\epsilon_e$, only an adjustment for the amount water vapor emission in the cloud layer would be needed to produce an estimate of $N_e$. For the 11$\mu$m simulation described in Section 8.2, the dependence of the $N_e$-$\epsilon_e$ relationship on the amount of water vapor in the cloud layer is shown in Fig. 9.4. For this 11 $\mu$m simulation the relationship between $N_e$ and $\epsilon_e$ can be expressed accurately as:

where $u_{cld}$ is the amount of water vapor in the cloud layer. Depending on the spectral region, the emission from

97

$$N_e = \frac{\epsilon_\theta - 0.1 u_{cld}(1 + 3 u_{cld})}{1 - 0.1 u_{cld}(1 + 3 u_{cld})} \qquad (9.3)$$

species other than water vapor might need to be accounted for. Note that since both $N_e$ and $\epsilon_e$ are functions of $N_a$ and the cloud aspect ratio, the difference between $N_e$ and $\epsilon_e$ has little or no dependence on the geometry of the cloud layer.
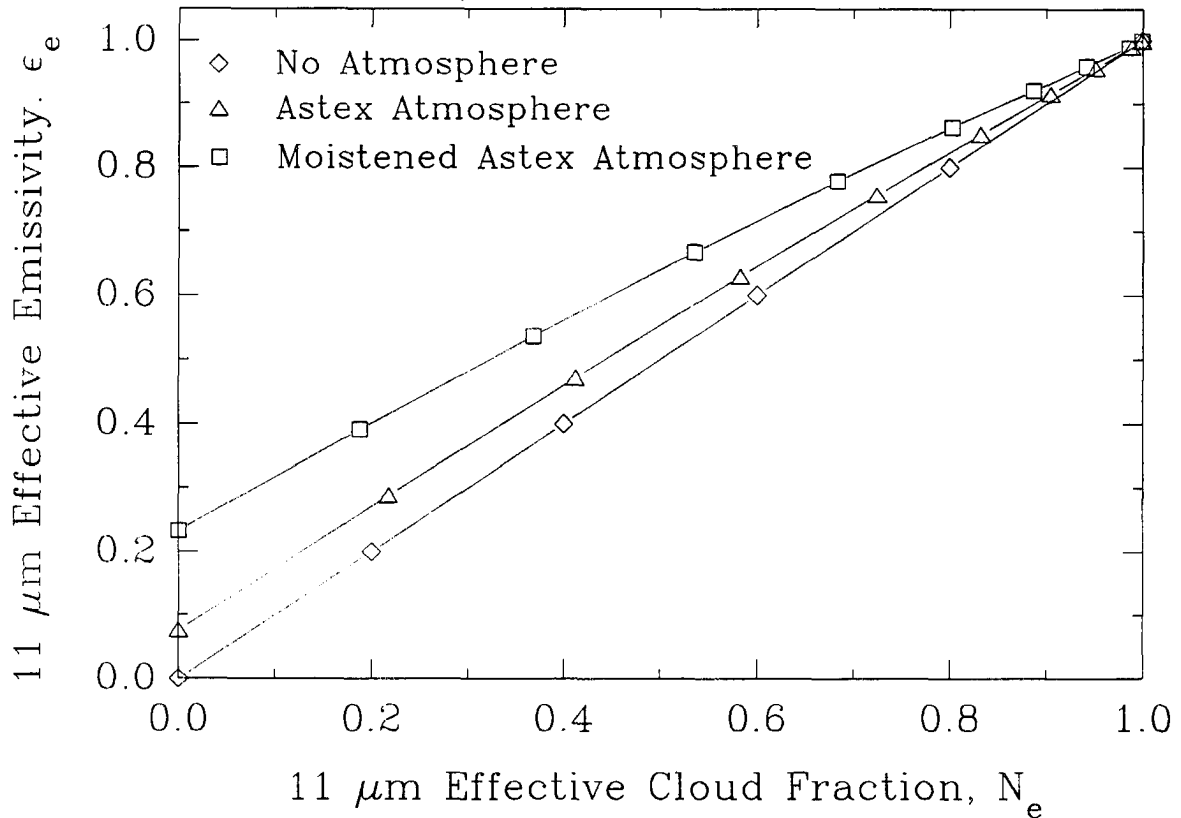


Fig 9.4 Simulation variation of $\epsilon_e$ with $N_e$ for different amounts of cloud layer water vapor.

### 9.2.2 The Direct Measurement of $N_e$

Another possible technique to derive values of $N_e$ from satellite based sensors is to vary slightly the currently used technique to derive cloud fraction. As mentioned previously, due to the altitudes, narrow fields-of-view and the viewing angles of satellites, the cloud fraction estimates from satellites approximate the value of $N_a$, which only accounts for the horizontal coverage of the clouds.

Imagine a cloud field consisting of an infinite horizonal array of cuboidal clouds. If a satellite high above the cloud layer were to measure the cloud fraction directly below the satellite, the measured cloud fraction would approximate the value of $N_a$. If the satellite were to scan out towards the horizon, the probability of a clear line-of-sight would decrease from a value of $1-N_a$, at nadir, to 0, at the horizon. This variation in the probability of a clear line-of-sight, P, as a function of zenith angle, $\Theta$, for four different cloud fields is shown in Fig 9.5.

In Fig 9.5, $P(\Theta)$ ranges from approximately $1-N_a$ to 0 as $\Theta$ increases from 0 to 90°. One possibly useful consequence of this variation would be if there were one unique value of $\Theta$ where $P(\Theta)$ had the value of $1 - N_e$ for any cloud layer geometry. Let this value of $\Theta$ where $P(\Theta) = 1 - N_e$ be defined as $\Theta_o$. As shown in Fig 9.5, $\Theta_o$ does depend slightly on $N_a$. However, this dependence is small enough to allow for accurate estimates of $N_e$ for all $N_a$ if a value of 45° is assumed for $\Theta_o$. The effect of non-regular cloud geometry, shown by the dashed line in Fig. 9.5, was shown to be minimal. This non-regular cloud geometry is shown in Fig 8.11. These results suggest that if the current methods of determining cloud fraction were applied at a zenith angle of 45° relative to the cloud layer, the measured cloud fraction should provide an estimate of $N_e$.

## 9.3 Summary

In this chapter, parameterizations of $N_e$ derived from ASTEX data were presented. Parameterizations based on $N_a$ and LWP were shown. The parameterization based on $N_a$ was shown to match the observations more closely than the LWP based parameterization. From the ASTEX data, the effective cloud aspect ratio was shown be inversely related to $N_a$. In addition, possible satellite measurement techniques were suggested to enable the calculation and parameterization of $N_e$ on a global basis.
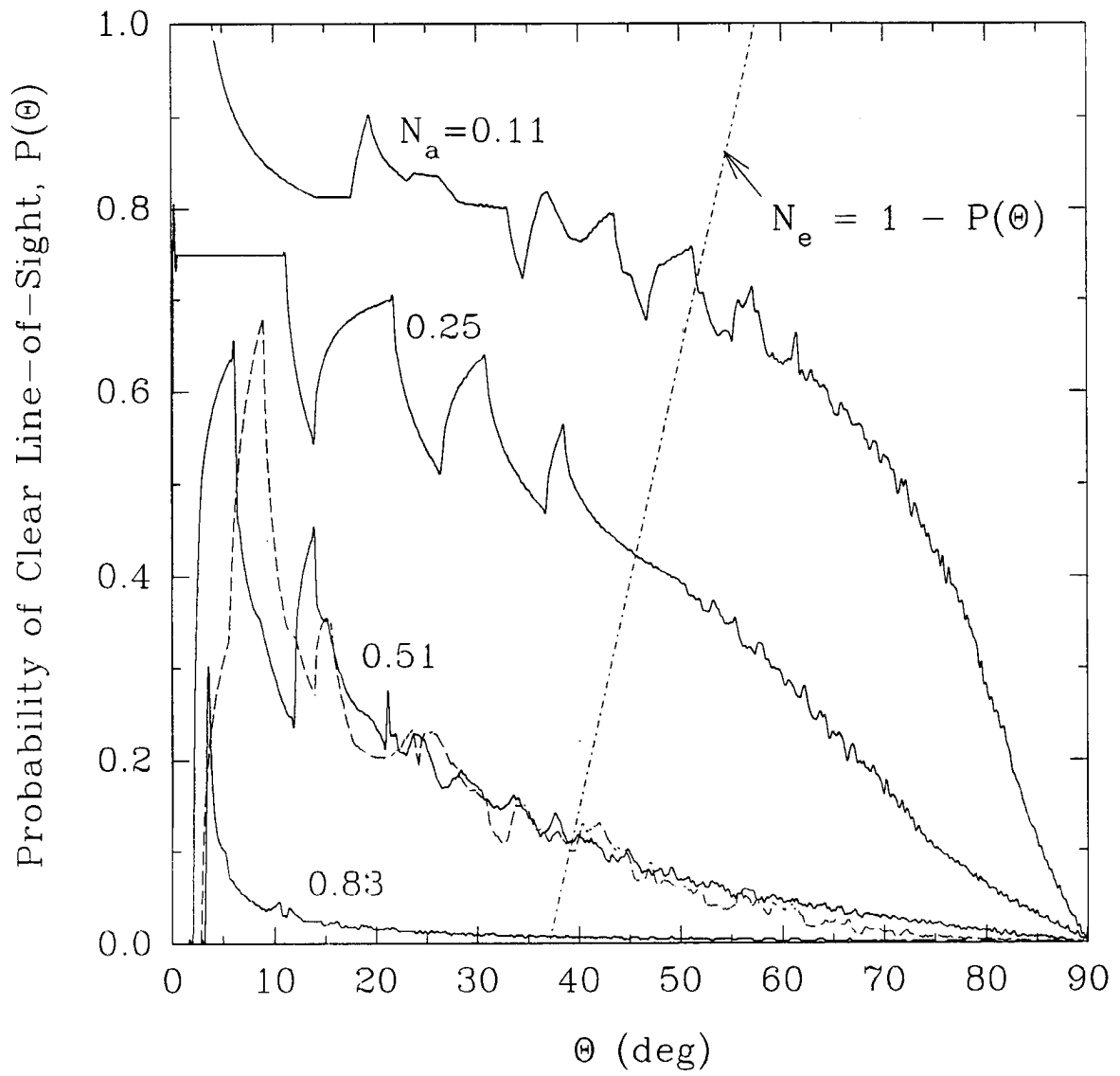
**Fig. 9.5** Probability of clear line-of-sight functions for several different cloud layer geometries. Dashed line shows variation of $\Theta_o$ with $N_a$.

## Chapter 10

## CONCLUSIONS

This research focused on the role of finite cloud effects in longwave radiative transfer. Clouds have been known for decades to be a fundamental modulator of radiation in the earth's atmosphere. As numerical weather and climate modelling begin to treat clouds realistically, the inclusion of the effect of the finite dimensions of clouds becomes imperative.

One of the strengths of this research was the ability to show directly finite cloud effects in measurements of the longwave surface flux. The observations used in this study were collected during the ASTEX phase of FIRE during June 1992 on the Island of Porto Santo. The analysis of these measurements showed that longwave surface flux schemes which ignored the vertical dimensions of the clouds typically underestimated the surface flux by 5-10 W/m$^2$. In addition, values of the effective cloud fraction, $N_e$, which account for cloud geometry, at ASTEX where found to 30% higher on average than the absolute cloud fraction, $N_a$. $N_a$ is the cloud fraction usually predicted by numerical models and used in one dimensional radiative transfer schemes. These values from the ASTEX region should be representative of any fair weather cumulus cloud field.

This research investigated the parameterization and inclusion of these finite cloud effects into existing one dimensional radiative transfer schemes. Several different methods for the inclusion of finite cloud effects where compared. The commonly used method of accounting for partial cloudiness by weighting overcast and clear sky flux profiles by the absolute cloud fraction, $N_a$, was found to significantly underestimate the net cooling in cloud layers. One method which accurately predicted both the net cooling and the distribution of cooling in the cloud assumed a linear variation of $N_e$ through the cloud layer. Due to the simplicity of this method, current one dimensional longwave radiative transfer schemes could be modified easily to account for finite cloud effects. In addition, parameterizations of $N_e$ based on $N_a$ and the liquid water path developed from the ASTEX data.

101

Using a three dimensional 11 $\mu$m model, which neglected scattering, the heating rates in isolated and non-isolated clouds were compared. The effect of neighboring clouds on the total cooling of non-isolated cubic clouds were found to be significant when the clouds were spaced less than two cloud widths apart. Plane-parallel theory was shown to provide an inaccurate estimate of the total cooling in non-isolated clouds until the cloud spacing was less than 10% of the mean cloud width. In addition, the heating around the edges of non-isolated clouds was found to be fundamentally different from that in isolated clouds. In isolated clouds, the edge cooling could lead to positive dynamical and microphysical feedbacks in the growth of the cloud. These feedbacks were shown to be fundamentally different in non-isolated clouds.

Through the observations and modelling simulations presented here, the role of finite cloud effects in longwave radiative transfer was shown to be worthy of further study. In this research, the effective cloud fraction was shown to be a useful quantity in characterizing finite cloud effects. Since routine measurements of $N_c$ are not currently made, one beneficial area of future research might be the measurement of this important quantity on a global basis. Once the variation of $N_c$ is known globally, comprehensive studies of finite cloud effects in longwave radiative transfer would then be possible.

# REFERENCES

Ackerman, S. A., W. L. Smith , J. D. Spinhirne, and H. E. Revercomb, 1990: The 27-28 October 1986 FIRE IFO Cirrus Case Study: Spectral Properties of Cirrus Clouds in the 8-12 $\mu$m Window, *Mon. Wea. Rev.*, **118**, 2377-2388.

Albrect, B. A. and S. K. Cox, 1976: Pyrgeometer data reduction and calibration procedures. Atmos. Sci. Paper #251, Colorado State University.

Cox, S. K., 1969: Observational evidence of analmalous infra-red cooling in a clear tropical atmosphere. *J. Atmos Sci.*, **26:6**, 1347-1349.

Duda, D. P., G. L. Stephens, and S. K. Cox, 1989: Microphysical and radiative properties of marine stratocumulus from tethered balloon measurements, *J. Appl. Meteor.*, **30**, 170-186.

Ellingson, R. G., 1982: On the effects of cumulus dimensions on longwave irradiance and heating rate calculations. *J. Atmos. Sci.*, **39**, 886-896

Evans, K. F., 1993: A general solution for stochastic radiative transfer, *Geophys. Res. Letters*, **20**, 2075-2078.

Harshvardhan, J. A. Weinman and R. Davies, 1981: Transport of infrared radiation in cuboidal clouds. *J. Atmos. Sci.*, **38**, 2500-2513.

Harshvardhan, and J. A. Weinman, 1982: Infrared radiative transfer through a regular array of cuboidal clouds. *J. Atmos. Sci.*, **39**, 431-439

Irvine, W. M., and J. B. Pollack, 1968: Infrared optical properties of water and ice spheres. *Icarus*, **8**, 324-360.

Killen, R. M., and R. G. Ellingson, 1994: The effect of shape and spatial distribution of cumulus clouds on longwave irradiance. *J. Atmos. Sci.*, **51**, 2123-2136.

Kneizys, F. X., E. P. Shettle, W. O. Gallery, J. H. Chetwynd Jr., L. W. Abreu, J. E. A. Selby, R. W. Fenn and R. A. McClatchey, 1980: Atmospheric Transmittance/Radiance: computer code LOWTRAN 5. Report No. AFGL-TR-80-0067, Air Force Geophysics Lab, Hanscom AFB, MA., 200 pp.

Lappen C., 1994: An assessment of the extent of the contamination of measurements taken in Porto Santo during ASTEX, Atmos. Sci. Paper #549, Colorado State University.

Liou, K. N., and S. C. Ou, 1979: Infrared radiative transfer in finite cloud layers. *J. Atmos. Sci.*, **36**, 1985-1996.

Minnis P., P. W. Heck, D. F. Young, C. W. Fairall and J. B. Snider, 1992: Stratocumulus Cloud Properties Derived from Simultaneous Satellite and Island-based Instrumentation during FIRE. *J. Appl. Meteor.*, **31**, 317-339.

Niylisk, Kh. Yu, 1968: Atmospheric thermal radiation in partly cloudy regions. Izv. Acad. Sci. USSR, *Atmos. Oceanic Phys.*, **4**, 383-396.

Niylisk, Kh. Yu, 1972: Cloud Characteristics in problems of radiation energetics in the earth's atmosphere. Izv. Acad. Sci. USSR, *Atmos. Oceanic Phys.*, **8**, 270-281.

Plank, V. G., 1969: The size distribution of cumulus clouds in representative Florida populations. *J. Appl. Meteor.*, **8**, 46-67.

Preisendorfer, R. W., and G. L. Stephens, 1984: Multimode radiative transfer in finite optical media. I: Fundamentals. *J. Atmos Sci.*, **41**, 709-724.

Roach, W. T., 1976: On the effect of radiative exchange on the growth by condensation of a cloud or fog droplet. *Quart. J. R. Met. Soc.*, **102**, 361-372.

Roberts, R. E., L. M. Biberman and J.E. A. Selby, 1976: Infrared continuum absorption by atmospheric water vapor in the 8-12 $\mu$m window. *Appl. Opt.*, **15**, 2085-2090.

Schmetz, J., 1984: On the parameterization of the radiative properties of broken clouds. *Tellus*, **36A**, 417-432.

Stephens, G. L., 1978: Radiation profiles in extended water clouds. I: Theory. *J. Atmos. Sci.*, **35**, 2111-2122.

Stephens, G. L., 1984: The parameterization of radiation of numerical weather prediction and climate models. *Mon. Wea. Rev.*, **112**, 826-867.

Stephens, G. L., and R. W. Preisendorfer, 1984: Multimode radiative transfer in finite optical media. II: Solutions. *J. Atmos. Sci.*, **41**, 725-735.

Stowe, L. L., H. Y. M. Yeh, T. F. Eck, C. G. Wellemeyer, H. L. Kyle and the Nimbus-7 Cloud Data Processing Team, Nimbus-7 global cloud climatology, II, First-year results, *J. Clim.*, **2**, 671-709, 1989.

Stull, R. B., 1984: Models and measurements of the interaction between the mixed layer and fair-weather cumulus clouds; Parts 2. Some preliminary measurements. *Transactions of An APCA Specialty Conference on Environmental Impact of Natural Emissions* (V. P. Aneja, Ed.), Air Pollution Control Assoc., 326-337.

Warren, S. G., C. J. Hahn, J. London, R. M. Chervin and R. L. Jenne, 1986: Global Distribution of Total Cloud Cover and Cloud Type amount over land, *NCAR Technical Notes*, TN-273-STR